NEW PHASES IN THE HYDROUS FERRIC SULFATE SYSTEM, A SUPPORTING ARGUMENT THAT THE MINERAL LAUSENITE IS OF FORMULA $Fe_2(SO_4)_3 \cdot 5H_2O$ AND THE CRYSTAL STRUCTURE REFINEMENT AND HYDROGEN BONDING SCHEME OF THE MINERALS QUENSTEDTITE AND ROMERITE

by

Robin Elizabeth Westland

A thesis submitted to the Department of Geological Sciences and Geological Engineering

In conformity with the requirements for

the degree of Master of Science

Queen's University

Kingston, Ontario, Canada

(August, 2012)

Abstract

A series of experiments were conducted to explore the hydration state of the mineral lausenite. The experiments of Posnjak and Merwin (1922) were recreated and the conclusion is reached that lausenite is of mineral formula $Fe_2(SO_4)_3 \cdot 5H_2O$, rather than $Fe_2(SO_4)_3 \cdot 6H_2O$ as suggested by Posnjak and Merwin (1922). This conclusion is based on the X-ray diffraction data which found that the Posnjak and Merwin experiments produced a phase whose pattern matched that of the pentahydrate identified by Majzlan (2005). The refractive index data and morphology of this phase is also a match for the mineral described previously as a hexahydrate by Posnjak and Merwin (1922) and Lausen (1928).

Synchrotron X-ray diffraction data was collected from a possible new phase in the hydrous ferric sulfate system. The data were analyzed and a unit cell was identified with monoclinic unit cell dimensions of a = 7.532(3)Å b = 12.551(6)Å c = 7.077(4)Å and β = 96.775(8)° with a unit cell volume of 664.4Å^3. This phase was determined to grow only at temperatures above 85°C and at a RH of ~23%.

The atomic structures of the minerals quenstedtite [$Fe_2(SO_4)_3 \cdot 11H_2O$] and romerite [$Fe^{2+}Fe^{3+}{}_2(SO_4)_4 \cdot 14H_2O$] are refined, hydrogen positions are identified and hydrogen bonding scheme is discussed. The weakest hydrogen bonds are found to occur between layers of differently coordinated tetrahedral groups in both romerite and quenstedtite. The transition from romerite to quenstedtite involves the oxidation of the ferrous iron in romerite converting into a $Fe^{3+}(SO_4) \cdot 5H_2O$ cluster.

Acknowledgement

In loving memory of Terence James O'Connor

1948 - 2012

"I got dark, only to shine."

Table of Contents

List of Figures

List of Tables

Chapter 1

Introduction

1.1 Acid Mine Drainage

The occurrence of acid waters has been reported for centuries (Jambor et al., 2000). These waters have been reported to form naturally in an assortment of environments associated with magmatic gases such as fumaroles, hot springs and crater lakes (Nordstrom et al., 2000). They have also been found to occur naturally through the oxidation of pyrite and other sulfides where they are exposed to the atmosphere through the natural geological cycles of uplift and erosion (Nordstrom et al., 2000). However, the most extensive occurrences of acidic waters on Earth are not formed as a result of such natural processes, but are rather due to the mining, crushing, and subsequent exposure of sulfide bearing deposits (Jambor et al., 2000; Chandra and Gerson, 2010; Hu et al., 2006).

The mining activities expose rock material to air and water in much larger volumes than would occur during the natural weathering process. In an average sulfide mining operation, it is estimated that approximately 98% of all geological material disrupted during the mining process is discarded as waste (Bigham and Nordstrom, 2000). Much of this waste rock is stored on the mine sites as large piles characterized by a heterogeneous mineralogy, but often rich in iron sulfides such as pyrite and pyrrhotite. The remaining 2% undergoes some form of treatment in an effort to extract the desired precious metals. This generates still more waste, which is discarded into large fine-grained slurry impoundments known as tailings (Majzlan et al., 2005; Bigham and Nordstrom, 2000; Nordstrom et al., 2000; Jerz and Rimstidt, 2003).

The exposure of this waste material leads to oxidation of the chemically reactive minerals present in the host rock. In the case of massive sulfide deposits, the most common mineral undergoing oxidation in the waste piles and tailings is pyrite, FeS_2 (Jambor et al., 2000). The oxidation of pyrite is an extremely complex process which typically involves oxidizing bacteria (Bond et al., 2000). The rate of pyrite oxidation is greatly influenced by factors such as available oxygen, surrounding mineralogy, temperatures, pH of associated waters, relative humidity, and surface area of particles (Bigham and Nordstrom, 2000; Nordstrom et al., 2000; Jambor et al., 2000). The general sequence of pyrite oxidation can be described by the following equation:

$$FeS_{2(s)} + {}^{15}/_{4}O_{2(aq)} + {}^{7}/_{2}H_2O_{(l)} \leftrightarrow Fe(OH)_{3(s)} + 2H_2SO_{4(aq)}$$

It can be seen from the above reaction that the outcome of pyrite oxidation is a combination of a ferric hydroxide as well as the formation of sulfuric acid (H_2SO_4). The above equation, however, does not convey the complexity of reaction pathways occurring at any given massive sulfide mine site. These pathways include the proliferation of Fe- and S-oxidizing bacteria, known as chemolithotrophs (Bigham and Nordstrom, 2000; Garcia et al., 2005). These bacteria serve to oxidize the Fe^{2+} ion, forming the Fe^{3+} ion which is a catalyst for further oxidation reactions (Jerz and Rimstidt, 2003; Bond et al., 2000). The sulfur cation also undergoes a process of oxidation, also catalyzing these reactions (Lottermoser, 2007). Some of the electron exchanges involved in the reducing-oxidizing reactions occurring when pyrite is exposed to the elements are presented in Figure 1.1, which also illustrates the complexity of the pyrite oxidation process, and its ultimate outcome: an acidic solution rich in dissolved metal species known as acid mine drainage (AMD) (Hammarstrom et al., 2005).

Waste rock at mine sites is typically found in large rock piles or in tailings ponds. In the case of rock piles the material is coarse, resulting in a small surface area to volume ratio which means a relatively small amount of material is exposed to the elements and undergoing oxidation at one time,

when compared to a finer-grained form of waste such as tailings. However, the coarse material found in a rock pile creates open spaces within the pile through which air can move. As pyrite oxidation is an exothermic process, the air inside the pile can heat up in localized, pyrite rich regions, and air-flow patterns can develop within the pile (Molson et al., 2005). The movement of air throughout the pile works to increase the oxygen supply and provides momentum to the oxidation process, making rock piles significant sources of AMD (Nordstrom et al., 2000; Montero et al., 2005).

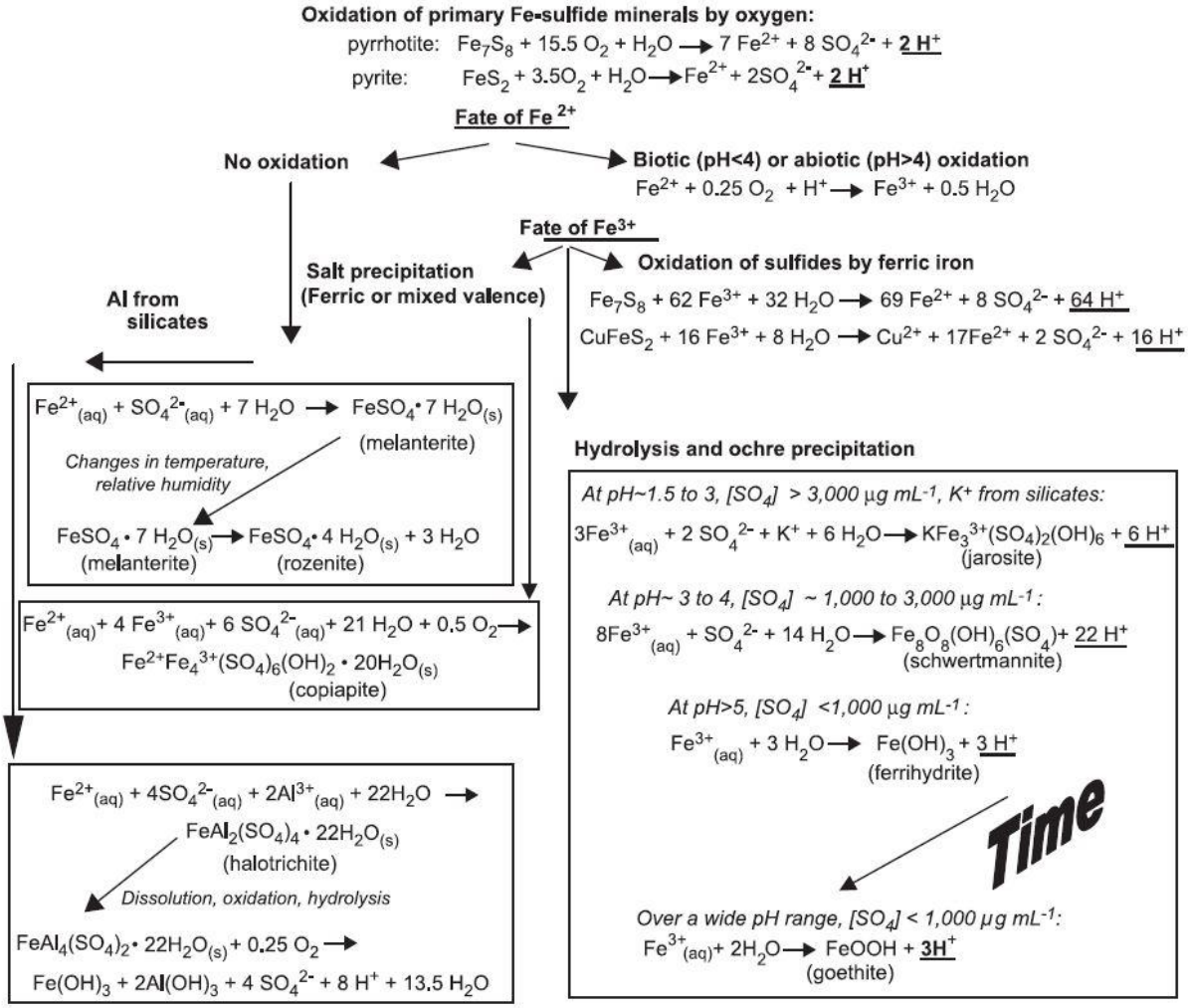

Figure 1.1: Pyrite oxidation processes that lead to the formation of secondary sulfate-mineral and acid mine drainage (taken directly from Hammarstrom et al., 2005)

The production of AMD will be limited, however, by the chemistry of the other materials present in the rock being oxidized. For example, if the waste rock hosts a large variety of calcium carbonates or other neutralizing material, then the production of AMD will be limited or not occur at all (Hill, 1969). If there is no neutralization potential in the surrounding rock, however, then waste rock piles can be a significant source of AMD.

While the waste rock piles at mine sites can generate large volumes of AMD, mine tailings produce much larger concentrations of this potentially toxic material (Nordstrom et al., 2000). The particle size in tailings is much smaller than in rock piles, which means the sulfides have a greater surface area exposed to the oxidation reactions. Tailings are also typically richer in sulfides than rock piles, as they were more closely related to the sulfide ore being sought. Furthermore, tailings are deposited as slurry into large impoundments known as tailings ponds. These ponds are typically submerged in an effort to slow the oxidation rates, and in modern-day mines, ponds may be designed to remain saturated. However, in older mines, periods of drying or fluctuation of the water level allow mass quantities of highly reactive particles to be temporarily exposed. The result is that ferric sulfates are then created and, when the ponds are again submerged, these new compounds risk being flushed into the groundwater as sulfuric acid and dissolved metal species. This problem is intensified by the practice of elevating tailings ponds, which become groundwater recharge zones (Bigham and Nordstrom, 2000).

When AMD is allowed to enter the natural Earth systems, serious damage to aquatic ecosystems results, which has large-scale effects on the ecosystem as a whole (Bigham and Nordstrom, 2000; Liang and Thompson, 2010). AMD is also destructive through the process of increased erosion and sedimentation, which in turn causes further harm to the natural ecosystem. Much effort is being made to mitigate these effects (Natarajan, 2008; Akcil and Koldas, 2006; Hesketh et al., 2010). Some such

mitigation techniques focus on the prevention of the oxidation process from occurring all together, while others focus on containing the AMD generated results (Hesketh et al., 2010).

1. 2 Iron Sulfate Minerals

Pyrite oxidation involves many intermediate processes, some of which result in the formation of iron sulfate minerals. These iron sulfate minerals are generally hydrous and highly soluble (Bigham and Nordstrom, 2000; Posnjak and Merwin, 1922; Bandy, 1938). They form primarily as precipitates from acid sulfate waters and are visible, for example, along the edges of evaporating tailings ponds. They also form as efflorescent blooms on oxidizing material when it is exposed to high relative humidity conditions (Nordstrom and Alpers, 1999; Nordstrom et al., 2000; Jambor et al., 2000). The general sequence of evolution of these soluble salts begins with ferrous sulfate salts, followed by mixed valence sulfates, and finally evolving into purely ferric sulfate salts (Bandy, 1938). The ferric sulfate salts may then undergo evolution through the loss or gain of structural water. An example of this sequence would be:

(Szomolnokite) $Fe^{2+}SO_4 \cdot H_2O \rightarrow$ (Romerite) $Fe^{2+}Fe_2^{3+}(SO_4)_4 \cdot 14H_2O \rightarrow$ (Quenstedtite) $Fe_2^{3+}(SO_4)_3 \cdot 10H_2O \rightarrow$ (Coquimbite) $Fe_2^{3+}(SO_4)_3 \cdot 9H_2O$ (Bandy, 1938)

The final stages of this evolution, the formation of ferric iron sulfates, act as temporary sinks for metals and the sulfate ion. However, the highly soluble nature of metal sulfate salts means that when exposed to rainfall, the ferric and sulfate ions are washed back into the ecosystem in a large, contaminating pulse (Nordstrom and Alpers, 1999). Many studies have shown that when a period of drying (and, therefore, hydrous metal sulfate formation) is followed by rainfall, dissolved metals and sulfate ions enter the ecosystem in a very high concentration which is not tolerated by aquatic ecosystems (Liang and Thompson, 2010; Hammarstrom et al., 2005). Once dissolved, the ferric ion is free to continue the oxidation process of sulfide minerals and the process continues.

Soluble ferric sulfate minerals, where present, are a key component to AMD and pose a considerable threat to aquatic ecosystems (Hammarstrom et al., 2005). It is therefore important that the formation, evolution and dissolution properties of these minerals be well-understood in order to be more successful at mitigating and predicting their effects (Nordstrom et al., 2000). The need to understand ferric sulfates more completely is however not limited to the problem of AMD, as these minerals are also significant to other natural systems on Earth.

1.3 Ferric Sulfates in Art Conservation

While mining operations present the most visible and, arguably, destructive site where ferric sulfates are found on Earth, their occurrence is also noted elsewhere.

One little-mentioned region where pyrite oxidation and the formation of ferrous and ferric sulfates are quite problematic is in the field of Art Conservation (Newman, 1998). The process of pyrite oxidation has been known to affect archeological specimens (Oddy, 1977; Fors and Sandstrom, 2005) as well as any sculpture or stonework made out of a geological material which hosts pyrite (Scott and Eggert, 1948; Oddy, 1977).

The efforts to conserve the materials being affected by pyrite oxidation are often unsuccessful largely due, it is postulated, to the complexity of the pyrite oxidation process (Newman, 1998). If efforts to slow or stifle the process are not successful, then art conservationists are confronted with the task of trying to remove the resultant sulfates. This process involves a great deal of risk for the specimens, as iron sulfates may be easily removed with water, but they will just as easily re-form, continually eating away at the object (Oddy, 1977; Yerrapragada and Chirra, 1996). Therefore, the same need to halt iron sulfate formation confronting the environmental mining engineer when looking at AMD is felt by the art conservationist trying to protect objects of historical significance.

That pyrite oxidation and the formation of ferric sulfates poses a problem not only for the environment, but also in fields somewhat removed from the natural world such as in Art Conservation, presents another reason why ferric sulfates and their formation mechanisms need to be understood. This need is further presented when looking beyond the Earth and to other regions of the solar system.

1.4 Ferric Sulfates on Mars

In January 2004 the Mars Exploration Rovers (MERs), Spirit and Opportunity, landed upon the surface of Mars and began collecting data about the Martian surface. Amongst other instruments, the MERs were equipped with a miniature Mossbauer spectrometer, which is capable of determining the oxidation and coordination states of Fe and, to some extent, the mineralogical composition of Fe-bearing phases (Morris et al., 2006). The collected Mossbauer data indicate that in many of the regions tested by the MERs, there is a larger percentage of ferric iron- and sulfur- bearing minerals the S content came from the APXS instrument, Mossbauer does not give chemical content than had been previously suspected and these minerals often occur in the form of ferric iron sulfates (Marion et al., 2008; Morris et al., 2006; Sefton-Nash and Catling, 2008; Wang et al., 2008). In fact, in some regions, such as at Paso Robles in the Gusev Crater, the MER Spirit detected large volumes of hydrous ferric sulfates of varying hydration states (Yen et al., 2008). This, as well as the earlier detection of geothite [α-FeOOH], a mineral which is known to only grow in the presence of water on Earth, was one of the first real indications of water-related mechanisms occurring on the surface of Mars (Yen et al., 2008; Morris et al., 2006; Lichtenberg et al., 2010). In the Burns formation of Meridiani Planum, the mineral jarosite [$KFe_3(SO_4)_2(OH)_6$] was found in abundance. The presence of this mineral not only indicates water activity, but also acidic conditions (i.e. pH<4.0) (Marion et al., 2008).

Layered sedimentary units of hydrated sulfates in Meridiani Planum were also found, and these were confirmed by the MER Opportunity (Lichtenberg et al., 2010). The mineralogical variation in these deposits suggests a lacustrine system, dominantly acidic, which alternated with a more arid environment (Lichtenberg et al., 2010). Poly-hydrated sulfates, including ferric sulfates, constitute one of the predominant mineralogical groups found in these deposits (Lichtenberg et al., 2010). The Burns formation is in fact estimated to be composed of between 15% and 40% ferric sulfates. (Sefton-Nash and Catling, 2008). Many more occurrences of ferric sulfates on the surface of Mars have been documented, and the abundance of iron sulfate materials on the surface of Mars has sparked a great deal of interest in the formation mechanisms of these minerals. A complete understanding of the conditions under which they form on Earth would provide useful information about the possible environmental evolutionary history of Mars. There is a relative dearth of information about ferric sulfates in general (Marion et al., 2008; Ling and Wang, 2010) and much more work needs to be done before the surficial history of Mars can be understood.

Chapter 2

The Crystal Structures of Normal Ferric Sulfate Hydrates

2.1 Introduction

A wide variety of hydrous ferric sulfates have been identified and several attempts have been made to outline a classification scheme (*eg*., Susse, 1971; Sabelli and Trosti-Ferroni, 1985). One of the simplest systems, which was devised by Posnjak and Merwin in their foundational work, *The System, Ferric Oxide-Sulfur Trioxide-Water, 1922*, consists of separating the sulfates into three groups: basic, normal and acid. Posnjak and Merwin (1922) describe basic ferric sulfates as having a ratio of 3:4, 1:2 or 2:5 of Fe_2O_3 to SO_3. These basic ferric sulfates include butlerite [$Fe_2O_3{\cdot}2SO_3{\cdot}H_2O$] and copiapite [$2Fe_2O_3{\cdot}5SO_3{\cdot}17H_2O$]. Normal hydrous ferric sulfates are those with a Fe_2O_3 to SO_3 ratio of 1:3, such as coquimbite [$Fe_2O_3{\cdot}3SO_3{\cdot}9H_2O$]. Finally, acid ferric sulfates consist of those with a Fe_2O_3 to SO_3 ratio of 1:4 and include the mineral rhomboclase [$Fe_2O_3{\cdot}4SO_3{\cdot}9H_2O$]. Depending on the relative abundance of the starting components (Fe_2O_3, SO_3 and H_2O) and the temperatures to which the materials would be subjected, Posnjak and Merwin (1922) were able to form a wide variety of ferric sulfates, most of which were already recognized as mineral species, though there were a few outlined which had yet to be characterized. One of these previously unidentified sulfates included the ferric sulfate hexahydrate [$Fe_2(SO_4)_3{\cdot}6H_2O$], which will be discussed in depth in the following chapter.

This chapter presents the crystal structures of two sulfates. The first is the mixed-valence iron sulfate known as romerite [$Fe^{2+}Fe^{3+}{}_2(SO_4)_4{\cdot}14H_2O$]. Romerite is known to grow in intimate association with quenstedtite, a normal sulfate [$Fe_2(SO_4)_3{\cdot}11H_2O$] (Bandy, 1938). The atomic structures of quenstedtite's and romerite's crystallography are discussed here and their hydrogen locations, bonds and bonding scheme are presented.

2.2 Quenstedtite and Romerite

Bandy (1938) researched the sulfate mineral assemblages found at three former mine sites in the Atacama Desert, Northern Chile which is one of the driest places on Earth (Bandy, 1938). While sulfates are easily soluble, the high evaporation and low precipitation rates found in desert environments typically allows for a wide range of sulfate minerals to grow, evolve, and persist. These environments provide an excellent opportunity for the study of the complicated phase relationships associated with sulfate formation. At two sites, Alcaparrosa and Quetena, Bandy observed a reoccurring relationship between three hydrous iron sulfates: the mixed hydrous ferrous-ferric iron sulfate romerite, the hydrous ferric iron sulfate quenstedtite, and the hydrous ferric iron sulfate coquimbite. Romerite was seen to form first followed either by quenstedtite and then coquimbite (at Quetena), or by coquimbite and then quenstedtite (at Alcaparrosa). Coquimbite pseudomorphs of quenstedtite were also common.

The crystal structures of both romerite and quenstedtite had been solved in the 1970's but the hydrogen positions were not determined in the case of quenstedtite. It was therefore considered of some importance to pursue a more accurate crystallographic refinement of these two minerals.

Grailich (1858) first identified romerite at Rammelsburg, Germany. Blaas (1883) was the first to examine the mineral with the intention of classifying its crystallography more accurately, and he determined romerite to belong to the triclinic class of minerals. Due to the lack of definite restrains upon how the triclinic axes must relate to each other, there followed some debate about the best way to orient the axes of romerite by Linck (1889), Ungemach (1935) and Wolfe (1937) whose orientation was ultimately settled upon. Fanfani et al. (1970) solved the crystal structure of romerite by single crystal X-ray diffraction analysis. The hydrogen bonds and angles were presented (Fanfani et al., 1970). This study presents an updated crystal structure refinement for romerite, with hydrogen positions,

bonds and angles. This solution was achieved by single-crystal X-ray diffraction, and based on the atomic structure first determined by Fanfani et al. (1970).

Quenstedtite was established to have a triclinic crystal form by Ungemach (1935). Originally, quenstedtite was determined, through weight loss measurements, to have the mineral formula [$Fe_2(SO_4)_3 \cdot 10H_2O$]. However, Thomas et al. (1974), who gathered the first crystallographic data for quenstedtite's atomic arrangement through single crystal X-ray diffraction, found a formula of [$Fe_2(SO_4)_3 \cdot 11H_2O$]. This determination was based on weight loss measurements and crystal structure refinement as well as using information about the electron density to locate the weakly-bonded water molecules. The water molecule in question was defined as zeolitic by Thomas et al. (1974 there is evidence for a variable amount of water within the unit cell. The refinement of the atomic structure performed during this study found quenstedtite to have 11 H_2O molecules, in agreement with Thomas et al (1974). This study also reports the hydrogen positions and hydrogen bonds and angles which was previously unknown for this mineral.

2.2.1 Materials

A sample of quenstedtite was purchased from a mineral dealer and originated from Alcaparossa, Chile. Romerite was also found to occur with quenstedtite in the sample. Minerals were identified using optical microscopy using criteria such as refractive indices, morphology, colour and pleochroism.

2.2.2 Romerite Structure

The structure of romerite includes both ferric and ferrous iron. The ferrous iron is found as isolated octahedra coordinated with 6 H_2O molecules. These ferrous-iron-containing octahedra are located at the cell origin (coincident with its inversion center). The ferric iron is also in octahedral coordination, but it is coordinated by 4 H_2O molecules and two oxygen atoms. Each of these oxygen

atoms coordinating the Fe^{3+} are also part of two different and adjacent SO_4^{2-} groups. These $[Fe(H_2O)_4(OSO_3)_2]^{-1}$ groups are described by Fanfani et al. (1970) as having *cis*-configuration of ligands. These groups are located in the unit cell at ½, ½, ½. The isolated octahedra and the $[Fe(H_2O)_4(OSO_3)_2]^{-1}$ groups are linked together through hydrogen bonding.

2.2.3 Romerite Crystal Structure Refinement

A crystal which exhibited the resinous pinkish-mauve coloration and pleochroism associated with romerite (Dana, 1951; Fanfani et al., 1970) was selected. It was verified to show perfect extinction behavior under crossed polars and was mounted upon a glass fiber to perform spindle stage measurements. The function of the spindle stage is to record the extinction locations of the mineral covering a complete 360° rotation (Bloss, 1980). With this information it is possible to determine the orientation of the crystal's indicatrix so that subsequently its refractive indices can be measured (Gunter et al., 2005). Measurements were taken using the monochromatic light from a sodium vapor lamp (λ=589.3nm). Using the computer program Excalibur (QuickWin V. 5.00, ©1998), the crystal was shown to have a 2V angle of 51°, consistent with romerite (Dana, 1951). The refractive indices measured, using Becke line technique and varying the refractive indecx of the immersion oils were also consistent with those described for romerite.

Crystals from the same sample as that analyzed above, exhibiting the same colour and pleochroism, were collected and placed in a FEI™ scanning electron microscope. Chemical composition was determined by EDS and the results indicated an iron sulfate, with no sign of impurities such as aluminum (Figure 2.1).

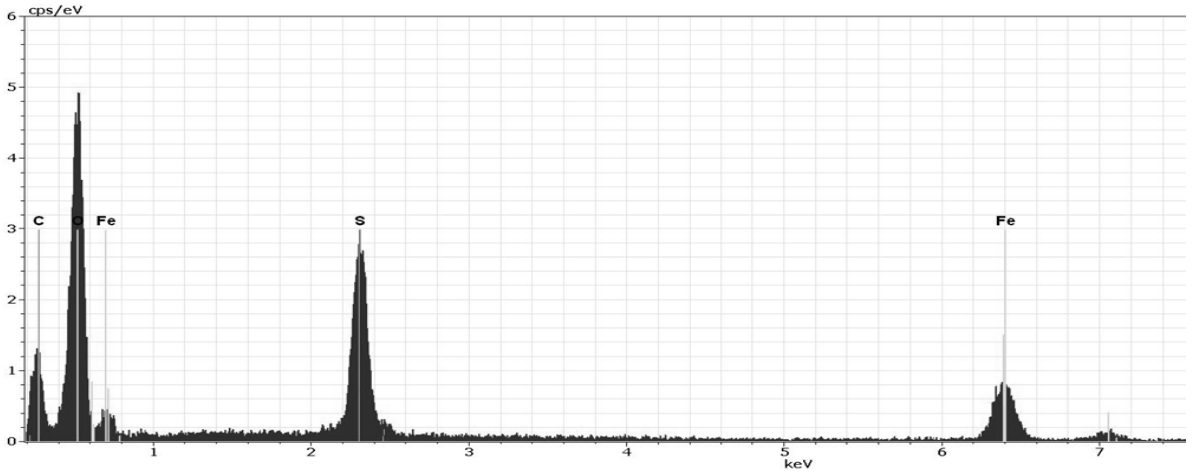

Figure 2.1: Romerite chemistry as determined using EDS analysis. The sample contains Fe, S and O. The C peak is associated with the carbon tack upon which the sample was placed and the small peak to the right of the second Fe peak is also associated with iron.

A grain exhibiting perfect extinction behavior was selected for single crystal X-ray analysis. A Bruker SMART CCD 1000 X-ray diffractometer with graphite-monochromated Mo*Kα* radiation (λ=0.71073 Å), was used over a range of θ 2.68 – 26.0 ° at 25°C to gather the XRD pattern for the crystal. The crystal structure refinement was conducted by Dr. Ruiyao Wang of the Queen's University Chemistry Department, using the program SHELXL-97.

The crystallographic data collected and subsequent structure refinement confirmed the crystal to be romerite, with a $P\bar{1}$ space group, and the unit cell measurements were in excellent agreement with those reported by Fanfani et al. (1970). The cell dimensions for the romerite grain analyzed here are listed in Table 2.1 in comparison with the Fanfani et al. (1970) data, and atomic positional coordinates and bond lengths and angles are reported in Tables 2.2-2.7.

Table 2.1 Romerite unit cell dimensions determined in the present study. These dimensions are listed in comparison with those of Fanfani et al. (1970).

Present Study		Fanfani et al. (1970)	
a- 6.4274(3) Å	α- 89.72°	a- 6.463±0.008 Å	α- 90.32° ± 10.047°
b- 15.2490(7) Å	β- 100.79°	b- 15.309±0.018 Å	β- 101.5° ± 10.047°
c- 6.3464(3) Å	γ- 85.96°	c- 6.341±0.008 Å	γ- 85.44° ± 10.047°

The fragments of the crystal structure of romerite can be seen in Figure 2.2. Displayed in this image is the Fe1 ferrous iron octahedron coordinated with the 6 H_2O molecules to the right. To the left, the Fe2 ferric iron octahedron is coordinated with two sulfate tetrahedra and 4 H_2O molecules. Figure 2.3 shows the unit cell of romerite, where the Fe1 octahedra occupy the corners, and the Fe2 octahedra are located within the unit cell.

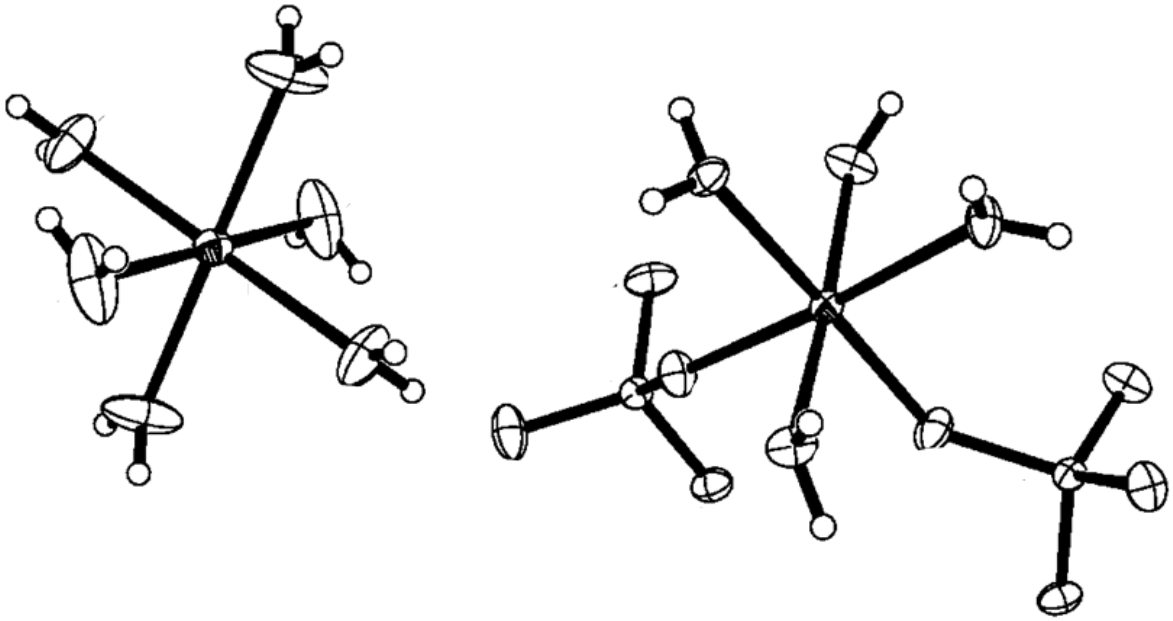

Figure 2.2: Romerite atomic arrangement. The Fe1 octahedron on the left is the site of the Fe^{2+}, while the Fe2 octahedron on the right hosts the Fe^{3+}. The Fe2 octahedron has a *cis* configuration of ligands.

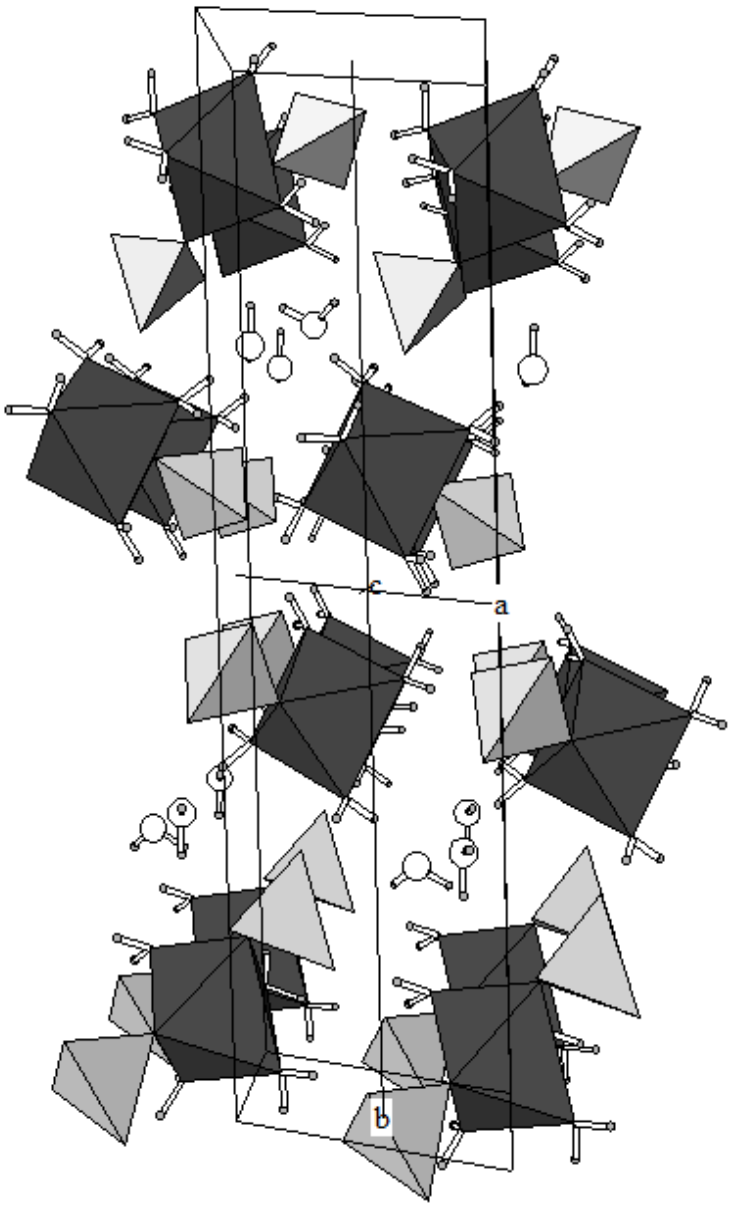

Figure 2.3: Romerite unit cell as seen down the *c* axis. Octahedra are dark grey, while tetrahedra are light grey. The octahedra in the corners of the cell are the Fe1, Fe^{2+} octahedra, coordinated with 6 water molecules, while up the b axis are the Fe2, Fe^{3+} octahedra, each coordinated with 4 water molecules and oxygen atoms belonging to two different sulfate tetrahedra.

Table 2.2. Crystal data and structure refinement parameters for romerite

Mineral Name	Romerite	
Empirical formula	$Fe_3 H_{28} O_{30} S_4$	
Formula weight	804.01 gm	
Temperature	180(2) K	
Wavelength	0.71073 Å	
Crystal system	Triclinic	
Space group	P$\bar{1}$	
Unit cell dimensions	a = 6.4274(3) Å	α= 89.72°.
	b = 15.2490(7) Å	β= 100.79°.
	c = 6.3464(3) Å	γ = 85.96°.
Volume	609.40(5) $Å^3$	
Z	1	
Density (calculated)	2.191 Mg/m^3	
Absorption coefficient	2.230 mm^{-1}	
F(000)	410	
Crystal size	0.25 x 0.15 x 0.08 mm^3	
Theta range for data collection	2.68 to 26.00°.	
Index ranges	-7<=h<=7, -18<=k<=18, -7<=l<=7	
Reflections collected	5995	
Independent reflections	2370 [R(int) = 0.0146]	
Completeness to theta = 26.00°	99.5 %	
Absorption correction	Multi-scan	
Max. and min. transmission	0.8418 and 0.6056	
Refinement method	Full-matrix least-squares on F^2	
Data / restraints / parameters	2370 / 13 / 229	
Goodness-of-fit on F^2	1.043	
Final R indices [I>2sigma(I)]	R1 = 0.0199, wR2 = 0.0546	
R indices (all data)	R1 = 0.0207, wR2 = 0.0551	
Largest diff. peak and hole	0.313 and -0.400 $e.Å^{-3}$	

Table 2.3. Atomic coordinates (x 10^4) and equivalent isotropic displacement parameters ($Å^2$x 10^3) for romerite. U(eq) is defined as one third of the trace of the orthogonalized U^{ij} tensor.

	x	y	z	U(eq)
Fe(1)	0	0	0	16(1)
Fe(2)	3414(1)	3197(1)	5970(1)	11(1)
S(1)	5952(1)	1674(1)	3652(1)	13(1)
S(2)	7628(1)	3864(1)	9083(1)	12(1)
O(1)	4336(2)	2073(1)	4864(2)	17(1)
O(1W)	2460(3)	514(1)	-1321(4)	41(1)
O(2)	5859(2)	2194(1)	1676(2)	22(1)
O(2W)	1134(3)	489(1)	3090(3)	31(1)
O(3)	8095(2)	1694(1)	4974(2)	18(1)
O(3W)	1803(3)	-1170(1)	906(3)	40(1)
O(4)	5411(2)	773(1)	3218(2)	24(1)
O(4W)	2598(2)	2539(1)	8459(2)	18(1)
O(5)	6269(2)	3284(1)	7588(2)	19(1)
O(5W)	364(2)	3084(1)	4459(2)	16(1)
O(6)	6421(2)	4222(1)	10656(2)	18(1)
O(6W)	2231(2)	4352(1)	7000(2)	18(1)
O(7)	8276(2)	4568(1)	7805(2)	20(1)
O(7W)	3824(2)	3881(1)	3390(2)	19(1)
O(8)	9504(2)	3311(1)	10139(2)	16(1)

Table 2.4. Bond lengths [Å] and angles [°] for romerite.

Fe(1)-O(3W) (X2)	2.0746(16)	O(1)-Fe(2)-O(7W)	93.56(6)
Fe(1)-O(1W) (X2)	2.1169(17)	O(5)-Fe(2)-O(6W)	94.93(6)
Fe(1)-O(2W) (X2)	2.1183(15)	O(1)-Fe(2)-O(6W)	175.68(6)
Fe(2)-O(5)	1.9414(13)	O(7W)-Fe(2)-O(6W)	86.26(6)
Fe(2)-O(1)	1.9506(13)	O(5)-Fe(2)-O(5W)	176.22(6)
Fe(2)-O(7W)	2.0051(14)	O(1)-Fe(2)-O(5W)	91.54(6)
Fe(2)-O(6W)	2.0286(14)	O(7W)-Fe(2)-O(5W)	87.61(6)
Fe(2)-O(5W)	2.0343(13)	O(6W)-Fe(2)-O(5W)	84.14(6)
Fe(2)-O(4W)	2.0362(13)	O(5)-Fe(2)-O(4W)	90.78(6)
S(1)-O(4)	1.4560(14)	O(1)-Fe(2)-O(4W)	89.03(6)
S(1)-O(2)	1.4699(13)	O(7W)-Fe(2)-O(4W)	172.77(6)
S(1)-O(3)	1.4748(13)	O(6W)-Fe(2)-O(4W)	90.65(6)
S(1)-O(1)	1.5021(13)	O(5W)-Fe(2)-O(4W)	85.57(6)
S(2)-O(6)	1.4606(13)	O(4)-S(1)-O(2)	112.35(9)
S(2)-O(8)	1.4703(13)	O(4)-S(1)-O(3)	110.91(8)
S(2)-O(7)	1.4716(13)	O(2)-S(1)-O(3)	108.78(8)
S(2)-O(5)	1.5000(13)	O(4)-S(1)-O(1)	106.21(8)
		O(2)-S(1)-O(1)	108.92(8)
O(3W)-Fe(1)-O(1W) (X2)	87.92(8)	O(3)-S(1)-O(1)	109.60(8)
O(3W)-Fe(1)-O(1W) (X2)	92.08(8)	O(6)-S(2)-O(8)	110.88(8)
O(3W)-Fe(1)-O(2W) (X2)	91.22(7)	O(6)-S(2)-O(7)	111.29(8)
O(3W)-Fe(1)-O(2W) (X2)	88.78(7)	O(8)-S(2)-O(7)	110.04(8)
O(1W)-Fe(1)-O(2W) (X2)	93.15(8)	O(6)-S(2)-O(5)	109.18(8)
O(1W)-Fe(1)-O(2W) (X2)	86.85(8)	O(8)-S(2)-O(5)	106.99(8)
O(5)-Fe(2)-O(1)	89.38(6)	O(7)-S(2)-O(5)	108.33(8)
O(5)-Fe(2)-O(7W)	95.99(6)		

:

Table 2.5. Anisotropic displacement parameters ($Å^2 x\ 10^3$)for romerite. The anisotropic displacement factor exponent takes the form: $-2\pi^2[\ h^2 a^{*2} U^{11} + ... + 2\ h\ k\ a^*\ b^*\ U^{12}\ ]$

	U^{11}	U^{22}	U^{33}	U^{23}	U^{13}	U^{12}
Fe(1)	16(1)	16(1)	15(1)	-1(1)	3(1)	2(1)
Fe(2)	10(1)	13(1)	11(1)	-1(1)	2(1)	0(1)
S(1)	11(1)	14(1)	12(1)	-1(1)	3(1)	1(1)
S(2)	9(1)	13(1)	12(1)	-1(1)	2(1)	0(1)
O(1)	17(1)	16(1)	21(1)	-5(1)	9(1)	0(1)
O(1W)	40(1)	29(1)	67(1)	-22(1)	37(1)	-13(1)
O(2)	20(1)	32(1)	15(1)	6(1)	4(1)	5(1)
O(2W)	19(1)	45(1)	29(1)	-19(1)	1(1)	2(1)
O(3)	14(1)	22(1)	17(1)	3(1)	1(1)	-1(1)
O(3W)	66(1)	36(1)	18(1)	10(1)	19(1)	31(1)
O(4)	21(1)	17(1)	38(1)	-11(1)	11(1)	-3(1)
O(4W)	14(1)	24(1)	15(1)	2(1)	6(1)	3(1)
O(5)	12(1)	23(1)	21(1)	-6(1)	-1(1)	-2(1)
O(5W)	13(1)	21(1)	14(1)	2(1)	0(1)	-5(1)
O(6)	17(1)	18(1)	22(1)	-4(1)	10(1)	-1(1)
O(6W)	14(1)	18(1)	24(1)	-8(1)	7(1)	-2(1)
O(7)	17(1)	18(1)	25(1)	5(1)	9(1)	2(1)
O(7W)	20(1)	20(1)	21(1)	6(1)	12(1)	5(1)
O(8)	12(1)	23(1)	14(1)	2(1)	1(1)	3(1)

Table 2.6. Hydrogen coordinates (x 10^4) and isotropic displacement parameters ($Å^2$x 10^3) for romerite.

	x	y	z	U(eq)
H(1)	3180(50)	230(19)	-1890(50)	57(10)
H(2A)	3090(80)	550(50)	-180(50)	59(16)
H(2B)	2720(100)	984(16)	-1480(110)	59(16)
H(3)	2300(30)	570(20)	3450(50)	50(9)
H(4)	550(50)	740(20)	3850(50)	54(10)
H(5)	1840(50)	-1354(19)	2000(50)	39(8)
H(6)	2290(50)	-1520(20)	210(50)	48(9)
H(7)	3570(50)	2402(19)	9510(50)	42(8)
H(8)	1660(50)	2742(19)	8830(50)	34(8)
H(9)	-220(40)	2722(19)	4710(40)	28(7)
H(10)	110(40)	3184(16)	3130(50)	27(6)
H(11)	2790(50)	4680(20)	7680(50)	41(9)
H(12)	920(50)	4397(19)	7190(50)	43(8)
H(13)	3310(50)	4340(20)	3090(50)	48(9)
H(14)	4730(50)	3802(18)	2680(50)	34(7)

Table 2.7. Hydrogen bonds for romerite [Å and °].

D-H...A	d(D-H)	d(H...A)	d(D...A)	<(DHA)
O(1W)-H(1)...O(4)#2	0.753(19)	1.99(2)	2.726(2)	164(4)
O(1W)-H(2A)...O(4)	0.76(2)	2.42(2)	3.182(3)	172(8)
O(2W)-H(3)...O(4)	0.758(19)	2.08(2)	2.799(2)	159(3)
O(2W)-H(4)...O(3)#3	0.75(2)	2.28(2)	3.002(2)	159(3)
O(3W)-H(5)...O(3)#4	0.75(3)	1.98(3)	2.719(2)	173(3)
O(3W)-H(6)...O(2)#2	0.78(3)	2.07(4)	2.828(2)	165(3)
O(4W)-H(7)...O(2)#5	0.84(3)	1.82(3)	2.659(2)	174(3)
O(4W)-H(8)...O(8)#3	0.74(3)	1.90(3)	2.6369(19)	172(3)
O(5W)-H(9)...O(3)#3	0.72(3)	1.99(3)	2.707(2)	172(3)
O(5W)-H(10)...O(8)#6	0.84(3)	1.87(3)	2.7091(19)	175(2)
O(6W)-H(11)...O(6)#7	0.73(3)	2.02(3)	2.740(2)	165(3)
O(6W)-H(12)...O(7)#3	0.87(3)	1.82(3)	2.6836(19)	174(3)
O(7W)-H(13)...O(7)#8	0.76(3)	1.92(3)	2.673(2)	173(3)
O(7W)-H(14)...O(6)#9	0.80(3)	1.96(3)	2.6957(18)	151(3)
O(7W)-H(14)...O(2)	0.80(3)	2.62(3)	3.098(2)	119(2)

Symmetry transformations used to generate equivalent atoms:

#1 -x,-y,-z #2 -x+1,-y,-z #3 x-1,y,z #4 -x+1,-y,-z+1

#5 x,y,z+1 #6 x-1,y,z-1 #7 -x+1,-y+1,-z+2

#8 -x+1,-y+1,-z+1 #9 x,y,z-1

2.2.4 Bond Valence Summation Romerite

Using the structure determined, the bond valence environment was analyzed using VaList V. 4.0.7, © 1998-2010. The purpose of performing a bond valence analysis is to confirm that the assumed valence states of the cations located in the crystal structure are correct. Table 2.8 shows that the bond valence summation is in good agreement with the assumed valence states of the cations found in romerite. In Table 2.9 are the cation-anion bonds separated into individual polyhedra. The first polyhedron, the Fe1 octahedron, demonstrates bond lengths consistent with Fe-O bonds where the O anion is part of a water molecule (Thomas et al., 1974; Fanfani et al., 1970; Majzlan, 2005). In the case of these Fe-OW bonds there is a slight lengthening of the bond, making these bonds a little longer than 2.00Å. This is evident when compared with the Fe-O bonds found in Fe2, where the coordinating oxygen atom is not a part of a water molecule (Fe2-O5, Fe2-O1). These bonds are slightly shorter, being less than 2.00Å by approximately 0.05Å.

The lengths of the bonds within the sulfate tetrahedra in romerite are consistent with other reported sulfate structures (Robinson and Fang, 1973; Thomas et al., 1974). The average bond length for the S-O bonds not sharing bridging oxygen with the Fe2 octahedron is 1.467Å. The two O atoms being shared with the Fe2 octahedron have slightly longer lengths, an average of 1.501Å. This is also consistent with the other sulfate structures (Table 2.10).

Table 2.8: Bond valence summation of the cations found in the present study of romerite.

Atom	Valence State Assumed	Bond Valence Summation	% deviation from assumed valence state
Fe1	Fe1(2)	2.02	1
Fe2	Fe2(3)	3.083	3
S1	S1(6)	5.978	0
S2	S2(6)	5.976	0

Table 2.9: Cation-anion bonds located in romerite, separated according to individual polyhedra.

Bond	Length	Oxidation State	Ro	B	S
Fe1_O3W[O](x2)	2.075	Fe(2)	1.7	0.37	0.363
Fe1_O1W[O](x2)	2.117	Fe(2)	1.7	0.37	0.324
Fe1_O2W[O](x2)	2.118	Fe(2)	1.7	0.37	0.323
					Sum= 2.02
Fe2_O5	1.941	Fe(3)	1.751	0.37	0.598
Fe2_O1	1.951	Fe(3)	1.751	0.37	0.582
Fe2_O7W[O]	2.005	Fe(3)	1.751	0.37	0.503
Fe2_O6W[O]	2.029	Fe(3)	1.751	0.37	0.472
Fe2_O5W[O]	2.034	Fe(3)	1.751	0.37	0.465
Fe2_O4W[O]	2.036	Fe(3)	1.751	0.37	0.463
					Sum= 3.083
S1_O4	1.456	S(6)	1.624	0.37	1.575
S1_O2	1.470	S(6)	1.624	0.37	1.516
S1_O3	1.475	S(6)	1.624	0.37	1.496
S1_O1	1.502	S(6)	1.624	0.37	1.391
					Sum= 5.978
S2_O6	1.461	S(6)	1.624	0.37	1.554
S2_O8	1.470	S(6)	1.624	0.37	1.516
S2_O7	1.472	S(6)	1.624	0.37	1.508
S2_O5	1.500	S(6)	1.624	0.37	1.398
					Sum= 5.976

The bonds of the romerite structure reported here are in good agreement with those found by Fanfani et al. (1970) and are shown as a comparison in Table 2.10. This study used the same atom labels as those of Fanfani et al. (1970).

Table 2.10: The bond lengths reported for romerite by Fanfani et al. (1970) in direct comparison to those determined in the present study.

	Fanfani et al.	This Study		Fanfani et al.	This Study
Fe1_O1W	2.141	2.118	S1_O1	1.501	1.502
Fe1_O2W	2.118	2.117	S1_O2	1.496	1.470
Fe1_O3W	2.076	2.075	S1_O3	1.469	1.472
Mean=	*2.112*	*2.103*	S1_O4	1.450	1.470
			Mean=	*1.479*	*1.479*
Fe2_O1	1.945	1.951			
Fe2_O5	1.933	1.941	S2_O5	1.497	1.500
Fe2_O4W	2.047	2.036	S2_O6	1.458	1.461
Fe2_O5W	2.035	2.034	S2_O7	1.466	1.487
Fe2_O6W	2.025	2.029	S2_O8	1.467	1.470
Fe2_O7W	2.023	2.005	*Mean=*	*1.472*	*1.4795*
Mean=	*2.000*	*2.000*			

2.2.5 Quenstedtite Structure

The structure of quenstedtite, as initially determined by Thomas et al. (1974) and refined here, is composed of two isolated cluster types. The first cluster type consists of a ferric iron octahedron sharing two of its corners with one of two sulfate tetrahedra and the other four corners being occupied by water molecules. The result is a $[Fe(H_2O)_4(SO_4)_2]^{-1}$ group. Thomas et al. (1974) refers to this first cluster type as type A. The second cluster consists of a ferric iron octahedron sharing just one corner with a sulfate tetrahedron and the other five corners being occupied by water molecules resulting in a formulation of $[Fe(H_2O)_5(SO_4)]^{-1}$ (referred to as type B). These two cluster types are arranged along the *b* axis in an …AABBAA… arrangement (Thomas et al., 1974). The two remaining water molecules are not coordinating any polyhedra (free waters) and are located between A and B layers. Each cluster is isolated from each other, but all are connected through hydrogen bonding.

2.2.6 Quenstedtite Crystal Structure Refinement

Pale violet crystals with a tabular morphology were identified as possible quenstedtite grains (Dana, 1951; Bandy, 1938). Spindle stage measurements were recorded on samples showing perfect extinction. Measurements were taken using the monochromatic light from a sodium vapor lamp (λ=589.3nm). Using the computer program Excalibur©, the crystal's indicatrix was found. This sample was shown to have a 2V angle of 74°, consistent with that reported for quenstedtite (Dana, 1951; Bandy, 1938). Refractive indices measurements using liquids of known refractive indices and the Becke line method were similar to those observed for quenstedtite (Dana, 1951).

Crystals from the same sample were analyzed through EDS analysis to confirm mineral chemistry. The results indicated an iron sulfate. As seen in Figure 2.4, there was a small amount of calcium present, but this impurity is not believed to be internal to the quenstedtite structure and was likely due to gypsum dust contaminating the surface of the sample crystals (Figure 2.5).

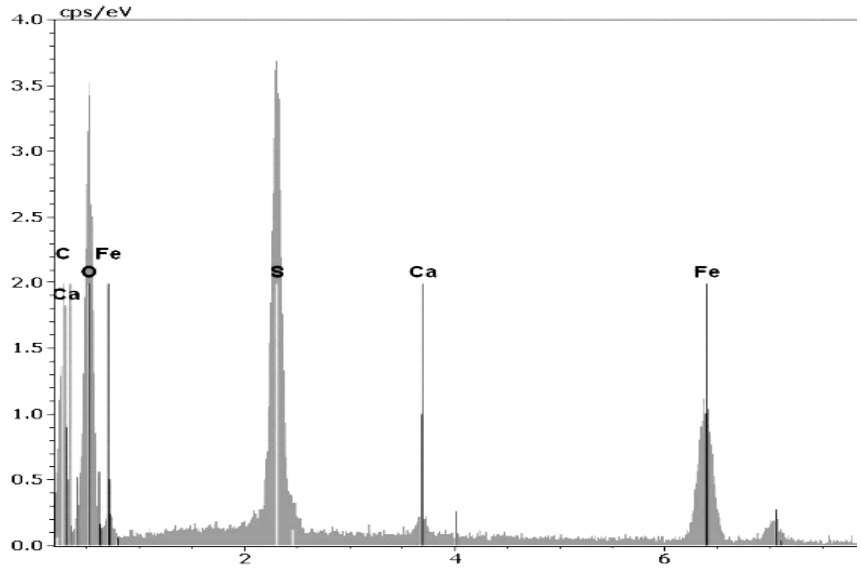

Figure 2.4: The EDS analysis of the quenstedtite grains gathered from the same sample as the crystal submitted for single crystal X-ray analysis. The Ca peak is explained by the gypsum dust coating the quenstedtite grains as seen in figure 2.5.

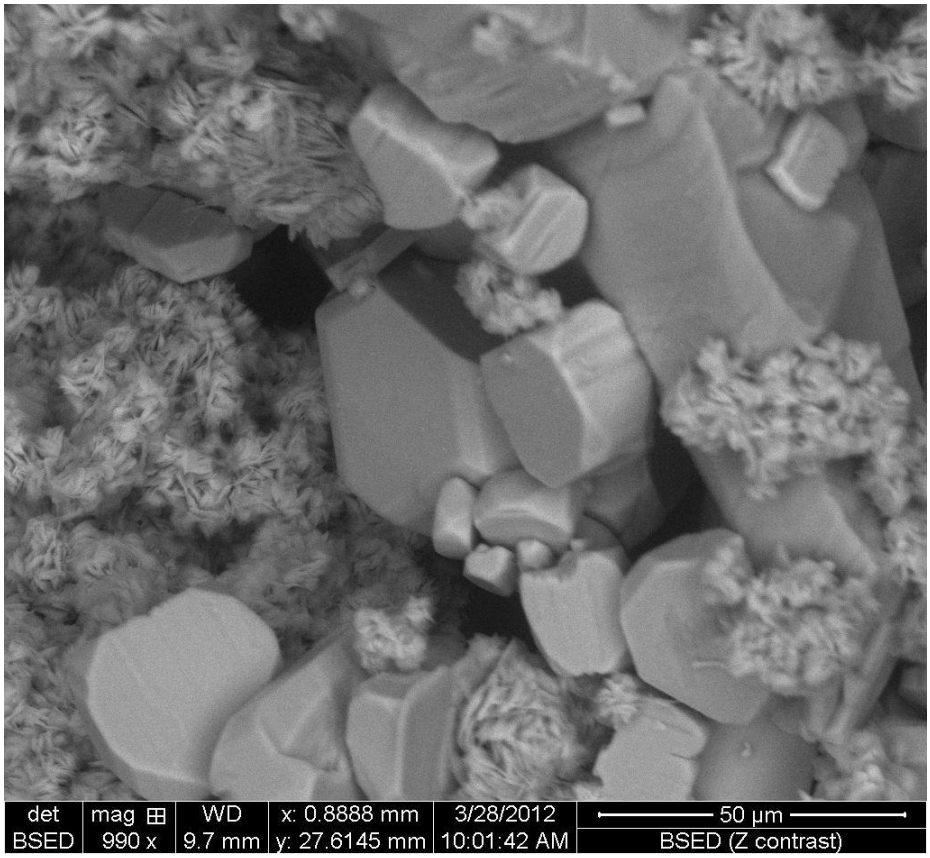

Figure 2.5: SEM image of quenstedtite crystals. The large crystals are of quenstedtite, while the small crystal grains were identified to be gypsum through EDS analysis as well as optical microscopy on larger grains.

A Bruker SMART CCD 1000 X-ray diffractometer with graphite-monochromated MoKα radiation (λ=0.71073 Å), over a range of θ 1.75 – 25.0 ° at -93.15°C was used.

The unit cell dimensions were found to be in good agreement with those of Thomas, et al. (1974) (Table 2.11). The cell was refined by Dr. Ruiyao Wang of Queen's University and the resulting data can be seen in Tables 2.12-2.17.

Table 2.11: Quenstedtite unit cell dimensions as determined in this study shown in comparison with those of Thomas et al. (1974).

Present Study		Thomas et al. (1974)	
a- 6.1741(1) Å	α- 95.633(1)°	a- 6.184(5) Å	α- 94.18(8)°
b- 23.5062(4) Å	β- 101.553(2)°	b- 23.60(2) Å	β- 101.73(8)°
c- 6.5282(1) Å	γ- 93.745(2)°	c- 6.539(5) Å	γ- 96.27(8)°

The atomic arrangement of quenstedtite, as refined in this study can be seen in Figure 2.6. Figure 2.7 shows the layered nature of the quenstedtite structure. The AA…BB layers are separated by the two free water molecules (hatched circles). A drawing of the crystal structure shows the layered nature of the arrangement of the clusters in Figure 2.7.

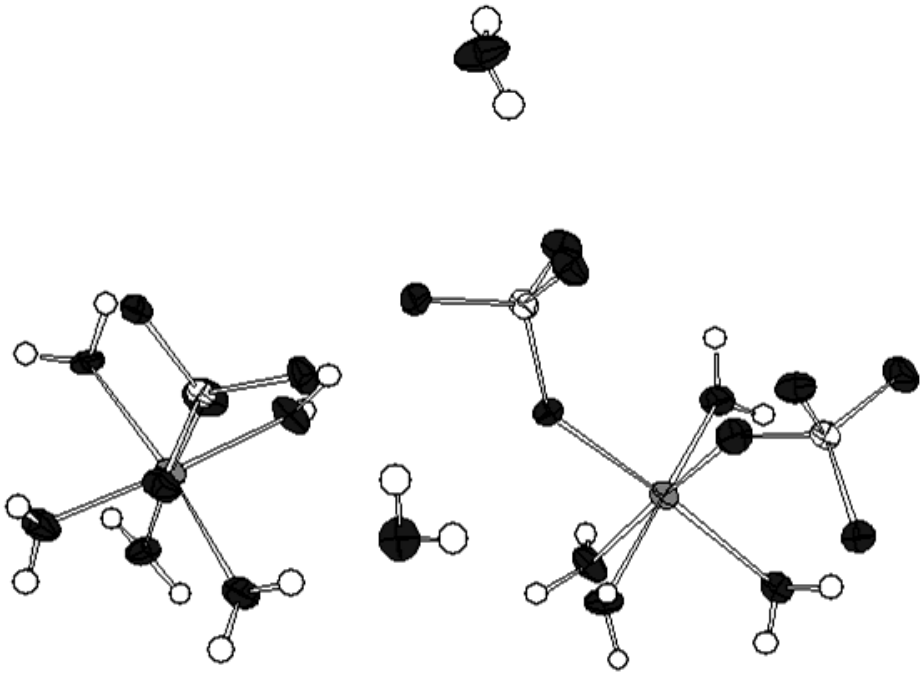

Figure 2.6: Quenstedtite atomic arrangement. The octahedra on the left is the 'B' unit, coordinated with one sulfate tetrahedron and 5 water molecules. The octahedra on the right is the 'A' unit, coordinated with two sulfate tetrahedra and 4 water molecules. Center top and bottom show the 2 water molecules not bound to a polyhedron.

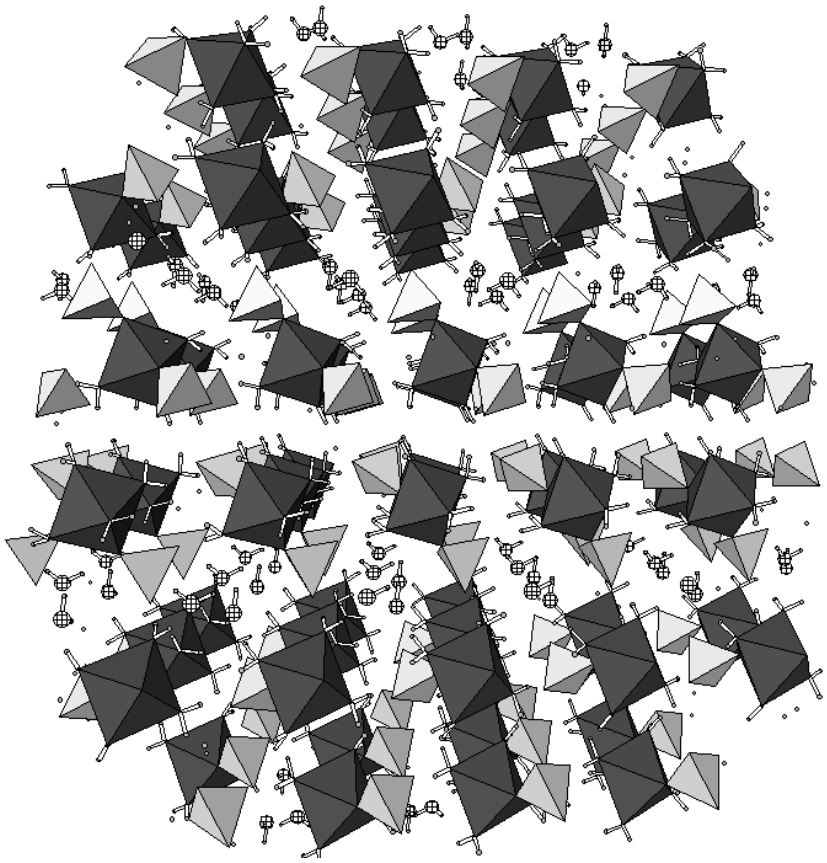

Figure 2.7 The quenstedtite AA..BB layers. Separating the layers are the two free water molecules (hatched circles).

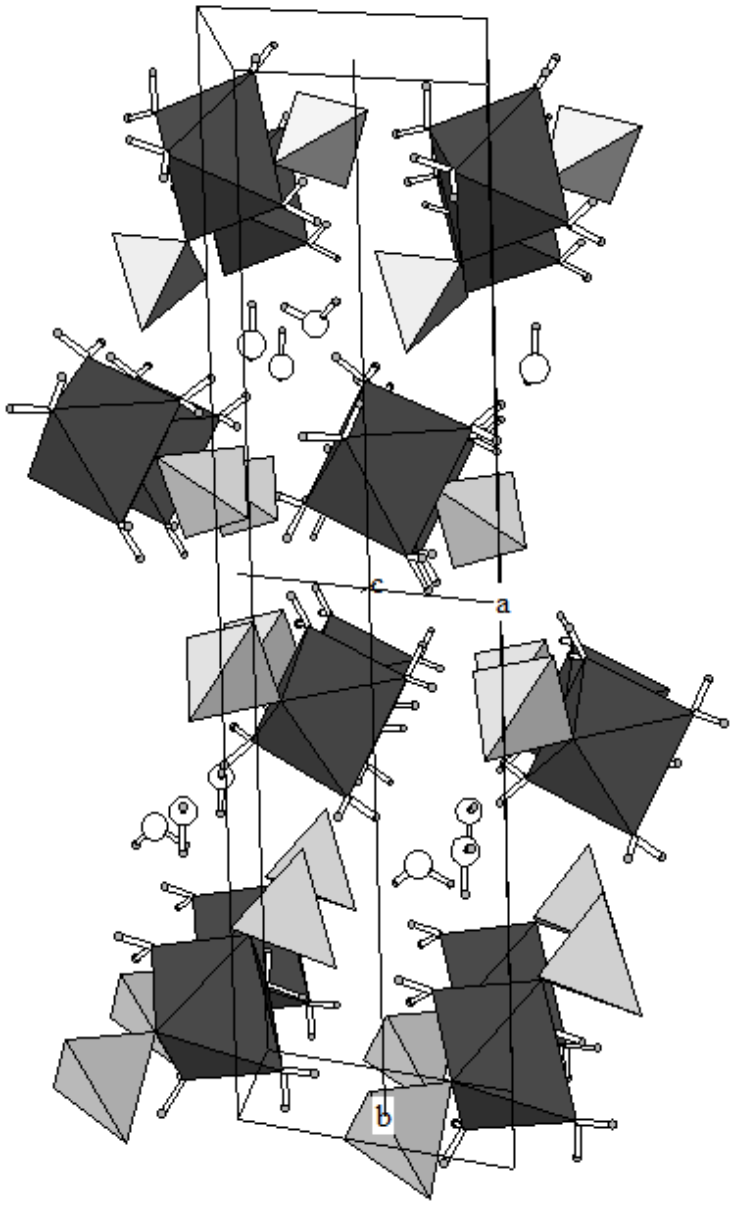

Figure 2.8: Quenstedtite unit cell as viewed down the c axis. The ...AABBAA... ordering of the structure can be seen here, with the A and B layers being separated by the "free" water molecules (open circles). The 'A' units are on the bottom and top, while the two layers in the center of the cell are the 'B' units.

Table 2.12. Crystal data and structure refinement for quenstedtite

Mineral name	Quenstedtite	
Empirical formula	H_{22} Fe_2 O_{23} S_3	
Formula weight	598.06 gm	
Temperature	180(2) K	
Wavelength	0.71073 Å	
Crystal system	Triclinic	
Space group	$P\bar{1}$	
Unit cell dimensions	a = 6.1741(1) Å	α =85.633(1)°.
	b = 23.5062(4) Å	β = 101.553(2)°.
	c = 6.5282(1) Å	γ = 83.745(2)°.
Volume	918.03(3) $Å^3$	
Z	2	
Density (calculated)	2.164 Mg/m^3	
Absorption coefficient	2.034 mm^{-1}	
F(000)	612	
Crystal size	0.08 x 0.04 x 0.02 mm^3	
Theta range for data collection	1.75 to 25.00°.	
Index ranges	-4<=h<=7, -27<=k<=27, -7<=l<=6	
Reflections collected	5946	
Independent reflections	3147 [R(int) = 0.0456]	
Completeness to theta = 25.00°	97.2 %	
Absorption correction	Multi-scan	
Max. and min. transmission	0.9604 and 0.8542	
Refinement method	Full-matrix least-squares on F^2	
Data / restraints / parameters	3147 / 34 / 307	
Goodness-of-fit on F^2	0.946	
Final R indices [I>2sigma(I)]	R1 = 0.0412, wR2 = 0.0848	
R indices (all data)	R1 = 0.0653, wR2 = 0.0945	
Largest diff. peak and hole	0.788 and -0.658 $e.Å^{-3}$	

Table 2.13. Atomic coordinates (x 10^4) and equivalent isotropic displacement parameters ($Å^2$x 10^3) for quenstedtite. U(eq) is defined as one third of the trace of the orthogonalized U^{ij} tensor.

	x	y	z	U(eq)
Fe(1)	320(1)	1185(1)	2559(1)	16(1)
Fe(2)	6387(1)	3855(1)	8352(1)	16(1)
S(1)	-2375(2)	2191(1)	4566(2)	17(1)
O(1)	-1102(6)	1936(1)	3045(6)	22(1)
O(2)	-937(6)	2162(1)	6655(6)	23(1)
O(3)	-4248(5)	1861(1)	4678(6)	21(1)
O(4)	-3127(6)	2789(1)	3717(6)	21(1)
S(2)	3718(2)	737(1)	7096(2)	14(1)
O(5)	1974(6)	1085(2)	5435(6)	26(1)
O(6)	2686(6)	277(1)	8041(6)	26(1)
O(7)	5514(6)	504(1)	6153(6)	21(1)
O(8)	4474(6)	1124(1)	8669(6)	22(1)
S(3)	9446(2)	4226(1)	12613(2)	16(1)
O(9)	7676(5)	3972(2)	11214(6)	24(1)
O(10)	10586(5)	3773(1)	14258(6)	21(1)
O(11)	10979(6)	4444(1)	11408(6)	23(1)
O(12)	8332(6)	4697(1)	13525(6)	27(1)
O(1W)	-1236(6)	1299(2)	-499(6)	21(1)
O(2W)	1705(7)	429(2)	1819(6)	24(1)
O(3W)	-2159(5)	770(1)	3168(6)	18(1)
O(4W)	2688(5)	1602(2)	1572(6)	18(1)
O(5W)	3394(6)	4269(2)	8441(7)	24(1)
O(6W)	5083(6)	3682(1)	5424(6)	19(1)
O(7W)	9242(6)	3477(2)	7885(6)	24(1)
O(8W)	5565(6)	3134(2)	9534(6)	23(1)
O(9W)	7028(7)	4617(2)	7105(6)	27(1)
O(10W)	3218(7)	2514(2)	7079(8)	35(1)
O(11W)	1390(7)	2871(2)	1328(7)	36(1)

Table 2.14. Bond lengths [Å] and angles [°] for quenstedtite.

Fe(1)-O(5)	1.933(4)	O(9)-Fe(2)-O(7W)	92.67(16)
Fe(1)-O(1)	1.961(3)	O(8W)-Fe(2)-O(7W)	93.18(16)
Fe(1)-O(3W)	1.989(3)	O(9)-Fe(2)-O(5W)	93.62(16)
Fe(1)-O(1W)	2.018(4)	O(8W)-Fe(2)-O(5W)	90.55(16)
Fe(1)-O(2W)	2.021(3)	O(7W)-Fe(2)-O(5W)	172.89(17)
Fe(1)-O(4W)	2.026(3)	O(9)-Fe(2)-O(6W)	176.46(15)
Fe(2)-O(9)	1.931(4)	O(8W)-Fe(2)-O(6W)	90.71(16)
Fe(2)-O(8W)	1.969(3)	O(7W)-Fe(2)-O(6W)	85.83(16)
Fe(2)-O(7W)	1.976(3)	O(5W)-Fe(2)-O(6W)	88.08(17)
Fe(2)-O(5W)	2.006(3)	O(9)-Fe(2)-O(9W)	94.84(16)
Fe(2)-O(6W)	2.011(4)	O(8W)-Fe(2)-O(9W)	176.41(18)
Fe(2)-O(9W)	2.022(3)	O(7W)-Fe(2)-O(9W)	90.22(17)
S(1)-O(4)	1.461(3)	O(5W)-Fe(2)-O(9W)	85.95(16)
S(1)-O(2)	1.463(4)	O(6W)-Fe(2)-O(9W)	88.38(16)
S(1)-O(3)	1.472(3)	O(4)-S(1)-O(2)	110.6(2)
S(1)-O(1)	1.505(4)	O(4)-S(1)-O(3)	112.2(2)
S(2)-O(7)	1.449(4)	O(2)-S(1)-O(3)	109.5(2)
S(2)-O(8)	1.465(4)	O(4)-S(1)-O(1)	105.7(2)
S(2)-O(6)	1.470(3)	O(2)-S(1)-O(1)	110.6(2)
S(2)-O(5)	1.486(4)	O(3)-S(1)-O(1)	108.2(2)
S(3)-O(11)	1.456(4)	O(7)-S(2)-O(8)	111.8(2)
S(3)-O(10)	1.463(3)	O(7)-S(2)-O(6)	111.4(2)
S(3)-O(12)	1.467(4)	O(8)-S(2)-O(6)	109.9(2)
S(3)-O(9)	1.487(4)	O(7)-S(2)-O(5)	108.9(2)
O(1W)-H(1WA)	0.804(19)	O(8)-S(2)-O(5)	106.7(2)
O(1W)-H(1WB)	0.821(19)	O(6)-S(2)-O(5)	107.9(2)
O(2W)-H(2WA)	0.816(19)	O(11)-S(3)-O(10)	111.5(2)
O(2W)-H(2WB)	0.817(19)	O(11)-S(3)-O(12)	110.3(2)
O(3W)-H(3WA)	0.811(19)	O(10)-S(3)-O(12)	110.5(2)
O(3W)-H(3WB)	0.837(19)	O(11)-S(3)-O(9)	110.1(2)
O(4W)-H(4WA)	0.850(19)	O(10)-S(3)-O(9)	107.3(2)
O(4W)-H(4WB)	0.844(19)	O(12)-S(3)-O(9)	107.1(2)
O(5W)-H(5WA)	0.836(19)	Fe(1)-O(1W)-H(1WA)	129(4)

O(5W)-H(5WB)	0.828(19)	Fe(1)-O(1W)-H(1WB)	113(4)
O(6W)-H(6WA)	0.806(19)	H(1WA)-O(1W)-H(1WB)	108(3)
O(6W)-H(6WB)	0.832(19)	Fe(1)-O(2W)-H(2WA)	124(3)
O(7W)-H(7WA)	0.822(19)	Fe(1)-O(2W)-H(2WB)	128(3)
O(7W)-H(7WB)	0.850(19)	H(2WA)-O(2W)-H(2WB)	106(3)
O(8W)-H(8WA)	0.811(19)	Fe(1)-O(3W)-H(3WA)	140(3)
O(8W)-H(8WB)	0.811(19)	Fe(1)-O(3W)-H(3WB)	117(3)
O(9W)-H(9WA)	0.826(19)	H(3WA)-O(3W)-H(3WB)	104(3)
O(9W)-H(9WB)	0.819(19)	Fe(1)-O(4W)-H(4WA)	120(3)
O(10W)-H(10A)	0.812(19)	Fe(1)-O(4W)-H(4WB)	117(3)
O(10W)-H(10B)	0.825(19)	H(4WA)-O(4W)-H(4WB)	99(3)
O(11W)-H(11A)	0.851(19)	Fe(2)-O(5W)-H(5WA)	123(3)
O(11W)-H(11B)	0.863(18)	Fe(2)-O(5W)-H(5WB)	134(3)
		H(5WA)-O(5W)-H(5WB)	103(3)
O(5)-Fe(1)-O(1)	89.79(16)	Fe(2)-O(6W)-H(6WA)	120(4)
O(5)-Fe(1)-O(3W)	94.59(16)	Fe(2)-O(6W)-H(6WB)	120(4)
O(1)-Fe(1)-O(3W)	93.73(15)	H(6WA)-O(6W)-H(6WB)	108(3)
O(5)-Fe(1)-O(1W)	176.54(16)	Fe(2)-O(7W)-H(7WA)	128(3)
O(1)-Fe(1)-O(1W)	91.11(15)	Fe(2)-O(7W)-H(7WB)	130(3)
O(3W)-Fe(1)-O(1W)	88.69(15)	H(7WA)-O(7W)-H(7WB)	101(3)
O(5)-Fe(1)-O(2W)	94.45(16)	Fe(2)-O(8W)-H(8WA)	121(3)
O(1)-Fe(1)-O(2W)	175.59(16)	Fe(2)-O(8W)-H(8WB)	129(3)
O(3W)-Fe(1)-O(2W)	87.14(15)	H(8WA)-O(8W)-H(8WB)	109(3)
O(1W)-Fe(1)-O(2W)	84.59(16)	Fe(2)-O(9W)-H(9WA)	116(4)
O(5)-Fe(1)-O(4W)	92.08(16)	Fe(2)-O(9W)-H(9WB)	130(4)
O(1)-Fe(1)-O(4W)	87.69(14)	H(9WA)-O(9W)-H(9WB)	105(3)
O(3W)-Fe(1)-O(4W)	173.18(16)	H(10A)-O(10W)-H(10B)	106(3)
O(1W)-Fe(1)-O(4W)	84.61(15)	H(11A)-O(11W)-H(11B)	100(3)
O(2W)-Fe(1)-O(4W)	90.94(15)		
O(9)-Fe(2)-O(8W)	86.17(16)		

Table 2.15. Anisotropic displacement parameters ($Å^2 x\ 10^3$) for quenstedtite. The anisotropic displacement parameter exponent takes the form: $-2\pi^2[\ h^2 a^{*2} U^{11} + ... + 2\ h\ k\ a^*\ b^*\ U^{12}\ ]$

	U^{11}	U^{22}	U^{33}	U^{23}	U^{13}	U^{12}
Fe(1)	19(1)	16(1)	13(1)	-1(1)	4(1)	-3(1)
Fe(2)	16(1)	19(1)	15(1)	-2(1)	3(1)	-4(1)
S(1)	23(1)	15(1)	13(1)	-2(1)	5(1)	-4(1)
O(1)	32(2)	15(2)	22(2)	-1(2)	15(2)	0(2)
O(2)	34(2)	24(2)	12(2)	-3(2)	4(2)	-10(2)
O(3)	10(2)	30(2)	25(2)	-4(2)	3(2)	-9(2)
O(4)	29(2)	15(2)	17(2)	0(2)	8(2)	4(2)
S(2)	11(1)	18(1)	15(1)	-1(1)	3(1)	-1(1)
O(5)	31(2)	30(2)	12(2)	-1(2)	-1(2)	4(2)
O(6)	40(2)	17(2)	26(3)	-4(2)	16(2)	-10(2)
O(7)	23(2)	20(2)	21(2)	-3(2)	7(2)	0(2)
O(8)	30(2)	25(2)	14(2)	-10(2)	7(2)	-9(2)
S(3)	19(1)	18(1)	13(1)	-1(1)	4(1)	-4(1)
O(9)	7(2)	40(2)	24(2)	-5(2)	-3(2)	-9(2)
O(10)	9(2)	26(2)	24(2)	7(2)	1(2)	3(2)
O(11)	29(2)	23(2)	21(2)	-2(2)	11(2)	-11(2)
O(12)	43(3)	19(2)	21(2)	-1(2)	15(2)	-1(2)
O(1W)	30(2)	23(2)	12(2)	3(2)	3(2)	-11(2)
O(2W)	38(2)	20(2)	16(2)	1(2)	12(2)	2(2)
O(3W)	7(1)	23(1)	27(2)	-6(1)	6(1)	-2(1)
O(4W)	7(1)	23(1)	27(2)	-6(1)	6(1)	-2(1)
O(5W)	15(1)	31(2)	24(2)	7(1)	8(1)	5(1)
O(6W)	23(2)	21(2)	14(2)	-7(2)	5(2)	-1(2)
O(7W)	15(1)	31(2)	24(2)	7(1)	8(1)	5(1)
O(8W)	25(2)	28(2)	14(2)	2(2)	-2(2)	-13(2)
O(9W)	49(3)	21(2)	17(2)	-8(2)	13(2)	-18(2)
O(10W)	26(2)	40(2)	50(3)	-25(2)	20(2)	-14(2)
O(11W)	34(3)	34(2)	36(3)	1(2)	6(2)	2(2)

Table 2.16. Hydrogen coordinates (x 10^4) and isotropic displacement parameters ($Å^2$x 10^3) for quenstedtite.

	x	y	z	U(eq)
H(1WA)	-1190(70)	1554(17)	-1380(70)	26
H(1WB)	-2510(40)	1220(20)	-690(80)	26
H(2WA)	1980(90)	380(20)	670(40)	29
H(2WB)	2370(80)	152(16)	2620(60)	29
H(3WA)	-3290(60)	829(17)	3610(80)	22
H(3WB)	-2150(70)	431(11)	2860(80)	22
H(4WA)	3750(60)	1701(19)	2460(60)	22
H(4WB)	3460(70)	1424(18)	830(60)	22
H(5WA)	2830(70)	4572(14)	7680(70)	29
H(5WB)	2460(70)	4218(19)	9160(70)	29
H(6WA)	5620(70)	3404(15)	4960(80)	23
H(6WB)	3710(30)	3711(19)	5010(80)	23
H(7WA)	10180(60)	3249(18)	8710(50)	29
H(7WB)	10000(70)	3570(20)	6990(60)	29
H(8WA)	4630(70)	2970(20)	8860(60)	27
H(8WB)	5850(80)	2990(20)	10740(40)	27
H(9WA)	7490(90)	4610(20)	6000(50)	32
H(9WB)	7580(90)	4879(17)	7690(70)	32
H(10A)	4080(70)	2290(19)	6650(100)	42
H(10B)	2060(50)	2370(20)	7010(100)	42
H(11A)	1440(100)	2507(9)	1500(80)	43
H(11B)	1180(100)	2959(18)	2540(40)	43

Table 2.17. Hydrogen bonds for quenstedtite [Å and °].

D-H...A	d(D-H)	d(H...A)	d(D...A)	<(DHA)
O(1W)-H(1WA)...O(2)#1	0.804(19)	1.888(19)	2.692(5)	177(5)
O(1W)-H(1WB)...O(8)#2	0.821(19)	1.86(2)	2.679(5)	172(5)
O(2W)-H(2WA)...O(6)#1	0.816(19)	1.88(2)	2.695(5)	178(6)
O(2W)-H(2WB)...O(7)#3	0.817(19)	1.92(3)	2.709(5)	162(5)
O(3W)-H(3WA)...O(7)#4	0.811(19)	2.07(4)	2.718(5)	136(5)
O(3W)-H(3WB)...O(6)#5	0.837(19)	1.85(2)	2.675(5)	169(5)
O(4W)-H(4WA)...O(3)#6	0.850(19)	1.80(2)	2.639(5)	170(5)
O(4W)-H(4WB)...O(8)#1	0.844(19)	1.81(2)	2.638(5)	164(5)
O(5W)-H(5WA)...O(12)#7	0.836(19)	1.84(2)	2.665(5)	169(5)
O(5W)-H(5WB)...O(11)#4	0.828(19)	1.95(3)	2.700(5)	150(5)
O(6W)-H(6WA)...O(4)#6	0.806(19)	1.88(2)	2.685(5)	176(6)
O(6W)-H(6WB)...O(10)#2	0.832(19)	1.88(2)	2.708(5)	177(6)
O(7W)-H(7WA)...O(11W)#8	0.822(19)	1.84(2)	2.598(6)	153(4)
O(7W)-H(7WB)...O(10)#1	0.850(19)	1.92(2)	2.728(5)	158(5)
O(8W)-H(8WA)...O(10W)	0.811(19)	1.80(2)	2.584(5)	164(6)
O(8W)-H(8WB)...O(4)#8	0.811(19)	1.92(2)	2.721(5)	168(5)
O(9W)-H(9WA)...O(12)#1	0.826(19)	1.80(2)	2.620(5)	173(6)
O(9W)-H(9WB)...O(11)#9	0.819(19)	1.98(2)	2.787(5)	169(5)
O(10W)-H(10A)...O(3)#6	0.812(19)	2.06(3)	2.844(5)	162(6)
O(10W)-H(10B)...O(2)	0.825(19)	1.93(2)	2.749(5)	169(5)
O(11W)-H(11A)...O(4W)	0.851(19)	2.18(3)	2.989(5)	159(5)
O(11W)-H(11A)...O(1)	0.851(19)	2.48(5)	3.084(5)	128(4)
O(11W)-H(11B)...O(10)#2	0.863(18)	2.32(3)	3.028(6)	139(4)

Symmetry transformations used to generate equivalent atoms:

#1 x,y,z-1 #2 x-1,y,z-1 #3 -x+1,-y,-z+1 #4 x-1,y,z

#5 -x,-y,-z+1 #6 x+1,y,z #7 -x+1,-y+1,-z+2

#8 x+1,y,z+1 #9 -x+2,-y+1,-z+2

2.2.7 Bond Valence Summation Quenstedtite

A bond valence analysis was performed using bond length data from the crystal structure of quenstedtite determined here. This analysis was also done using the program VaList V.4.0.7. ©1998-2010. In Table 2.18 are the bond valence summations to the cations of the structure which agree with the assumed valence states.

The bond lengths of the cation-anion pairs of the quenstedtite polyhedra are in good agreement with those reported for other ferric sulfates (Robinson and Fang, 1970; Ackerman et al., 2009), as well as with those reported by Thomas et al. (1974). These numbers can be seen in Table 2.19. Table 2.20 shows the bonds as reported by In italics are the equivalent-bond names from this study Thomas et al. (1974) in comparison with those of this study.

.

Table 2.18: Bond valence summation for the cations found in the mineral quenstedtite.

Atom	Valence State Assumed	Bond Valence Summation	% deviation from assumed valence state
Fe1	Fe1(3)	3.148	5
Fe2	Fe2(3)	3.192	6
S1	S1(6)	5.986	0
S2	S2(6)	6.110	2
S3	S3(6)	6.097	2

Table 2.19: Bond lengths of the cation-anion pairs found in quenstedtite.

Bond	Length	Oxidation State	Ro	B	S
Fe1_O5	1.933	Fe(3)	1.751	0.37	0.611
Fe1_O1	1.961	Fe(3)	1.751	0.37	0.567
Fe1_O3W[O]	1.989	Fe(3)	1.751	0.37	0.526
Fe1_O1W[O]	2.018	Fe(3)	1.751	0.37	0.486
Fe1_O2W[O]	2.021	Fe(3)	1.751	0.37	0.482
Fe1_O4W[O]	2.026	Fe(3)	1.751	0.37	0.476
					Sum = 3.148
Fe2_O9	1.931	Fe(3)	1.751	0.37	0.615
Fe2_O8W[O]	1.969	Fe(3)	1.751	0.37	0.555
Fe2_O7W[O]	1.976	Fe(3)	1.751	0.37	0.544
Fe2_O5W[O]	2.006	Fe(3)	1.751	0.37	0.502
Fe2_O6W[O]	2.011	Fe(3)	1.751	0.37	0.495
Fe2_O9W[O]	2.022	Fe(3)	1.751	0.37	0.481
					Sum = 3.192
S1_O4	1.461	S(6)	1.624	0.37	1.554
S1_O2	1.463	S(6)	1.624	0.37	1.545
S1_O3	1.472	S(6)	1.624	0.37	1.508
S1_O1	1.505	S(6)	1.624	0.37	1.379
					Sum = 5.986
S2_O7	1.449	S(6)	1.624	0.37	1.605
S2_O8	1.465	S(6)	1.624	0.37	1.537
S2_O6	1.47	S(6)	1.624	0.37	1.516
S2_O5	1.486	S(6)	1.624	0.37	1.452
					Sum = 6.11
S3_O11	1.456	S(6)	1.624	0.37	1.575
S3_O10	1.463	S(6)	1.624	0.37	1.545
S3_O12	1.467	S(6)	1.624	0.37	1.529
S3_O9	1.487	S(6)	1.624	0.37	1.448
					Sum = 6.097

Table 2.20: Cation-anion bond lengths of the polyhedra of quenstedtite determined here, compared with Thomas et al. (1974)

Bond Thomas et al. (1974) *(This study)*	Thomas et al.	This Study	Bond Thomas et al. (1974) *(This study)*	Thomas et al.	This Study
Fe1_O12 *(Fe2_O9)*	1.92	1.931(4)	Fe2_O8 *(Fe1_O5)*	1.92	1.933(4)
Fe1_O1W *(Fe2_O8W)*	1.98	1.969(3)	Fe2_O4 *(Fe1_O1)*	1.96	1.961(3)
Fe1_O3W *(Fe2_O7W)*	2.01	1.976(3)	Fe2_O6W *(Fe1_O3W)*	1.99	1.989(3)
Fe1_O4W *(Fe2_O5W)*	2.01	2.006(3)	Fe2_O7W *(Fe1_O1W)*	2.02	2.018(4)
Fe1_O5W *(Fe2_O6W)*	2.01	2.011(4)	Fe2_O8W *(Fe1_O2W)*	2.03	2.021(3)
Fe1_O5W *(Fe2_OW)*	2.03	2.022(3)	Fe2_O9W *(Fe1_O4W)*	2.05	2.026(3)
Mean =	*1.99*	*1.99*	*Mean=*	*2.00*	*1.99*
S1_O1 *(S1_O4)*	1.43	1.461(3)	S3_O9 *(S3_O11)*	1.44	1.456(4)
S1_O2 *(S1_O3)*	1.45	1.463(4)	S3_O10 *(S3_O10)*	1.45	1.463(3)
S1_O3 *(S1_O2)*	1.48	1.472(3)	S3_O11 *(S3_O12)*	1.45	1.467(4)
S1_O4 *(S1_O1)*	1.5	1.505(4)	S3_O12 *(S3_O9)*	1.47	1.487(4)
Mean=	*1.47*	*1.48*	*Mean=*	*1.45*	*1.47*
S2_O5 *(S2_O7)*	1.42	1.449(4)			
S2_O6 *(S2_O8)*	1.42	1.465(4)			
S2_O7 *(S2_O6)*	1.43	1.470(3)			
S2_O8 *(S2_O5)*	1.49	1.486(4)			
Mean=	*1.44*	*1.47*			

2.3 Hydrogen Bonding Introduction

One of the mechanisms relating to bond valence, and subsequently bond strength, is the hydrogen bonding of crystals. Both quenstedtite and romerite have clusters of tetrahedra and octahedra, all of which are bonded together through hydrogen bonding. Quenstedtite also has two free water molecules, one of which is likely zeolitic (Fanfani et al., 1970). To determine how strongly these bonds are holding the clusters and/or water molecules in place one must look predominantly to the hydrogen bond lengths in conjunction with the angles formed (Brown, 1976).

A hydrogen bond in hydrous iron sulfates consists of an O-H···O group. The oxygen in the O-H portion represents the hydrogen donor; whereas the oxygen in the H···O portion is the acceptor. Of the two, it is the donor bond which is the stronger of the two bonds as it, by definition, is a shorter distance

between the oxygen and the hydrogen atom. It is the acceptor bond distance which dictates the overall strength of the entire hydrogen bond. However, there are several factors which contribute to the strength of a hydrogen bond. Brown (1976) outlines these factors as follows: O-O distances between 2.4Å and 2.73Å represent strong hydrogen bonds, whereas O-O distances between 2.74Å and 3.1Å are weak hydrogen bonds. O-O distances greater than 3.1Å are not considered likely hydrogen bonds. As well, strong hydrogen bonds will have O-H···O angles closer to 180°, whereas weaker bonds have O-H···O angles in a lower range and down to a minimum of 130°.

To demonstrate the hydrogen bond strength of particular atomic structures, Brown (1976) organized the data points graphically, plotting the weaker acceptor bond (H···O) in relations to the bond angle. The result was a graph visually demonstrating the distribution of hydrogen bonds as a function of distance and angles in a variety of atomic structures. This graphical means was recreated here using the results of the present study of romerite and quenstedtite and includes the data of Brown (1976).

2.3.1 Hydrogen Bonding of Romerite and Quenstedtite Introduction

An analysis of the hydrogen bonds of romerite (Table 2.7) and quenstedtite (Table 2.13) shows that the majority of the hydrogen bonds in these structures satisfy the requirements set forth by Brown (1976) as indications of strong hydrogen bonds. Figure 2.9 shows strong hydrogen bonds are clustered in the region of H…O distances around 1.73Å. However, there are several bonds in each structure represented on Figure 2.9 that lie outside the main cluster of data points. These bonds classify as weak hydrogen bonds and are listed in Table 2.21.

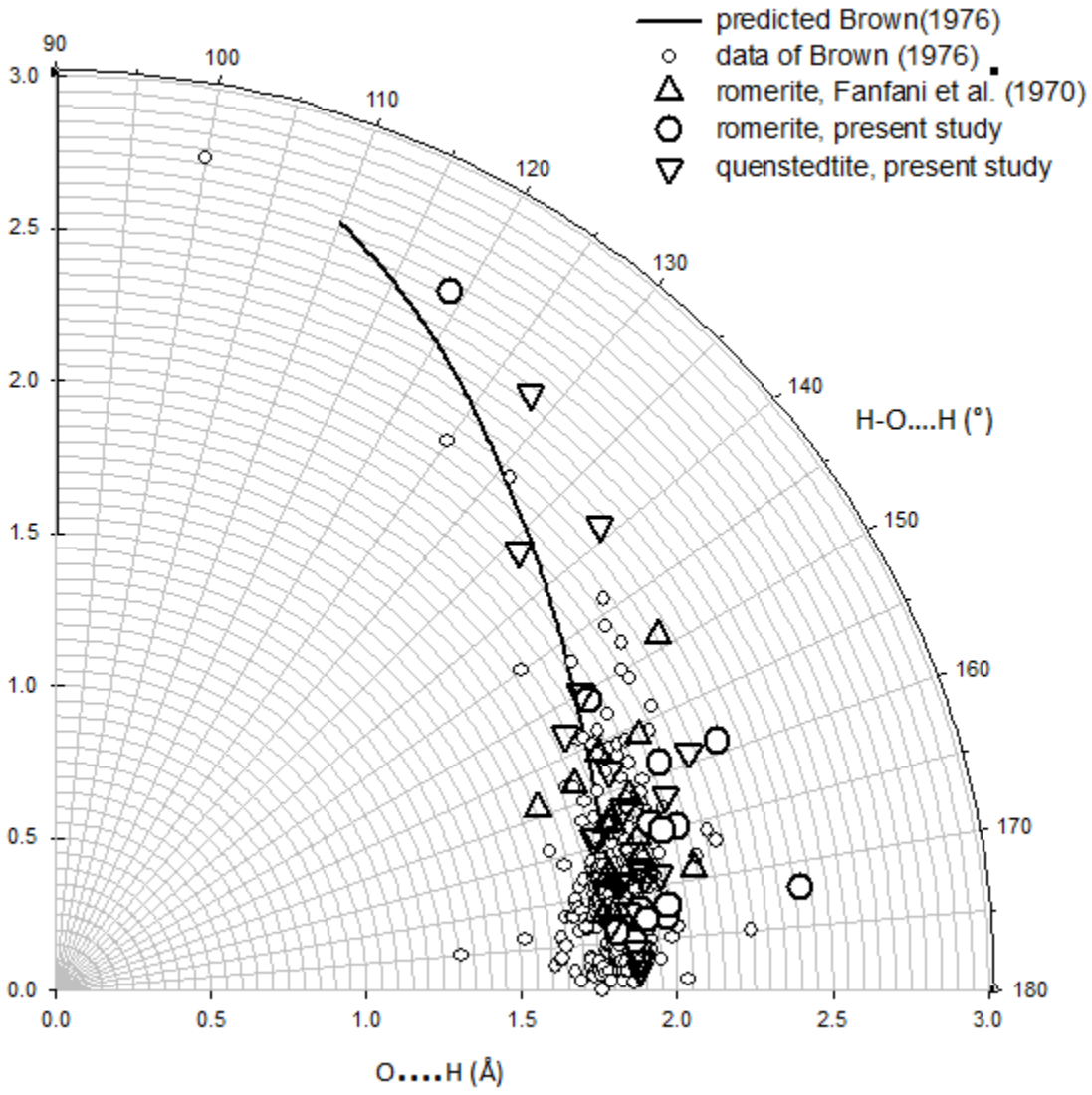

Figure 2.9: O...H acceptor bond lengths plotted against O-H...O angels. Those data points forming a cluster indicate strong hydrogen bonds. Those data points lying outside the cluster suggest weak hydrogen bonds and/or bifurcated bonds.

Table 2.21: The hydrogen bonds in romerite and quenstedtite which classify as weak hydrogen bonds according to Brown (1976).

Romerite (Fanfani et al., 1970)			Romerite (present study)		
O-H···O	d (O-O)	< OHO	O-H···O	d (O-O)	< OHO
O(2W)-H(3)…O(4)	2.82	156	O(1W)-H(2A)…O(4)	3.182(3)	172(8)
O(2W)-H(4)…O(3)	2.99	149	O(2W)-H(3)…O(4)	2.799(2)	159(2)
O(3W)-H(5)…O(3)	2.74	165	O(2W)-H(4)…O(3)	3.002(2)	159(2)
O(3W)-H(6)…O(2)	2.84	169	O(3W)-H(6)…O(2)	2.828(2)	165(3)
O(5W)-H(10)…O(8)	2.74	167	O(7W)-H(14)…O(2)	3.098(2)	119(2)
Quenstedtite (present study)					
O(9W)-H(9WB)…O(11)	2.787(5)	169(5)			
O(10W)-H(10A)…O(3)	2.844(5)	162(6)			
O(10W)-H(10B)…O(2)	2.749(5)	169(5)			
O(11W)-H(11A)…O(4W)	2.989(5)	159(5)			
O(11W)-H(11A)…O(1)	3.084(5)	128(4)			
O(11W)-H(11B)…O(10)	3.028(6)	139(4)			

2.3.1.1 Hydrogen Bonding of Romerite

The hydrogen bonds of romerite identified by Fanfani et al. (1970) are the same as that identified for the crystal analyzed for this study except for a few minor differences. One of the bonds, [O(1W)-H(2A)…O(4)], did not have the bond angle or any bond length listed by Fanfani et al. (1970) except for that of the H...O bond. This bond was measured as part of this study and the missing bond lengths and angles are listed. This bond is also listed in Table 2.21 as a weak bond. A closer look at this bond shows it to be bifurcated (Figure 2.10), meaning that one hydrogen is taking part in two hydrogen

bonds. This bifurcated nature of a bond decreases the strength and suggests both bonds involving the one hydrogen atom are very weak.

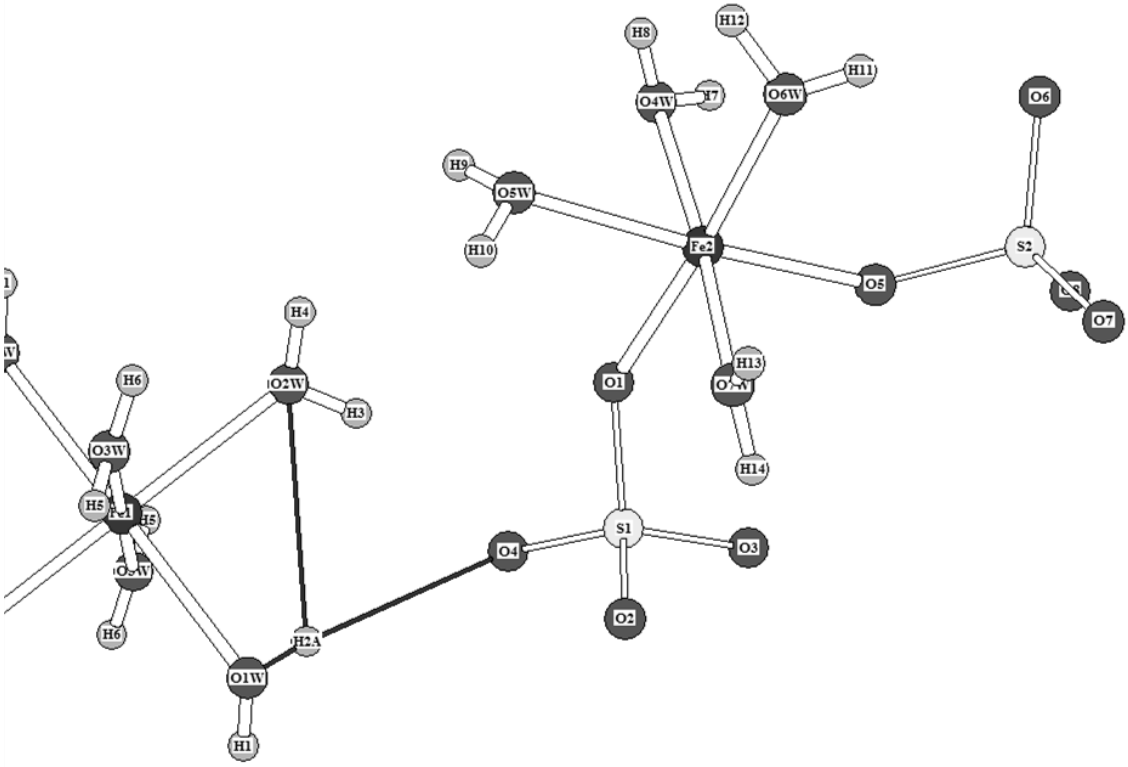

Figure 2.10: The bifurcated bond involving the H2A atom in romerite. Bifurcated hydrogen bonds indicated by dark, thin, lines.

Another difference between the Fanfani et al. (1970) bonding scheme and that identified in this study is that the Fanfani et al. (1970) paper did not list [O(7W)-H(14)...O(2)]. The O(7W) atom involved in this bond is also involved in three other hydrogen bonds, both of which form a bifurcated arrangement (Figure 2.11). The angle of the [O(7W)-H(14)...O(2)] bond is very small, at only 119°. This suggests that this bond is very weak. Anderson et al. (2012) suggested that a low O-H…O angle may indicate a bifurcated hydrogen bond, as seen in Figure 2.11. The other bond involving the H(14) atom in this bifurcated bond is slightly longer (stronger) but still would classify as weak.

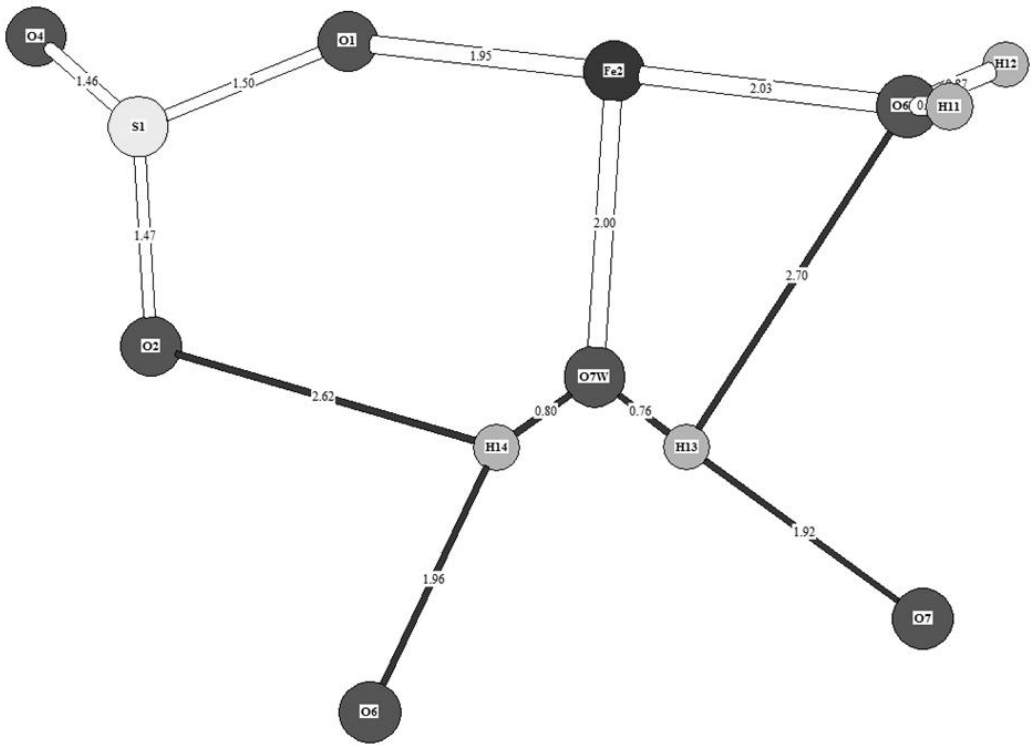

Figure 2.11: The bifurcated hydrogen bonds involving H13 and H14 in romerite. The O7W atom both these bifurcated bonds, the H14 bond involving a weak bond connected to O2 and a stronger one connected to O6. These weak bifurcated bonds connect the Fe1 and the Fe2 octahedra, suggesting that this is one of the less stable layers in the romerite structure.

While all the other hydrogen bonds listed in Fanfani et al. (1970) and this study are similar, there are several minor differences in bond lengths, which results in some of the outlying bonds of the Fanfani et al. (1970) description no longer being outliers (or weak bonds) in the present study. These bonds are the [O(3W)-H(5)…O(3)] bond and the [O(5W)-H(10)…O(8)] bond.

Four of the five weak hydrogen bonds of romerite identified in this study involve the Fe1 octahedron connecting to the Fe2 cluster. This suggests that the bonding between the layers of the Fe1 octahedra and the Fe2 ferric iron octahedra represent the one of the weakest connections between layers in the romerite crystal structure.

The rest of the bonds in the romerite structure all classify as strong and are represented among the cluster of points on Figure 2.9 and can be seen listed in Table 2.7.

2.3.1.2 Hydrogen Bonding of Quenstedtite

In the quenstedtite atomic structure, there are six hydrogen bonds that are identified as weak. No hydrogen bonds were discussed in the Thomas et al. (1974) structure solution so no comparisons can be made. However, five of the six weak hydrogen bonds in the quenstedtite involve either O(10W) or O(11W), those being the two free water molecules. This suggests that, while the other elements in the quenstedtite structure are held together with strong hydrogen bonds, the free water molecules represent the weakest aspect of the structure. That these water molecules are found between the AA…BB layers indicates that the strength of the structure is found within the strong-hydrogen-bonded AA or BB layers, whereas the weakest point is between these A and B layers, where the free water molecules are found. The only other bonds connecting these AA and BB layers are found to originate from the S1 tetrahedra (part of the Fe1 octahedral group), which connects with two of the OW atoms from the Fe2 octahedra group (Figure 2.12).

Similar to romerite, one of the weak bonds in quenstedtite, that of the O(11W)-H(11A)…O(1) bond has an angle of less than 130° (being 128°). This small angle suggests a bifurcated hydrogen bond (Anderson et al., 2012). When looking at Figure 2.13, we can see the hydrogen bonds associated with the free water molecule, O(11W). It is clear from this diagram that there are two bonds associated with the H(11A) atom, making this a bifurcated bond. Regarding the O(11W) atoms, there are three weak hydrogen bonds holding this, likely zeolitic, water molecule in place. However, there is also a fourth hydrogen bond, a strong bond, connecting the O(11W) molecule to the O(7W) of the Fe2 octahedron.

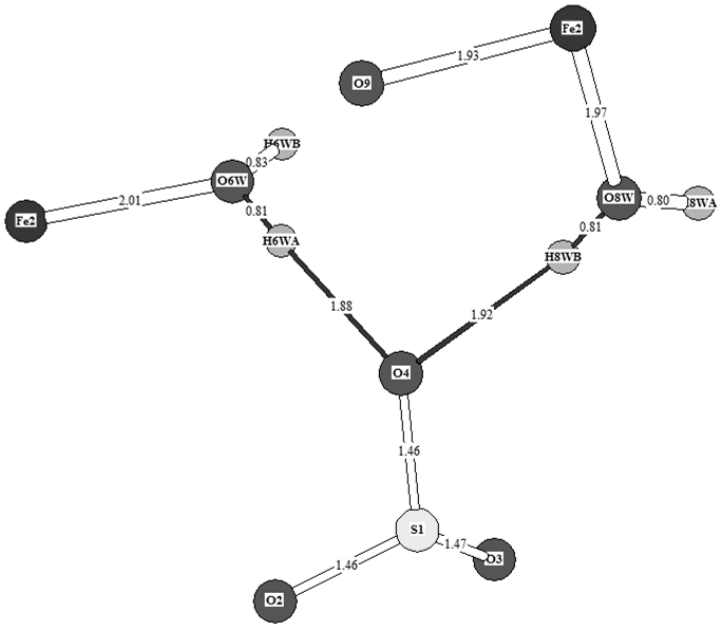

Figure 2.12: The only two strong hydrogen bonds connecting the A and B layers in quenstedtite. Both have the O4 atom in the S1 tetrahedra acting as the acceptor oxygen.

The other free water molecule in quenstedtite, O(10W), is likewise held in place with hydrogen bonds. However, O(10W) has only two weak hydrogen bonds associated with it and neither are bifurcated. They are still weak bonds, but they are not as weak as those holding in place O(11W). As well, there is a third hydrogen bond holding in place O(10W) and this bond is a strong one. Based on hydrogen bond lengths O(10W)it is less tightly bonded in comparison to O(11W). This fact may suggest that, while O(11W) may be zeolitic, it is unlikely that O(10W) is as well. However, O10W and O11W have similar isotropic displacement parameters indicating similar atomic bond constraints for both water molecules. The bonds holding in place O(10W) can be seen outlined in Figure 2.13.

The rest of the hydrogen bonds in quenstedtite are stronger bonds and can be seen as part of the cluster of points on Figure 2.9 and listed in Table 2.13.

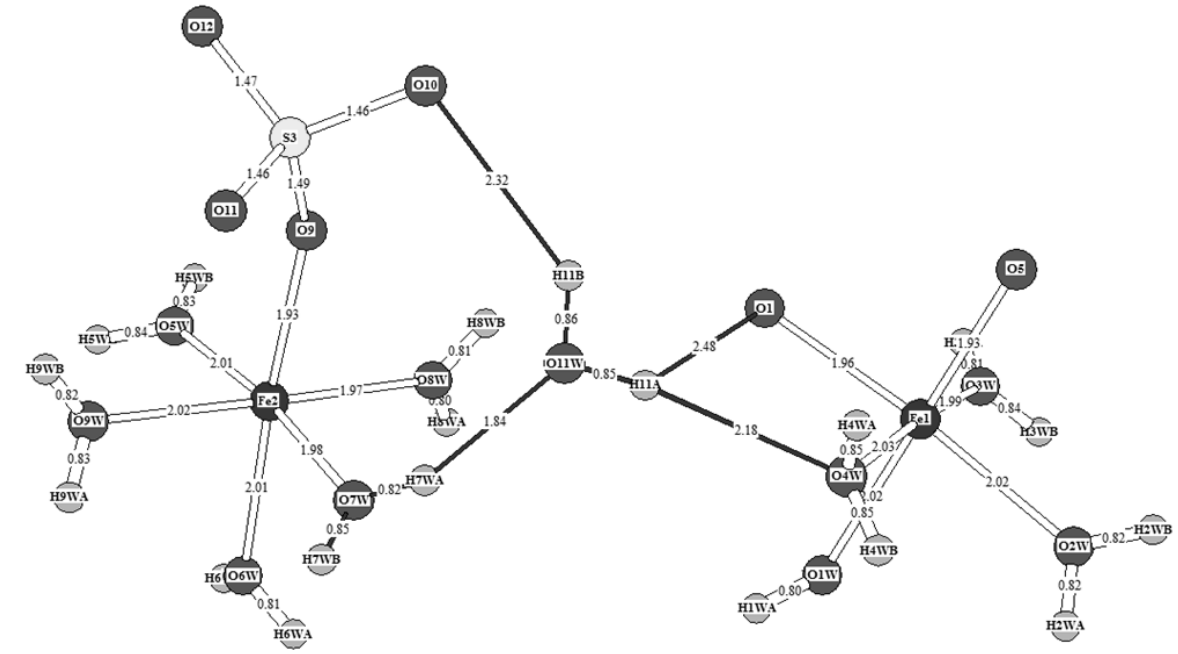

Figure 2.13: the hydrogen bonds in quenstedtite holding the zeolitic water molecule, O11W in place. One of the bonds is bifurcated. Hydrogen bonds are indicated by dark, thin, lines.

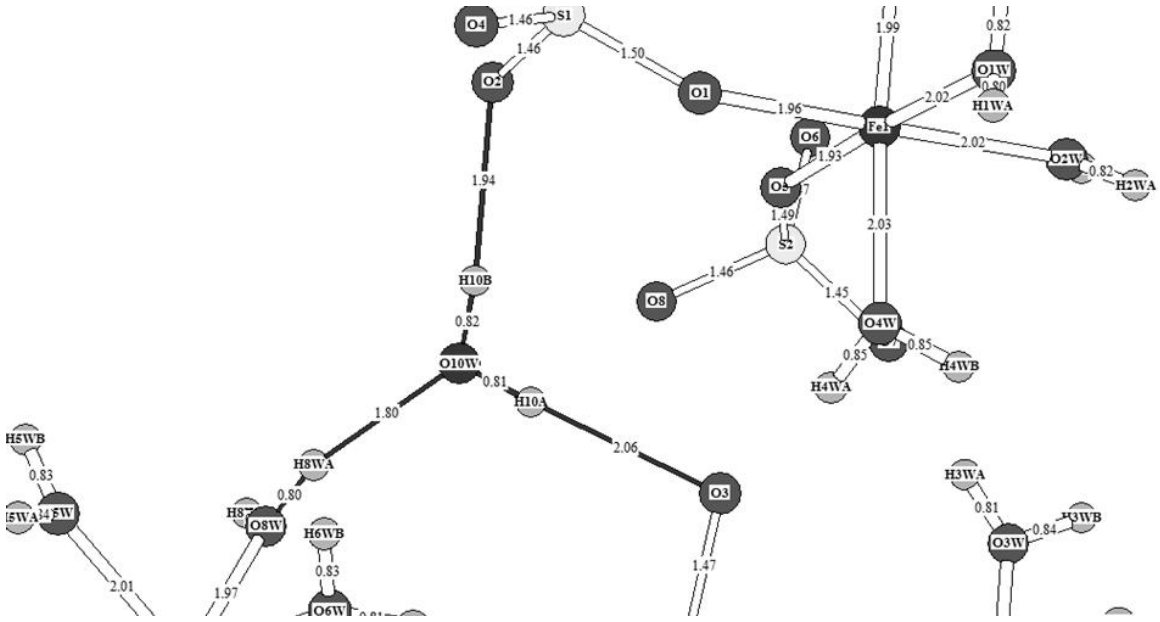

Figure 2.14: The hydrogen bonds holding the O10W molecule in place. Two bonds classify as weak bonds, and one as a strong bond. Neither weak bond is bifurcated, suggesting that the O10W water molecule held more tightly in the quenstedtite structure than O11W.

2.4 The Transition between Romerite and Quenstedtite

The transition between romerite and quenstedtite involves the oxidation of the ferrous iron located in romerite. In both structure the Fe^{2+} atom is coordinated with 6 water molecules and occurs as an isolated octahedron connected only through hydrogen bonding to the rest of the structure.

The process of ferrous iron oxidation typically takes place in the presence of dissolved oxygen (Stumm and Lee, 1961). This process can follow, for example, that which is outlined in Figure 2.15. In this oxidation example the result of the oxidation of ferrous iron is the production of ferric iron ion and a water molecule.

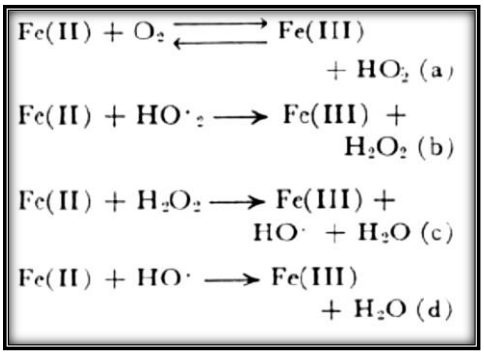

Figure 2.15: Oxygenation of ferrous iron (from Stumm and Lee, 1961)

In the case of the romerite-quenstedtite transition, the ferrous iron of the Fe1 octahedra in romerite becomes oxidized, leaving a more highly charged cation to be balanced. This causes a shuffling of the anions involved, with one of the sulfate groups from the Fe2 octahedra in romerite to be removed and added to the newly oxidized ferric iron. This process of the ferrous iron octahedron being oxidized and combined with one of the ferric iron octahedra of the romerite structure can be visualized as following the following equation:

Romerite $[Fe^{2+}(H_2O)_6 + Fe^{3+}(SO_4)_2(H_2O)_4]$ – e- → Quenstedtite $[Fe^{3+}(SO_4)(H_2O)_5 + Fe^{3+}(SO_4)(H_2O)_5]$

This process results in the ferrous iron octahedron of romerite combining with one of the $Fe^{3+}(SO_4)_2(H_2O)_4$ clusters to create two $Fe^{3+}(SO_4)(H_2O)_5$ octahedra, such as those that we find included in the quenstedtite structure. Following the formula outlined in Figure 2.15, we can see that the oxidation process of ferrous iron to ferric iron through the addition of dissolved oxygen (in water) also results in the formation of a water molecule. With this interaction we can see a hypothesis of where the free water molecules also found in quenstedtite could originate (however, the water molecules could also simply originate from the humidity in the air).

With the rearranging of sulfate groups following the oxidation of the ferrous iron in romerite, comes a change in the hydrogen bonding holding the structure together. The weakest bonds remain consistently between the layers of unlike octahedral-tetrahedral groups. In romerite, the weakest point, as inferred through the hydrogen bonds, is between the Fe1 layers and the Fe2 layers. Likewise, in quenstedtite, the weakest point is between the Fe1 layers and the Fe2 layers. This consistency in the weak points of the structure is expected as the alteration from romerite to quenstedtite involves the ferrous iron Fe1 atom in romerite to oxidize to the Fe1 ferric iron atom in quenstedtite

The two $Fe(SO_4)_2(H_2O)_4$ groups remain in a similar orientation in quenstedtite as they do in romerite. In romerite they are located running along the c axis in a *cis* configuration. In quenstedtite they are found as the AA units in the …AABBAA… ordering. The ferrous iron containing octahedron of romerite, having been split into two $Fe(SO_4)(H_2O)_5$ octahedral groups through the oxidation of the Fe^{2+} ion and the addition of dissolved oxygen, is found as the BB units in the quenstedtite structure. As described in the section 2.2.5, these …AABB… groups are separated by two water molecules not directly bound to any polyhedron.

Of course, looking at systems such as that shown in Figure 1.1, it is clear that the description provided here is a simplified version of what is likely actually happening on the atomic level in relation

to these two minerals and the transition of romerite to quenstedtite. However, this simplified analysis does make the visualization of what is a much more complex process possible and can help us to understand the mineral transitions of this system.

Chapter 3

An Investigation into the Ferric Sulfate Hexahydrate

3.1 Introduction

Posnjak and Merwin (1922) studied the Fe_2O_3-SO_3-H_2O system in a series of experiments using mixtures in sealed glass vials at temperatures from 50°C to 140°C, where they created synthetic analogues of the mineral species in this chemical system (Figures 3.1 and 3.2). One of the phases Posnjak and Merwin synthesized had not been observed previously and had no known analogue in nature. The phase was the only normal hydrous ferric sulfate found to form at 110°C and above. Through gravimetric analysis they determined this phase to have the composition $Fe_2(SO_4)_3 \cdot 6H_2O$. Optical measurements were made to determine its crystallographic properties (Posnjak and Merwin, 1922) and the hexahydrate was described as forming monoclinic laths elongated parallel to the *c* axis. A maximum extinction angle of 26° was noted and the refractive indices were observed to be α=1.605 β=1.635 and γ=1.657. Figures 3.1 and 3.2 (Posnjak and Merwin, 1922) show that at 110° C and 140°C there was a large stability field for the hexahydrate (presented as $Fe_2O_3 \cdot 3SO_3 \cdot 6H_2O$).

The mineral formulas used by Posnjak and Merwin (1922) reflect the components expressed as oxides. Expressed in today's system of mineralogy the formulas represent those indicated in Table 3.1.

Table 3.1: Posnjak and Merwin (1922) formulas described using today's formulaic methods. Two of the Posnjak and Merwin materials have no known equivalent substance.

Posnjak and Merwin (1922)	Present Day Formula	Mineral
$Fe_2O_3 \cdot H_2O$	$FeO(OH)$	Limonite/Goethite
$3Fe_2O_3 \cdot 4SO_3 \cdot 9H_2O$	$(H_3O)Fe_3(SO_4)_2(OH)_6$	Hydronium Jarosite
$Fe_2O_3 \cdot 2SO_3 \cdot H_2O$	$Fe_2(SO_4)_2(OH)_2$	No known analogue
$Fe_2O_3 \cdot 3SO_3 \cdot 6H_2O$	$Fe_2(SO_4)_3 \cdot 6H_2O$	Hexahydrate
$Fe_2O_3 \cdot 4SO_3 \cdot 3H_2O$	$H_2Fe_2(SO_4)_4 \cdot 2H_2O$	No known analogue
$Fe_2O_3 \cdot 4SO_3 \cdot 9H_2O$	$HFe(SO_4)_2 \cdot 4(H_2O)$	Rhomboclase

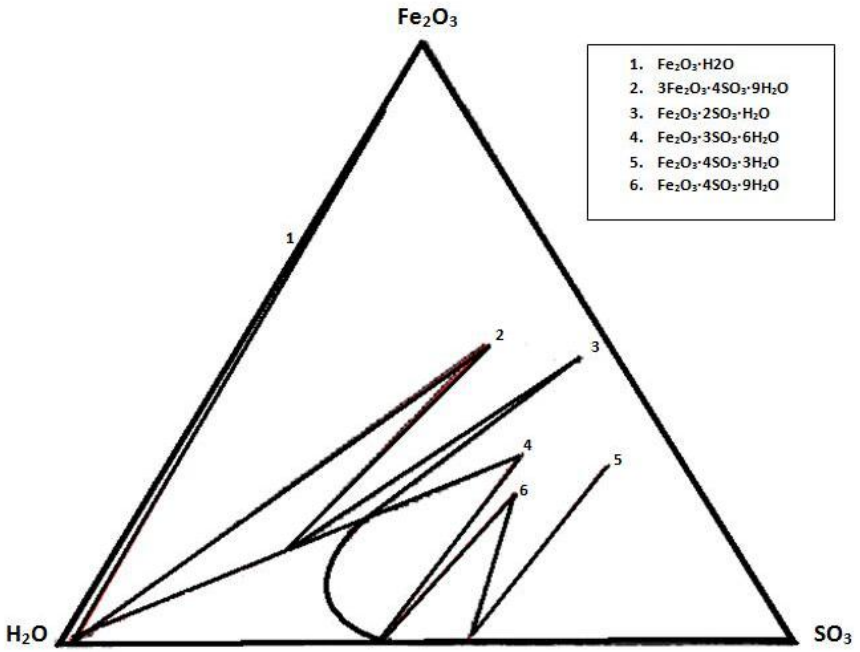

Figure 3.1: Sulfates formed at 110° C in closed systems as a function of H_2O, SO_3 and Fe_2O_3 available (after Posnjak and Merwin, 1922 redrawn).

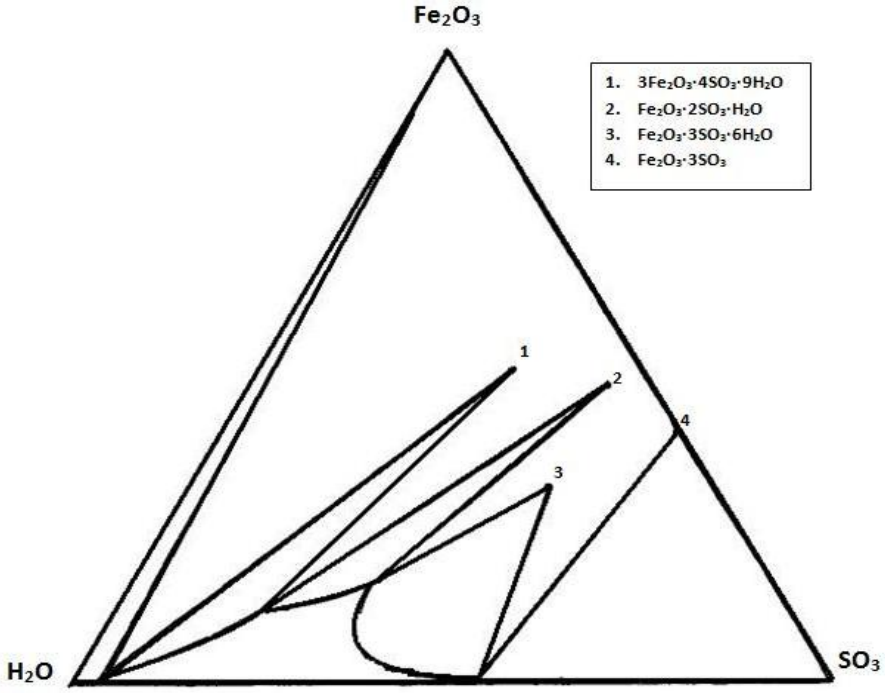

Figure 3.2: Sulfates formed at 140° C in closed systems as a function of H_2O, SO_3 and Fe_2O_3 available (after Posnjak and Merwin, 1922 redrawn)

Lausen (1928) later described a hexahydrate phase that had formed under the extreme conditions of a self-combusted mine fire at the United Verde Copper mine. The minerals copiapite ($Fe^{3+}_{0.66}Fe^{3+}_{4}(SO_4)_6(OH)_2 \cdot 20H_2O$), coquimbite ($Fe_2(SO_4)_3 \cdot 9H_2O$), voltaite ($K_2Fe^{2+}_{5}Fe^{3+}_{3}Al(SO_4)_{12} \cdot 18H_2O$) and several other new sulfate species were also identified. In an effort to control the mine fire, water had been initially used, which likely contributed to the formation of hydrated ferric sulfate phases. One of the phases not previously discovered in nature described by Lausen was determined to have 6 water molecules by gravimetric analysis, and it was suggested by Lausen that this hexahydrate was likely the same material as that which had been identified by Posnjak and Merwin (1922). The hexahydrate crystals were described as forming monoclinic elongated laths with refractive indices of α=1.598 β=1.628 and γ=1.654 and a maximum extinction angle of 27°. This optical data coincided well with the data reported by Posnjak and Merwin (1922). As the fire at the mine was self-combusted, the hexahydrate was considered "natural" and thus the ferric sulfate hexahydrate mineral was recognized. It was named lausenite in honor of its discoverer (Butler, 1928).

Majzlan et al. (2005) obtained the type-specimen of lausenite from the Harvard Mineralogical Museum and re-analyzed the material. They compared its X-ray diffraction pattern to that of synthetic $Fe_2(SO_4)_3 \cdot 5H_2O$. The pentahydrate was synthesized by mixing ferric sulfate, deionized water and reagent-grade sulfuric acid, following the phase diagrams of Posnjak and Merwin (1922). However, unlike Posnjak and Merwin (1922), Majzlan et al. (2005) did not precipitate $Fe_2(SO_4)_3 \cdot 5H_2O$ in a closed system, the solution was instead allowed to slowly evaporate in a beaker at 90°C. The X-ray diffraction patterns of the type specimen of lausenite from the Harvard Mineralogical Museum and that of synthetic $Fe_2(SO_4)_3 \cdot 5H_2O$ were compared, and found to be nearly identical, with the exception of a few minor peaks. Majzlan et al. (2005) suggested that the original conclusions of Lausen (1928) and Posnjak and Merwin (1922) may have been incorrect and that the material they described as $Fe_2(SO_4)_3 \cdot 6H_2O$ was actually $Fe_2(SO_4)_3 \cdot 5H_2O$. The pentahydrate crystal structure was solved using powder diffraction

data and the unit cell was determined to be *a*=10.679Å *b*=11.053Å and *c*=5.567Å with β=98.89°. The space group was found to be $P2_1/m$. Unfortunately, no refractive indices were reported, likely due to the small size of the grains. It is not possible to say with absolute certainty that the type specimen from the museum had not dehydrated during the 85 years of storage but Majzlan et al. (2005) described no visible signs of deterioration on the sample. However, it is possible that the sample had re-equilibrated and had originally been a hexahydrate.

Ling and Wang (2009) synthesized kornelite $Fe_2(SO_4)_3 \cdot 7H_2O$, the $Fe_2(SO_4)_3 \cdot 5H_2O$ identified by Majzlan et al. (2005), rhomboclase ($H_3OFe(SO_4)_2 \cdot 3H_2O$) and a fourth unknown hydrous ferric sulfate. To produce this mixture they placed amorphous ferric sulfate in an atmosphere of relative humidity (RH) approximately 24% and left it for 24 hours at a temperature of 95 °C. They studied this mixture using Raman spectroscopy and powder X-ray diffraction (XRD). The XRD data showed peaks that could not be attributed to a known hydrous ferric sulfate. Unfortunately, the published XRD data is not of suitable quality to determine exact 2θ locations and d-spacings, and the original XRD files had been misplaced (Ling, personal correspondence, 2011), but some idea of the pattern details could be determined from this published document (Figure 3.3). Though the material was a mixture of pentahydrate, rhomboclase, possibly kornelite, and the previously unindexed phase, weight loss analysis was performed and the resulting formula for the new phase was estimated as $Fe_2(SO_4)_3 \cdot 5.75H_2O$. That this weight loss analysis was performed on a mixed-phase powder sheds some doubt on the results obtained, however, Ling and Wang (2009) suggested that Posnjak and Merwin (1922) and Lausen (1928) were correct in their original analyses when they reported on the existence of a ferric sulfate hexahydrate and that the hexahydrate was likely the unindexed phase that they had grown. Ling and Wang (2009) were not able to synthesize material consisting of a single phase of this hydrous ferric sulfate material (personal correspondence, 2011) and the crystallographic details of the phase they grew remained unknown.

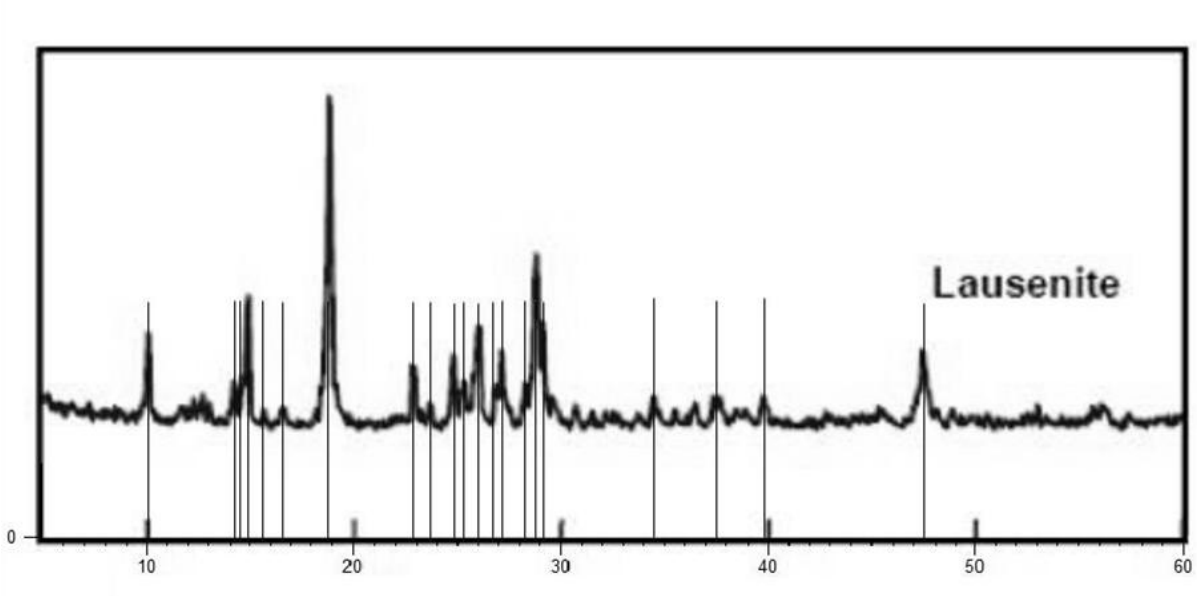

Figure 3.3: Lausenite pattern with peaks indicated (Cu Kα radiation). The quality of this pattern is not sufficient for accurate d-spacing analysis, but an estimation of the d-spacings is given in Table 3.2. Ling and Wang (2009).

Table 3.2: Approximate d-spacings indicated by the Ling and Wang (2009) pattern.

2θ	d-spacing (Å)	2θ	d-spacing (Å)
10.03	8.81182	26.02	3.42171
14.26	6.20603	26.69	3.33731
14.41	6.14177	27.18	3.27825
14.90	5.94087	28.18	3.16415
15.73	5.62922	28.83	3.09427
16.72	5.29807	29.21	3.05488
18.88	4.69653	34.50	2.59761
22.80	3.89714	37.56	2.39271
23.62	3.76367	39.82	2.26197
24.81	3.58578	47.49	1.91299
25.24	3.52566		

As there was evidently some uncertainty regarding the existence of the ferric sulfate hexahydrate and whether or not it would appropriately be given the mineral name of lausenite, it was decided to investigate further the unidentified phase of Ling and Wang as well as the experiments of Posnjak and Merwin (1922).

3.2 Ling and Wang (2009) Experiment Refined

The Ling and Wang (2009) experiments used an amorphous 5-hydrated ferric sulfate material exposed to a controlled humidity atmosphere created using a NaI buffer (RH 23.3%) at 95°C to create what they called lausenite (Ling and Wang, 2009). However, the material that they grew was not a single phase powder (personal correspondence, 2011) and thus the conclusion that they reached was questionable. It was decided to recreate the Ling and Wang (2009) experiment to obtain the same material and subject it to further analysis.

3.2.1 Experimental Method

The reagent, amorphous ferric sulfate pentahydrate (Acros Organics), was in the form of a loose, pale yellow powder. Two grams of this material was placed in a glass beaker above a saturated $MgCl_2$ buffer solution in a 250 ml. sealed container. This created an atmosphere of 23.07% relative humidity at 95°C (Greenspan, 1977), which is similar to that of the saturated sodium iodide (NaI) buffer solution used by Ling and Wang (2009) at 95°C of 23.3%.

After 24 hours at 95°C, the ferric sulfate turned a light brown-yellow colour, had decreased in volume, and had hardened. This resultant material was studied using a Panalytical X'pert Pro™ diffractometer equipped with a copper-target X-ray (Wavelength = 1.5418 Å for Cu Kα) tube operating at 40kV and 45mA. An incident slit of 1/8° with a 1/4° anti-scatter slit and 0.02 rad soller slits were used. A

Ni filter was used, with an X'celerator™ position sensitive detector. Data were collected with an effective step size of 0.017° 2θ and a 100 second counting time. The 2θ range of 5°-75° was measured.

The X-ray diffraction pattern was analyzed using the computer program HIGHSCORE™ (version 2.2; Panalytical, 2008). The pattern did not readily match any of the ferric sulfate patterns present in the International Center for Diffraction database (ICDD) (2006), however, the resulting pattern (Figure 3.4) included many peaks which were close to that of the pattern presented by Ling and Wang (2009) for the unknown mineral they believed to be a ferric sulfate hexahydrate (Figure 3.3, Table 3.2). It was clear that the material also contained a mixture of rhomboclase and pentahydrate. The XRD pattern in Figure 3.4 shows the resulting pattern with the known phases identified. The red peaks are those which are unaccounted for and were presumed to belong to the unknown phase (hereinafter referred to as UK1). A calculated profile was modeled using the Rietveld refinement method based on the atomic parameters for rhomboclase (Mereiter, 1974) and pentahydrate (Majzlan et al., 2005).

A series of experiments were conducted in an effort to obtain a single-phase sample so that the crystallographic details of the unknown material could be determined. Approximately 2 g of amorphous ferric sulfate was exposed to different relative humidities at different temperatures and for varying amounts of time. These experiments are outlined in greater detail below.

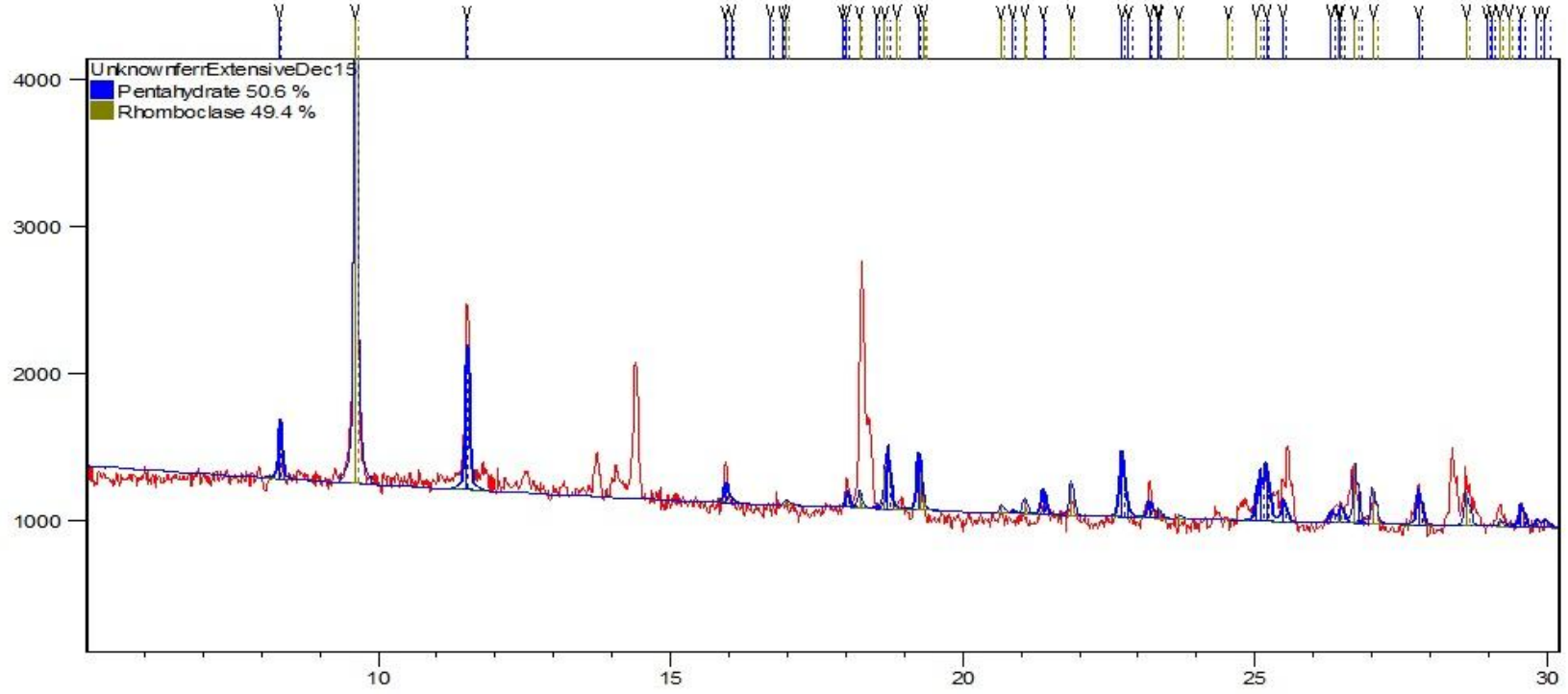

Figure 3.4: X-ray diffraction pattern showing Rietveld refinement created using the atomic structure data of pentahydrate (Majzlan, 2005) and rhomboclase (Mereiter, 1974). the profile cacluated using the contributions from rhomboclase and pentahydrate is blue. intensity not accounted for by this model is seen as the red line.

When a sample with the minimum amount of additional phases was achieved, X-ray diffraction data was collected from a back-packed sample using the Panalytical X'pert Pro™ diffractometer set with a cobalt-target X-ray tube (Fe filtered, wavelength 1.7902 A) operating at 40kV and 45mA. An incident slit of 1/16° with a 1/8° anti-scatter slit and 0.02 rad soller slits were used, with an X'celerator™ position sensitive detector. Data were collected with an effective step size of 0.017° 2θ and an effective counting time of 219 seconds. Measurements were taken between a range of 5°θ and 70°θ. Cobalt Kα radiation was used to reduce fluorescence of this iron sulfate. All X-ray diffraction results were analyzed using the computer program HIGHSCORE™.

3.2.2 Results and Discussion

The XRD patterns exhibiting peaks associated with the unknown mineral phase, UK1, were formed at a temperature between 85°C and 95°C and a RH between 10% and 25%. The only other variable which affected the synthesis of UK1 was that of time. While material consisting of only UK1 was never formed, the least-contaminated mixture grew after being at 90°C over a NaI buffer solution (RH 23.25%) for 33 hours. An estimated abundance of UK1 in this sample, using Rietveld method for identified phases and peak intensities of the unaccounted for peaks, was estimated to be approximately 75%. All samples grown for varying amounts of time contained a mixture of rhomboclase, kornelite or pentahydrate and UK1. There were always at least three phases created with each synthesis. These time-based variable results are summarized in Table 3.3 and Table 3.4.

All samples had become entirely pentahydrate after 35 hours of exposure to either 95°C or 85°C at relative humidities between 23.07% and 23.25%. This was consistent with other reported data regarding the stability field of pentahydrate (Ling and Wang, 2010; Xu, 2011). The samples were placed

in the oven at room temperature and therefore they were subjected to a temperature and relative humidity ramping period at the start of each time period.

Table 3.3: Sulfate formation at 85° C and 22.63% – 25.11% RH. Small sample volume refers to experiments done with approximately 1g of reagent in small ceramic cups. Other experiments began with 2g reagent.

Time (hours)	Product
11	1,4**
15	2,3,4**
15	2,3,4**
24	1,2,4
30	1,2,4
31	1,2,4
32	1,2,4
33	2,3,4
38	3,4
42	3

Legend
1- Kornelite
2- UK1
3- Pentahydrate
4- Rhomboclase
**small sample volume

Table 3.4: Ferric sulfate formation at 95° C and 23.07% RH from reagents amorphous ferric sulfate. the UK1 was never observed to grow as a single-phase powder.

Time (hours)	Product
13	4
16	4
16.5	4
23	2,3,4
23.5	2,3,4
24	2,3,4
25	2,3,4
27	2,3,4
27.5	2,3,4
30	2,3,4
31	2,3,4
33	2,3,4
33.5	2,3,4
35	2,3,4
36	3,4
37	3
44	3

Legend
1- Kornelite
2- UK1
3- Pentahydrate
4- Rhomboclase

The experiments performed here allowed for a large volume of resultant material to be formed and analyzed using back-packed X-ray techniques. This was required for Rietveld analysis of the data. Through a thorough analysis and comparison of the all patterns obtained for the different mineral mixtures, a list of the diffraction peaks due of UK1 could be determined. If a single-phase powder had been produced, the determination of the unit cell for UK1 would be relatively straight forward. However, not being able to generate a single phase sample meant that other methods of classifying this phase were necessary. More information needed to be gathered.

3.3 Stability Study

While it was evident from the experiments outlined above that UK1 formed at temperatures above 85°C, a series of experiments were performed to confirm that UK1 did not appear at temperatures below 60°C (Kong et al., 2011, Figure 3.5a) or below temperatures of 80°C (Ackerman et al., 2009, Figure 3.5b). These experiments used kornelite, pentahydrate and the amorphous ferric sulfate as the reagents. As the hypothesis put forth by Ling and Wang (2009) was that the UK1 was a hexahydrate, it was possible that the phase could be seen to dehydrate from kornelite or rehydrate from pentahydrate.

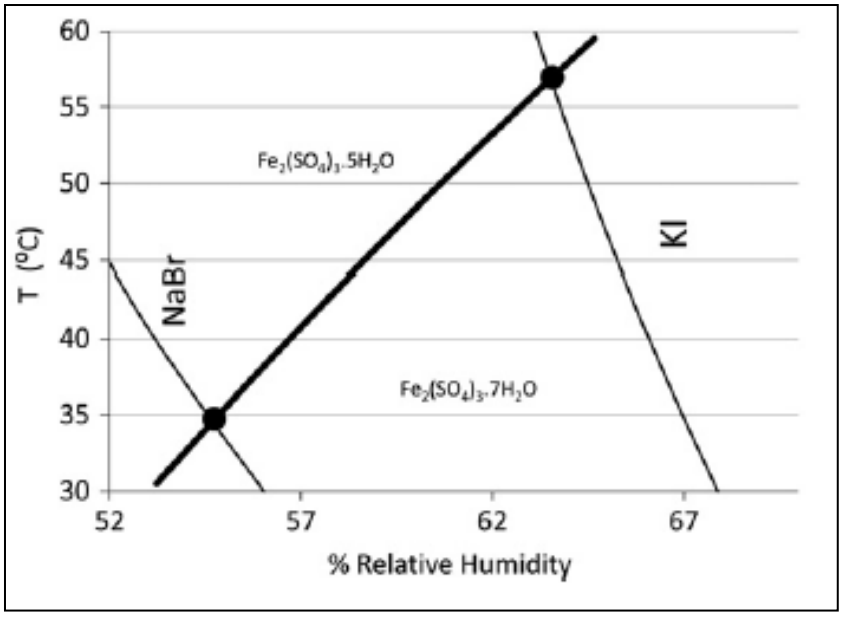

Figure 3.5a: Experimentally determined phase diagram showing the relationship between kornelite and pentahydrate (Kong et al., 2011). The results of this research were consistent with these findings.

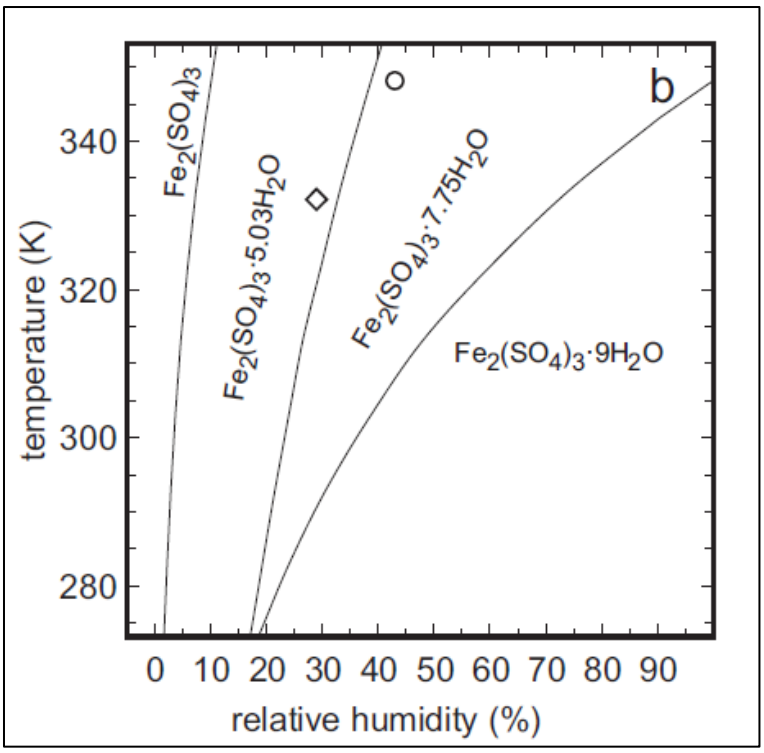

Figure 3.5b: Thermodynamically determined phase diagram, showing Kong data points (circle and square). (Ackerman et al, 2009). The Kong data are consistent with this phase diagram as is the data determined experimentally as part of this research.

3.3.1 Experimental Method

Pentahydrate and kornelite were used as reagents and were synthesized through the hydration of amorphous ferric sulfate. Pentahydrate was formed by exposing amorphous ferric sulfate to an atmosphere created by a $MgCl_2$ buffer solution (RH 24.12%) for a period of 48 hours at a temperature of 90°C (Ling and Wang, 2009). Kornelite was obtained by exposing amorphous ferric sulfate to an atmosphere of 65.03% RH created by a $NaNO_3$ buffer solution at 90°C for 24 hours (Ling and Wang, 2010). XRD analysis of both products confirmed their identity as pentahydrate and kornelite. A suite of buffer solutions (LiCl, KF, $MgCl_2$, NaBr, $MgNO_3$, KI and $NaNO_3$ (Greenspan, 1977) was used to span as much of the range of relative humidities as possible. These solutions were placed in 250 ml, wide-mouthed mason jars. Within each jar, three circular glass XRD sample slides (30mm), each of which having a fine dusting of either pentahydrate, kornelite or amorphous ferric sulfate, were placed on a support above the saturated solution and the jars were sealed. These containers were then placed in a resistance furnace at 30°C for two weeks. The samples were retrieved and analyzed by X-ray diffraction. Analysis occurred after one week in the oven and then the same sample was placed back in the oven and analyzed again after a second week at the same temperature and relative humidity. After each two week period the oven temperature was increased by 10°C and the samples were returned to the oven. This process was continued until a temperature of 80°C was reached. Oven temperatures were confirmed using thermocouple data monitored by Omega data loggers (±3 degrees). For most samples, the slides were prepared for the 30°C run and then used throughout the entire series. However, some samples experienced deliquescence, depending on the temperature, RH, and material and required a new slide to be prepared for the next 10°C increment.

Where the phases were seen to undergo transformation, this transition was examined more closely by following the above outlined procedure but studying the sample by XRD every 6-12 hours. This was to ensure that no sign of the UK1 phase appeared during transition.

During X-ray diffraction analysis, the samples on the glass slides were each exposed to room temperature and relative humidity for a period of approximately 30 minutes.

3.3.2 Results and Discussion

Figure 3.6 shows the results for the X-ray diffraction analysis as a function of time and temperature for the pentahydrate and kornelite reagents. The amorphous ferric sulfate sample results at these temperatures (below 80°C) are not included. They were not included because the crystallization of ferric sulfates from an amorphous starting material is highly dependent on subtle changes in formation pathways. As a result, the results of the amorphous ferric sulfate reagent were quite variable. This complicated process and the results of it have been previously and carefully documented elsewhere (Xu et al., 2009). However, these experiments were performed so that the diffraction data could be analyzed and it could be confirmed that the UK1 phase did not appear at these lower temperatures. Kornelite was seen to dehydrate to pentahydrate above 60°C. Below 60°C kornelite remained stable, despite being within the stability field of pentahydrate. This is likely a result of a kinetic barrier of transformation. The pentahydrate was not seen to rehydrate to kornelite in any of the two week periods at any temperature studied. This likely reflects the fact that the kinetic barriers were never overcome.

No peaks associated with UK1 were observed, either during the transition between kornelite to pentahydrate, or in the minerals formed through the hydration and/or deliquescence of the amorphous ferric sulfate. Where the kornelite to pentahydrate transition was observed, there was no sign of the

transitory UK1. These results are consistent with the work of Kong et al. (2011), Ackerman et al. (2009; Xu et al. (2009) and Posnjak and Merwin (1922). It seems evident, therefore, through analysis of the large sample volume and the small sample volume experiments, that UK1 is not observed below 80°C.

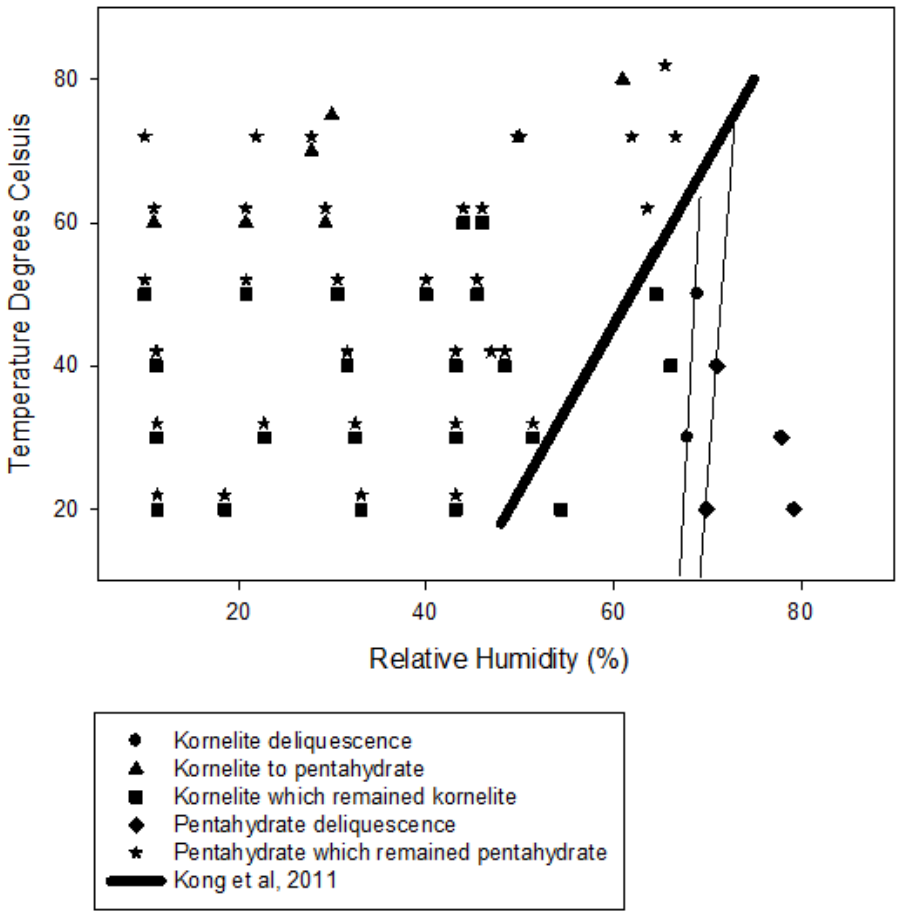

Figure 3.6: Observed phase transitions of kornelite and pentahydrate as reagents. The thick black line indicates the experimentally determined phase boundary from Kong et al. (2011). The thin lines connect the lowest relative humidity where kornelite (dot) or pentahydrate were observed to deliquesce.

UK1 seems to be a transient phase under the conditions of the present study above 85°C and does not occur below 85°C. When kept at room temperature and moderate relative humidities (20%-40%), UK1 was seen to persist for up to a period of 9 months.

3.4 Amorphous Ferric Sulfate at 90°C

The experiments outlined above make it evident that the UK1 phase does not grow at temperatures below 85°C and also does not develop with either kornelite or pentahydrate as the precursor phase. Therefore, another round of experiments were conducted focusing solely on amorphous ferric sulfate as the reagent and keeping a consistent temperature of 90°C and RH of 23.07%. The only variable for these experiments was that of time. These experiments would serve to better classify the window of UK1 formation as the entire reagent volume would be exposed to the humidity controlled atmosphere more evenly and the transformation into UK1 would be more consistent and predictable.

The experiments conducted following that outlined in Ling and Wang (2009) used a large (2g) volume of reagent material. This allowed for sufficient resultant phase powder to perform a back-packed X-ray analysis. Attempts to grow a single phase powder to make it possible to find a unit cell using powder were unsuccessful. However, using a smaller amount of reagent dusted upon a glass slide could result in the formation of larger grains being grown of the UK1 phase which could then be analyzed using single crystal techniques. Therefore, with these goals in mind, another series of experiments involving dusted powders of reagents on glass slides was conducted.

3.4.1 Experimental Method

Experiments were performed at 90°C with a light dusting of amorphous ferric sulfate pentahydrate above saturated solutions made of $MgCl_2$ and NaI (RH 23.07% and 23.25%) These experiments followed the same procedure as those described in section 3.3, but the samples were removed for analysis after much shorter time durations as the smaller reagent volume would allow reactions to take place more quickly.

3.4.2 Results and Discussion

It was seen that in all cases rhomboclase was the first to form. This rhomboclase formation first occurred between 7 and 8 hours. After 12 hours a mixture of rhomboclase, pentahydrate and UK1 was observed. At exposure times of longer than 27 hours only rhomboclase and pentahydrate remained. At no time was the mineral kornelite observed (Table 3.5). As well, at no time during the analysis were only the minerals rhomboclase and UK1 seen to occur alone together. This also suggests that UK1 is transitory or has a very limited window of stability. The mineral grains grown in these experiments were analyzed with optical microscopy with the hope that a large enough grain of UK1 could be selected for single crystal analysis. Unfortunately, the grains never grew large enough even to separate them into single units. To find the atomic structure of a mineral phase requires either a single-phase powder or a single crystal large enough for analysis. Neither of these were successfully found here. However, the possibility of finding a possible unit cell still remained.

3.4.3 Problems Encountered

The UK1 phase was created using an amorphous ferric sulfate pentahydrate reagent. This reagent originated from one jar obtained from Acros Organics. When the material was finished, the reagent was re-ordered from Acros Organics using the same identification code. Unfortunately, the

material had been produced to be a crystalline ferric sulfate pentahydrate, which is not a reagent suitable for the formation of UK1.

Ferric sulfate and hydrous ferric sulfate were ordered from several other chemical supply companies but they likewise produced either crystalline pentahydrate or the mineral ferricopiapite [$Fe0.66Fe4(SO_4)_6(OH)_2 \cdot 20(H_2O)$]. Efforts to form amorphous material in the laboratory were likewise unsuccessful.

The inability to acquire more of the amorphous reagent needed to form UK1 meant that several important analyses could not be done. For starters, a real-time X-ray diffraction analysis at 90°C and RH 23.07% would have allowed for a better understanding of the phase transitions involved in the transformation of the reagent. Do the UK1 and pentahydrate grow together immediately or does one grow slightly before the other, for example? Information obtained in a real-time experiment could have helped predict the hydrous nature of this phase.

As well, a weight loss experiment of the UK1 mixed-phase powder could have, when considering the percentages of rhomboclase and pentahydrate using Rietveld analysis, allowed for an approximation of the water content of the UK1 phase. Without this weight loss experiment the water content of the material can only be hypothesized and there are no quanitfiable means to support the hypothesize.

A key requirement for further analysis of the UK1 phase is to obtain the amorphous ferric sulfate pentahydrate reagent.

Table 3.5: Ferric Sulfate at 90 degrees dusted on a glass slide and exposed to RH ~23%. UK1 was never observed to form without the presence of pentahydrate and rhomboclase.

Time (hours)	Product
7	4
7.5	4
8	4
8.5	4
9	4
9.5	2,3,4
10	2,3,4
11	2,3,4
12	2,3,4
13	2,3,4
13.5	2,3,4
14	2,3,4
16	2,3,4
17	2,3,4
18.5	2,3,4
20	2,3,4
22	2,3,4
23	2,3,4
25	3,4
26	3,4
28	3,4

Legend
1- kornelite
2- UK1
3- pentahydrate
4- rhomboclase

3.5 Synchrotron Based X-Ray analysis

Unfortunately, a single phase powder of UK1 was never synthesized and a UK1 crystal large enough for single crystal diffraction analysis was never grown. However, several of the experiments yielded a mixed-phase powder where the UK1 pattern was dominant. A sample containing the highest fraction of UK1 was analyzed using synchrotron generated X-rays in order to take advantage of the sharp peak profiles and high intensities generated by this higher energy source. Using a synchrotron radiation source resulted in higher intensities, higher signal to noise ratios and a greater accuracy of the measured peak positions With this information and a thorough analysis of the various Panalytical X'pert Pro™

diffractometer diffraction measurements, a system for identifying peaks belonging to the UK1 was developed and the identified peaks were then used in an effort to identify a unit cell for this phase.

3.5.1 Experimental Method

A 'Mail-In Sample Kit' was requested from the Advanced Photon Source at the Argonne National Laboratory in Argonne, Illinois. The kit included a small Kapton capillary vial (inner diameter 0.80mm). The mixed-phase powder was placed in the capillary vial and care was taken to ensure that there was as little pore space present in the sample as possible. This was done through high-intensity mechanical vibration to pack the powder densely. The vials were then viewed through microscope to ensure that the vibrations were successful in packing the vial as completely as possible. This was done in order to avoid phase transition during transport. Once packed, the capillary was then placed in the provided mounting base, covered with a supplied magnetic cap. The sample was analyzed at the 11-BM Powder Diffraction Beamline. Experimental parameters are summarized in Table 3.6.

Table 3.6: Details of synchrotron beamline specifications. Retrieved from http:11bm.xor.anl.gov

Monochromator	Si(111) double crystal (bounce up geometry)
Focusing	Sagittally Bent Si(111) Crystal (Horz), 1 meter Si/Pt mirror (Vert)
Beamsize	1.5 mm (horizontal) x 0.5 mm (vertical) focused at sample
Detection System	12 independent analyzer sets with 2θ separation of ~ 2° Si(111) analyzer crystals and LaCl3 scintillation detectors
Angular Coverage	2θ range: 0.5° - 130° at ambient temp (Qmax≈ 28 Å-1 at 30 keV)
Resolution	ΔQ/Q ≈ 2×10-4 (min. 2θ step size = 0.0001°)

3.5.2.1 Analysis of the Synchrotron pattern

The powder diffraction pattern generated at the Argonne National Laboratory was similar to that originally produced by the Panalytical X'pert Pro™ diffractometer, however, there were small differences in the d-spacings and the diffraction peaks had a lower full width at half maximum (FWHM). Peaks explained by classified ferric sulfates in the ICDD database were determined by fitting the X-ray diffraction pattern using Rietveld analysis to predict the contributions from pentahydrate, rhomboclase and kornelite (Figure 3.7). While the original sample did not include kornelite peaks, the synchrotron pattern suggested that kornelite had developed during transport to the beamline or was not detected by the Panalytical measurements.

A complete list of peaks not accounted for by intensity calculated using Rietveld simulation of the diffraction contribution of the known phases in the synchrotron pattern is found in Table 3.7. These d-spacings reflect the largest 48 d-spacings of every peak present in the synchrotron pattern that could not be explained by kornelite, pentahydrate or rhomboclase (Figure 3.7). While none of the peaks shown in Table 3.7 are explained by the included minerals, not all are reasonably considered to be part of the UK1 pattern. For example, there was the development of two broad peaks at low angle, having d-spacings of 16.56Å and 8.21Å. These peaks were not explained by the recognised minerals, and did not correspond to those peaks which had been identified as belonging to UK1 using the Panalytical X'pert Pro™ diffractometer patterns (see below). These peaks were not included in the unit cell analysis because of their different peak shapes suggested they belong to an additional minor phase, these peaks were never observed in the Panalytical X'pert Pro™ diffractometer patterns.

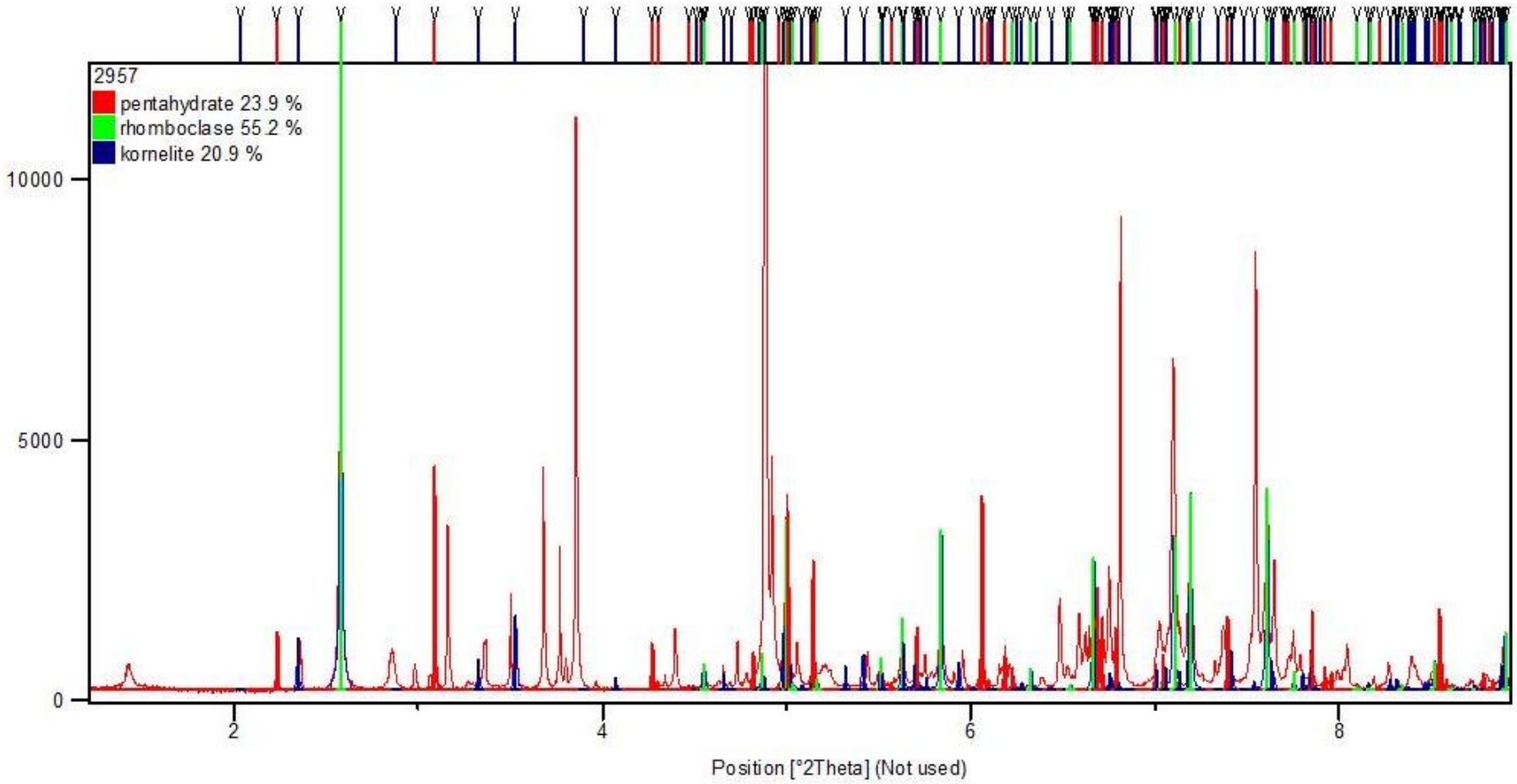

Figure 3.7: Synchrotron data including Rietveld of pentahydrate (Majzlan, 2005), rhomboclase (Merieter, 1974) and kornelite (Robinson and Fang, 1973). Unidentified peaks belong to one of at least two unknown phases.

A list of identified, consistent, UK1 peaks is listed in Table 3.8. These peaks were complied taking into account the Panalytical X-pert Pro™ patterns, rather than the more sensitive synchrotron patterns. This was done through the following reasoning: The fact that these peaks are consistently present in the less-sensitive Panalytical X-pert Pro™ suggests that they are the most prominent and the most intense peaks belonging to UK1. The consistent peaks maintain a consistent relative intensity to each other. For example, the peak at d-spacing 6.13 was always about twice as tall as the peaks at d-spacing 6.28 and d-spacing 6.43. This pattern of consistency of relative intensity was retained for all the peaks specified in Table 3.8. Any unit cell identified as possibly describing UK1 must be able to account for all the peaks in Table 3.8 listed as "consistent d-spacings".

The synchrotron patterns demonstrate a number of other possible peaks belonging to UK1, due to the increased sensitivity. These peaks are listed in Table 3.8 as "possible d-spacings". Any unit cell identified as possibly describing UK1 would be considered more reasonable if it could also account for all, or many, of these "possible peaks".

There is also a set of peaks in the synchrotron pattern which can be demonstrated to *not* belong to UK1 but to still be un-attributable to any other known phase in the system. For example, peaks such as that at d-spacing 6.76Å and 10.02Å. To demonstrate, Figure 3.8 shows two Panalytical X'Pert Pro patterns. The 6.76Å peak is not seen in the upper pattern at all. In the lower pattern, for a different sample,, the 6.76Å peak is almost as intense as the 6.13Å peak belonging to UK1. This inconsistency of intensity in relation to UK1 suggests that this peak, and others like it, belong to a different phase. A list of peaks that are identified through these variations of intensities between different sample measurements can be found in Table 3.8 listed as "d-spacings not belonging to UK1".

Table 3.7: The first 48 unaccounted for peaks in the synchrotron beamline pattern, omitting peaks explained through Rietveld analysis including kornelite, pentahydrate and rhomboclase. Not all these peaks are considered as reasonably belonging to UK1 due to variations in intensity and FWHM.

D-spacings	Relative intensity %	D-spacings	Relative intensity %	D-spacings	Relative intensity %
16.53977	2.44	4.94769	1.58	3.630	2.09
10.00346	4.13	4.84518	100	3.596	6.56
8.2704	3.5	4.81015	21.11	3.577	4.77
7.92936	2.26	4.73506	17.4	3.567	5.33
7.71391	1.25	4.68101	4.23	3.543	5.53
7.47893	17.17	4.55131	2.06	3.508	11.15
7.03035	4.46	4.35364	3.31	3.489	5.35
6.75942	10.02	4.11712	3.04	3.477	42.79
6.42795	19.88	4.09085	1.38	3.372	5.89
6.27738	12.69	4.00851	1.33	3.336	29.4
6.2269	2.76	3.97556	4	3.320	5.87
6.13273	51.17	3.84733	2.2	3.233	2.18
5.97037	0.24	3.82847	3.52	3.214	5.63
5.45346	1.26	3.81252	2.17	3.204	5.63
5.38159	5.92	3.70812	0.32	3.152	6.22
5.00201	4.23	3.65277	8.19	3.139	39.64

Table 3.8: d-spacings and relative intensities of intense and consistent UK1 peaks, as determined through analysis of numerous powder X-ray diffraction patterns showing the unknown phase, UK1. Also listed are possible d-spacings present in the synchrotron pattern and may be part of the UK1 peak profile as well as those which are not possible.

d-spacings-consistent UK1	Relative Intensity %
7.48	17.17
6.43	19.88
6.28	12.69
6.13	51.17
4.85	100
4.81	24.94
3.65	8.19
3.48	42.79
3.34	29.4
3.14	39.64
3.10	11.41
2.95	4.03
2.82	2.85
2.64	5.55
2.49	5.67

d-spacings-possible UK1	d-spacings not belonging to UK1
7.03	10.00
6.23	7.93
5.45	7.71
5.01	6.76
4.74	5.38
4.68	4.95
3.98	4.35
3.85	3.96
3.60	3.63
3.58	3.37
3.57	
3.51	

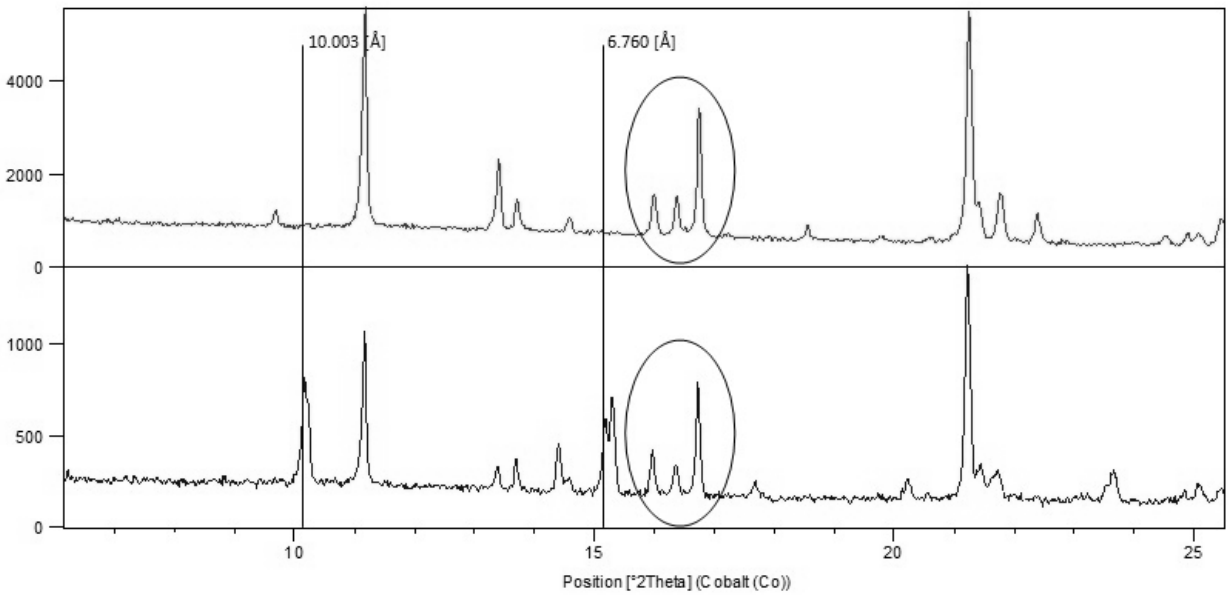

Figure 3.8: A comparison of two XRD patterns measured with the Panalytical XRD showing the unknown phase. The circled peaks belong to UK1. The peaks indicated as d-spacing 10.003 and d-spacing 6.760 can be seen to not develop in concert with UK1. That they do not form consistently with UK1, suggests that they belong to a different phase.

3.5.2.2 Indexing of UK1 Unit Cell - Methods

Numerous series of unit cell searches were conducted using the data from synchrotron pattern profile. All unit cell searches began with those peaks listed in Table 3.7 as "consistent" and these were then added upon with other possible peaks. It was attempted to maintain a methodology which included, for example, adding all unindexed peaks with a FWHM between 0.0100 – 0.0125, or adding the peaks listed in Table 3.8 as "possible" one at a time. Using this system a unit cell was eventually found.

The unit cell which explained all the peaks attributed to UK1 was modeled using ITO (Visser, 1969), a computer program designed to identify possible unit cells based on the d-spacings chosen for analysis. This program is embedded in the program package HIGHSCORE™.

The peaks included in the unit cell determination for this cell were all the "consistent" UK1 peaks listed in Table 3.8 and all of the "possible" peaks listed in Table 3.7. The cell did not include any of the peaks in Table 3.8 listed as "not-belonging" to UK1. Also excluded were the wide-peaks at d-spacing 16.559Å and 8.270Å with larger FWHM, as their low, broad peak shapes were inconsistent with the other peaks of the UK1 pattern. Excluded as well were any peaks lower than a d-spacing of 2.49Å.

The unit cell has a figure of merit (FOM) of 53.30, which is of a very high quality (a minimum desired being 10 (HIGHSCORE™)). The FOM is a calculation which compares how well the selected unit cell explains the peaks indicated (Smith and Snyder, 1979). The cell found here with an FOM of 53 is a monoclinic cell of dimensions:

a = 7.532(3)Å b = 12.551(6)Å c = 7.077(4)Å β = 96.775(8)°. The unit cell volume is 664.4Å.

Figure 3.9a, shows a reasonable agreement of the refined peak positions for UK1 cell for the synchrotron data and Figure 3.9b gives the agreement of the refined peak positions of the pentahydrate cell also using the synchrotron data, for comparison. ITO™ was successful in finding the unit cell provided by Majzlan (2005), which lends confidence to the cell identified for UK1. Table 3.9a provides details of the unit cell and peak refinement associated with UK1 unit cell, with the observed peaks used to identify the cell and the calculated peaks that could be explained by the cell. Table 3.9b provides a list of all the peaks left unindexed on the synchrotron pattern up to a d-spacing of 3.00Å. Complete details of the unit cell refinement are available in Appendix A.

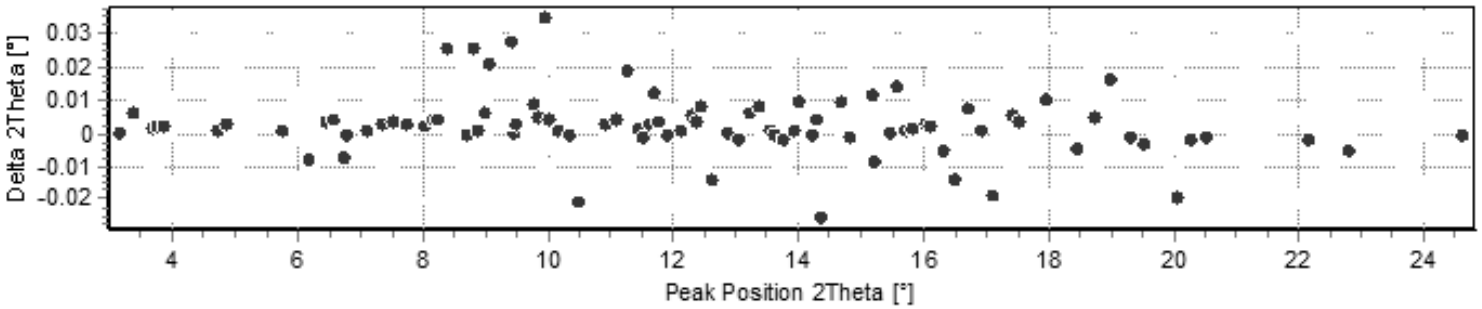

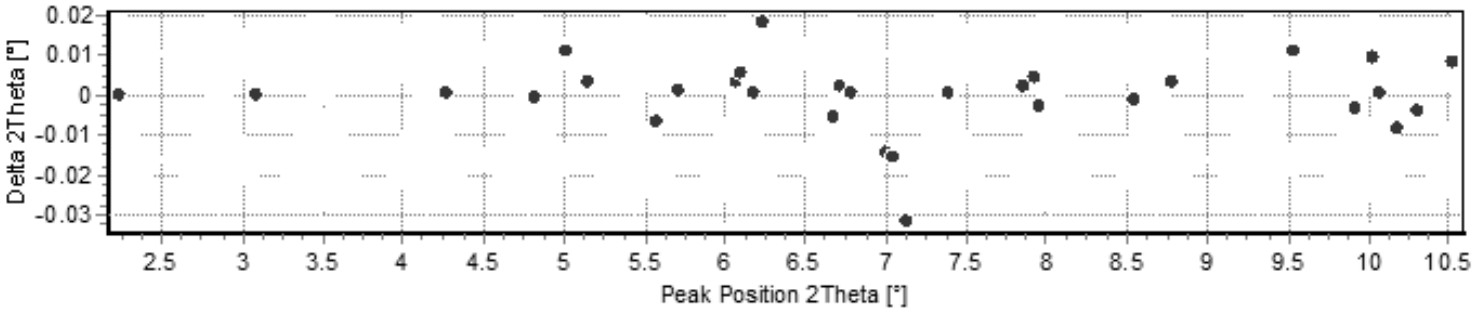

Figure 3.9a (above): The refinement scatter pattern for the unknown phase unit cell as determined using HIGHSCORE™. Figure 3.9b (below): The refinement scatter pattern for the pentahydrate unit cell, found using the same system as that for unknown phase. The distribution is similar to that of 3.9a, the UK1 unit cell refinement.

Table 3.9a: Calculated and observed d-spacings for the indexed unit cell

No.	h	K	l	d-sp. (c) [Å]	d-sp. (o) [Å]	d-sp. (d) [Å]
1	0	1	0	12.5574		
2	1	0	0	7.4526	7.4813	-0.028662
3	0	0	1	7.0430	7.0337	0.009307
4	1	1	0	6.4089	6.4279	-0.019013
5	0	2	0	6.2787	6.2774	0.001338
6	0	1	1	6.1428	6.1327	0.010138
7	0	1	-1	6.1428		
8	1	0	-1	5.4380	5.4542	-0.01625
9	1	1	-1	4.9902	5.0026	-0.01242
10	1	0	1	4.8500	4.8453	0.004755
11	1	2	0	4.8018	4.8102	-0.008393
12	0	2	1	4.6867	4.7356	-0.04891
13	0	2	-1	4.6867		
14	1	1	1	4.5243	4.3536	0.170657
15	0	3	0	4.1858	4.2081	-0.022323
16	1	2	-1	4.1106	3.9756	0.135017
17	1	2	1	3.8383	3.8470	-0.00879
18	2	0	0	3.7263		
19	1	3	0	3.6496	3.6528	-0.003199
20	0	3	-1	3.5983		
21	0	3	1	3.5983	3.5960	0.00233
22	2	1	0	3.5723	3.5764	-0.004088
23	0	0	2	3.5215	3.5082	0.013259
24	2	0	-1	3.4610	3.4775	-0.016477
25	0	1	-2	3.3907		
26	0	1	2	3.3907		
27	2	1	-1	3.3366		
28	1	0	-2	3.3343	3.3356	-0.001273
29	1	3	-1	3.3170		
30	1	1	-2	3.2226		
31	2	2	0	3.2045		
32	1	3	1	3.1688		
33	2	0	1	3.1485		
34	0	4	0	3.1394	3.1387	0.000618
35	0	2	-2	3.0714	3.0985	-0.027153
36	0	2	2	3.0714		
37	2	1	1	3.0540		
38	1	0	2	3.0522		
39	2	2	-1	3.0310		
40	1	1	2	2.9659		
41	1	2	-2	2.9448	2.9456	-0.000809

Table 3.9b: Unindexed peaks

d-spacing [Å]
16.54038
10.00337
7.92936
7.71281
6.7577
6.2269
5.97037
5.38366
4.95005
4.54952
4.35364
4.00744
3.97556
3.81252
3.62969
3.56746
3.37165
3.0659

3.5.2.3 Indexing of the UK1 Unit Cell - Discussion

The unit cell above accounts for the "consistent" UK1 peaks and all "possible" UK1 peaks. It does not explain any of the peaks known not to belong to UK1. This lends confidence to the reasonableness of this cell. However, because the sample was a mixture of several low symmetry phases and the UK1 phase always grew together with rhomboclase, the potential for peak overlap exists with the UK1 peaks and the rhomboclase peaks. The unit cell determined here, however, does not calculate any peaks that have d-spacings matching those of rhomboclase. This lends further support in the argument for this cell and reduces the concern over peak overlap.

A list of all the peaks found in the synchrotron pattern and their corresponding assignments can be found in Table 3.10. The peaks assigned to rhomboclase, pentahydrate or kornelite were determined using Rietveld analysis and are identified as such. Those identified as UK1 are those peaks outlined in Table 3.7 as consistent. All the peaks which could be explained by the unit cell found by HIGHSCORE™ are identified as UK1-PC. (possible or calculated). All other peaks are separated into three classes. Class 'A' refers to those two peaks whose broad peak shape suggests that they did not belong to UK1. Class 'B' refers to peaks which were excluded based on an inconsistent relative intensity to known peaks and are those that are outlined in Table 3.8 as "not belonging" to UK1 for this reason. Finally, class 'C' refers to all peaks not explained by any of the outlined designations and that therefore remain ambiguous. The Class 'C' peaks are typically of very low intensity in the synchrotron so they were present only as small humps in the Panalytical X'Pert Pro patterns or were not present at all. Class 'C' may also be peaks that are so close to other peaks in the synchrotron pattern that the two peaks are likely to be indistinguishable from each other in the Panalytical X'Pert Pro pattern. As a result, whether they belong to Class 'B' or not is uncertain. The peaks of Class 'B' and Class 'C' may belong to one other unindexed phase in this ferric sulfate system above 80°C or may represent more than one other phase.

Table 3.10: First 180 peaks of the synchrotron pattern. Assignments of kornelite, pentahydrate and rhomboclase are based on Rietveld analysis. UK1 refers to all peaks identified as consistently belonging to this one phase (Figure 3.7). UK1-PC are those peaks predicted by the HIGHSCORE™ unit cell. Class A are peaks left unindexed with a FWHM of >0.0150. Class B are peaks seen to be inconsistent in their relative intensities in relation to UK1. Class C are all peaks still left unexplained. The peaks of Class B and Class C may belong to one phase.

Pos. [°2Th.]	Assignment	H	K	l	d-spacing [Å]	Rel. Int. [%]	FWHM
1.4288	Class A				16.56548	2.58	0.0239
2.0371	Kornelite	0	1	-1	11.61906	0	0.0016
2.0371	Kornelite	0	1	1	11.61906	0	0.0205
2.236	Pentahydrate	0	0	1	10.58555	4	0.0065
2.3496	Kornelite	0	2	0	10.07399	3.55	0.0036
2.3662	Class B				10.00337	4.42	0.001
2.5822	Rhomboclase	0	2	0	9.1665	52.55	0.0281
2.862	Broad peak				8.2704	3.76	0.0053
2.8794	Kornelite	0	2	-1	8.22065	0.04	0.0115
2.8794	Kornelite	0	2	1	8.22065	0.04	0.0086
2.9853	Class B				7.92897	2.59	0.0078
3.069	Class B				7.71281	0.95	0.0118
3.0917	Pentahydrate	0	1	-1	7.65629	15.39	0.09
3.0917	Pentahydrate	0	1	1	7.65629	15.39	0.0034
3.1636	UK1				7.48215	14.98	0.001
3.3288	Kornelite	0	0	2	7.1111	2.05	0.0079
3.3659	UK1				7.03261	4.84	0.001
3.5029	Class B				6.75776	8.94	0.0139
3.5301	Kornelite	0	1	-2	6.7057	5.17	0.0129
3.5301	Kornelite	0	1	2	6.7057	5.17	0.001
3.6821	UK1				6.42894	20	0.012
3.771	UK1				6.27745	13.15	0.001
3.8014	Class C				6.2272	3.12	0.0097
3.8599	UK1				6.13283	51.44	0.0087
3.898	Kornelite	0	3	-1	6.07294	0.02	0.001
3.898	Kornelite	0	3	1	6.07294	0.02	0.001
3.964	Class C				5.97188	0.53	0.001
4.0748	Kornelite	0	2	-2	5.80953	0.77	0.011
4.0748	Kornelite	0	2	2	5.80953	0.77	0.012
4.2704	Pentahydrate	0	2	0	5.54356	3.13	0.01
4.3	Pentahydrate	1	0	0	5.50537	0.55	0.09
4.3404	UK1-PC				5.45422	1.61	0.0124
4.3973	Class B				5.38363	5.89	0.0092
4.4729	Pentahydrate	0	0	2	5.29278	0	0.001
4.5106	Kornelite	1	0	0	5.24849	0.03	0.011
4.5309	Pentahydrate	1	0	-1	5.22505	0.14	0.0083
4.5481	Kornelite	1	1	-1	5.20528	1.25	0.0054
4.554	Rhomboclase	0	1	1	5.19849	1.78	0.001
4.6612	Kornelite	1	1	0	5.07899	1.03	0.011

4.7001	Kornelite	0	4	0	5.037	0.09	0.0116
4.7322	UK1-PC				5.00282	4.49	0.0243
4.7827	Class B				4.95005	1.98	0.0195
4.8013	Pentahydrate	1	1	0	4.93093	0.04	0.006
4.8209	Pentahydrate	0	2	-1	4.9109	2.58	0.0067
4.8209	Pentahydrate	0	2	1	4.9109	2.58	0.0165
4.8488	Kornelite	0	3	-2	4.88263	0.16	0.001
4.8488	Kornelite	0	3	2	4.88263	0.16	0.0239
4.8694	Rhomboclase	2	0	0	4.862	2.48	0.0016
4.8792	Kornelite	1	0	-2	4.85224	0.77	0.0205
4.8863	UK1				4.84518	100	0.0065
4.9219	UK1				4.81015	21.43	0.0036
4.9567	Pentahydrate	0	1	-2	4.77643	0.44	0.001
4.9567	Pentahydrate	0	1	2	4.77643	0.44	0.0281
4.9829	Kornelite	1	2	-1	4.75128	3.69	0.0053
4.9864	Kornelite	0	4	-1	4.74802	3.91	0.0115
4.9864	Kornelite	0	4	1	4.74801	3.91	0.0086
5.0002	Rhomboclase	1	0	1	4.73492	11.8	0.0078
5.0091	Pentahydrate	1	1	-1	4.72648	12.33	0.0118
5.0188	Kornelite	1	1	-2	4.71737	1.59	0.09
5.0378	Rhomboclase	2	1	0	4.69954	0.39	0.0034
5.0578	UK1-PC				4.68101	4.64	0.001
5.0864	Kornelite	1	2	0	4.65465	0.27	0.0079
5.1305	Kornelite	0	1	-3	4.61471	0.31	0.001
5.1305	Kornelite	0	1	3	4.61471	0.31	0.0139
5.1441	Pentahydrate	1	0	1	4.60254	8.89	0.0129
5.1643	Rhomboclase	1	1	1	4.58448	0.74	0.001
5.1657	Rhomboclase	0	4	0	4.58325	0.71	0.012
5.2059	Class C				4.54794	2.54	0.001
5.2349	UK1-PC				4.52269	2.01	0.0097
5.3212	Kornelite	1	1	1	4.44944	1.62	0.0087
5.416	Kornelite	1	2	-2	4.37167	2.43	0.001
5.4384	Class B				4.35364	3.8	0.001
5.5124	Rhomboclase	2	2	0	4.2952	2.24	0.001
5.5197	Kornelite	0	2	-3	4.2895	1.08	0.011
5.5197	Kornelite	0	2	3	4.2895	1.08	0.012
5.57	Pentahydrate	1	1	1	4.25082	0.44	0.01
5.6283	Rhomboclase	1	2	1	4.20683	4.88	0.09
5.6337	Kornelite	1	3	-1	4.20278	3.17	0.0124
5.6975	Kornelite	1	2	1	4.1558	1.71	0.0092
5.7078	Pentahydrate	1	0	-2	4.14827	4.27	0.001
5.7255	Kornelite	1	3	0	4.13545	0.29	0.011
5.7512	UK1-PC				4.117	3.52	0.0083
5.7606	Kornelite	0	4	-2	4.11032	0.76	0.0054
5.7606	Kornelite	0	4	2	4.11032	0.76	0.001
5.7867	Class C				4.09178	1.98	0.011

5.8387	Rhomboclase	0	3	1	4.05533	11.06	0.0116
5.9087	Class A				4.00738	1.86	0.0243
5.9363	Kornelite	1	1	-3	3.98873	1.89	0.0195
5.9562	Class B				3.97541	3.57	0.006
6.0203	Kornelite	1	3	-2	3.93311	0.14	0.0067
6.0617	pentahydrate	1	2	0	3.90632	13.34	0.0165
6.0946	pentahydrate	1	1	-2	3.88523	0.72	0.001
6.1076	Kornelite	0	5	-1	3.87699	0.04	0.0239
6.1076	Kornelite	0	5	1	3.87699	0.04	0.0016
6.1138	Kornelite	0	3	-3	3.87302	0.02	0.0205
6.1138	Kornelite	0	3	3	3.87302	0.02	0.0065
6.1547	UK1-PC				3.8473	2.72	0.0036
6.1856	pentahydrate	0	2	-2	3.82815	2.16	0.001
6.1856	pentahydrate	0	2	2	3.82815	2.16	0.0281
6.211	Class C				3.81252	2.63	0.0053
6.2237	Rhomboclase	2	3	0	3.80471	0.92	0.0115
6.2277	pentahydrate	1	2	-1	3.80229	1.54	0.0086
6.2508	Kornelite	1	0	2	3.78827	0.1	0.0078
6.2748	Kornelite	1	3	1	3.77375	0.47	0.0118
6.276	Kornelite	1	2	-3	3.77307	0.47	0.09
6.3266	Rhomboclase	1	3	1	3.74288	1.37	0.0034
6.3604	Kornelite	1	1	2	3.72303	0.19	0.001
6.386	UK1-PC				3.70812	0.8	0.0079
6.4356	Kornelite	1	4	-1	3.6796	0.13	0.001
6.483	UK1				3.65271	8.57	0.0139
6.5161	Kornelite	1	4	0	3.63416	0.07	0.0129
6.524	Class B				3.62977	2.49	0.001
6.5425	Rhomboclase	2	0	1	3.6195	0.36	0.012
6.5853	UK1-PC				3.596	6.98	0.001
6.6206	UK1-PC				3.57684	5.37	0.0097
6.6381	Class C				3.56746	5.79	0.0087
6.6603	Kornelite	0	0	4	3.55555	4.13	0.001
6.6674	pentahydrate	1	0	2	3.5518	9.13	0.001
6.669	Rhomboclase	2	1	1	3.55096	9.16	0.001
6.6786	Kornelite	1	2	2	3.54585	4.24	0.011
6.6875	pentahydrate	1	2	1	3.54113	7.05	0.012
6.7114	pentahydrate	0	0	3	3.52852	4.96	0.01
6.7502	Kornelite				3.50827	11.26	0.09
6.7549	UK1-PC	0	5	-2	3.50585	1.19	0.0124
6.7549	UK1-PC	0	5	2	3.50585	1.19	0.0092
6.7634	Kornelite	0	1	-4	3.50145	0.55	0.001
6.7634	Kornelite	0	1	4	3.50145	0.55	0.011
6.7767	Kornelite	1	4	-2	3.49454	0.38	0.0083
6.7872	pentahydrate	0	3	-1	3.48917	4.27	0.0054
6.7872	pentahydrate	0	3	1	3.48917	4.27	0.001
6.8046	Kornelite	1	3	-3	3.48026	0.4	0.011

6.8114	UK1				3.47679	43.1	0.0116
6.86	Kornelite	0	4	-3	3.45219	0.01	0.0243
6.86	Kornelite	0	4	3	3.45219	0.01	0.0195
7.0015	pentahydrate	1	1	2	3.38248	1.76	0.006
7.0039	Kornelite	1	4	1	3.38134	1.28	0.0067
7.024	Class B				3.37168	6.5	0.0165
7.0332	Kornelite	1	0	-4	3.36727	0.38	0.001
7.0347	rhomboclase	2	2	1	3.36655	0.43	0.0239
7.0435	pentahydrate	0	1	-3	3.36235	2.39	0.0016
7.0435	pentahydrate	0	1	3	3.36235	2.39	0.0205
7.0526	Kornelite	0	6	0	3.358	1.54	0.0065
7.0635	Kornelite	0	2	-4	3.35285	0.69	0.0036
7.0635	Kornelite	0	2	4	3.35285	0.69	0.001
7.1002	Rhomboclas				3.33555	29.77	0.0281
7.1013	UK1	2	4	0	3.33504	10.7	0.0053
7.1306	pentahydrate	1	2	-2	3.32132	1.27	0.0115
7.1309	Kornelite	1	1	-4	3.3212	1.26	0.0086
7.134	UK1-PC				3.31975	6.43	0.0078
7.1777	Kornelite	1	3	2	3.29955	1.96	0.0118
7.1917	rhomboclase	1	4	1	3.29316	13.64	0.09
7.2468	Kornelite	0	6	-1	3.26814	0.16	0.0034
7.2468	Kornelite	0	6	1	3.26814	0.16	0.001
7.3248	UK1-PC				3.23338	2.78	0.0079
7.3393	Kornelite	1	5	-1	3.227	0	0.001
7.3694	UK1-PC				3.21383	6.06	0.0139
7.3933	pentahydrate	1	0	-3	3.20348	5.08	0.0129
7.4101	Kornelite	1	5	0	3.19622	2.64	0.001
7.4162	Kornelite	1	2	-4	3.19359	2.08	0.012
7.4824	Kornelite	1	4	-3	3.16537	0.01	0.001
7.5184	UK1-PC				3.15026	5.42	0.0097
7.5373	Kornelite	0	3	-4	3.14235	0.48	0.0087
7.5373	Kornelite	0	3	4	3.14235	0.48	0.001
7.5458	UK1				3.13883	38.52	0.001
7.6055	rhomboclase	2	3	1	3.11424	13.96	0.001
7.626	Kornelite	1	1	3	3.10585	2.06	0.011
7.6404	Kornelite	1	5	-2	3.1	1.24	0.012
7.6444	UK1-PC				3.0984	11.93	0.01
7.6962	pentahydrate	1	1	-3	3.07759	0.02	0.09
7.7144	Kornelite	0	5	-3	3.07032	0.07	0.0124
7.7144	Kornelite	0	5	3	3.07032	0.07	0.0092
7.7191	pentahydrate	1	3	0	3.06845	0.07	0.001
7.7257	Class C				3.06582	3.31	0.011
7.7488	UK1-PC				3.05672	5.61	0.0083
7.7519	rhomboclase	0	6	0	3.0555	1.26	0.0054
7.7866	UK1-PC				3.0419	3.4	0.001
7.7988	rhomboclase	0	5	1	3.03713	1.11	0.011

3.5.2.4 Unit Cell Volume Consideration

Regarding the hydration state suggested by this cell, a plot of the unit cell volumes of normal hydrous ferric sulfate minerals is presented in Figure 3.10 with a line regression (standard error R=0.9873). There is an approximately linear increase in cell volume as the number of water molecules per formula unit is increased. Based on this trend and the equation for the line (f=y0+a*x), a normal ferric sulfate hexahydrate would have a unit cell corresponding to a volume of approximately *n*715Å^3 where n is 1 or 2 (the most common for normal hydrous ferric sulfates). The ferric sulfate hexahydrate identified by Posnjak and Merwin (1922) was considered to be likely monoclinic based on their optical measurements exhibiting inclined extinction. UK1 would therefore also be expected to have a monoclinic cell if it were a hexahydrate, as suggested by Ling and Wang (2009). This prediction by Ling and Wang (2009) was made upon a mixed-phase powder, however, so their hypothesis was an uncertain one.

The unit cell volume obtained here of 664Å^3, using the equation of the line f=y0+a*x, corresponds to a water content closer to 4.92. The fact that the identified unit cell did not correspond well with the volume predicted by Figure 3.9 of 715Å^3, suggests that the UK1 phase is not a ferric sulfate hexahydrate and could be a polymorph of ferric sulfate pentahydrate.

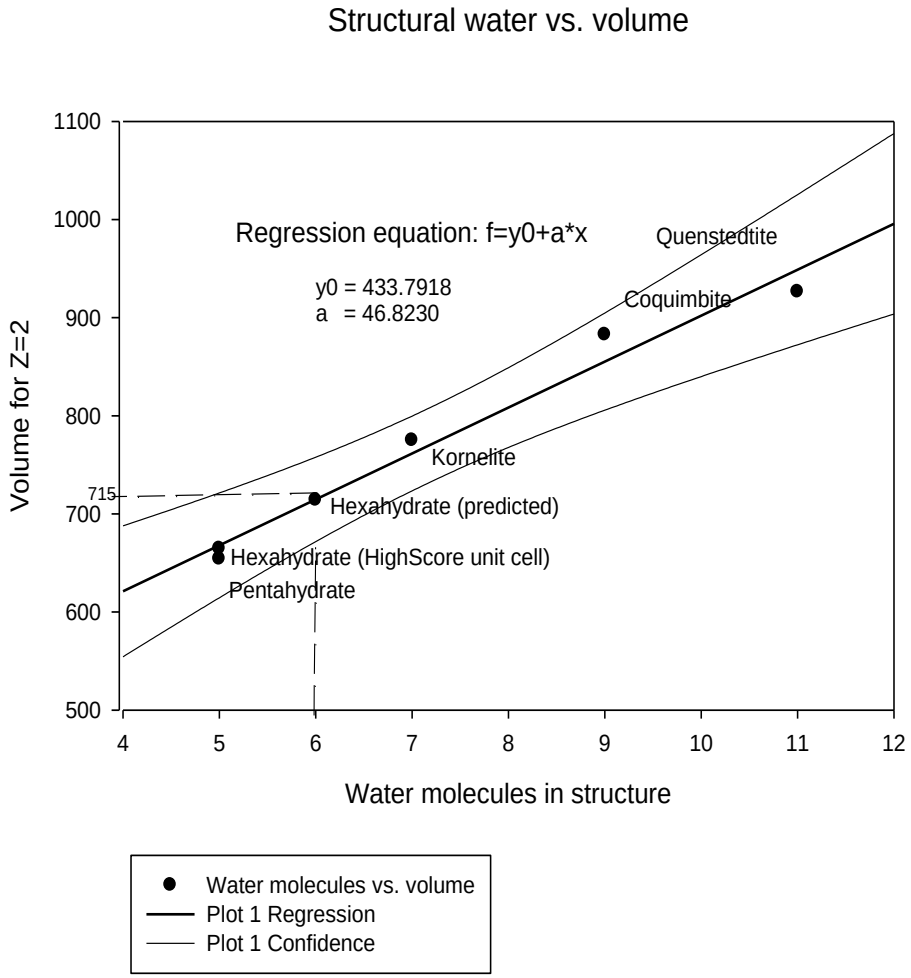

Figure 3.10: Unit cell volume as a function of structural water. The predicted unit cell volume for ferric sulfate hexahydrate is 715Å^3. The unit cell identified for the UK1 corresponds with an approximate mineral formula of also $Fe_2(SO_4)_3 \cdot 5H_2O$.

3.6 Kornelite, Pentahydrate and Hexahydrate

3.6.1 Kornelite

The mineral kornelite [$Fe_2(SO_4)_3 \cdot 7H_2O$)] was first discovered by Krenner(1888). Posnjak and Merwin (1922) included kornelite in their study of the system Fe_2O_3-SO_3-H_2O and described this mineral as monoclinic laths, elongated parallel to the *c* axis and noted a propensity for polysynthetic twinning. They also expressed some uncertainty about whether kornelite was a heptahydrate or octahydrate (Posnjak and Merwin, 1922).

Between the years of 1922 and 1973 several other analyses of kornelite were undertaken, but there remained some debate about the amount of structural water it contained. Kornelite was reported to have 7 waters (Dana, 1951), 7.5 waters (Cesbron, 1964) and 7.25 waters (Robinson and Fang, 1973). Despite these discrepancies, all these studies nevertheless agreed that kornelite has at least 6 structural waters and that the extra water(s) in question were not bound to a polyhedron. The structure, including hydrogen positions, was solved by Robinson and Fang (1973). Ackerman et al. (2009) refined the structure, determining more accurate hydrogen positions, and their solution involved 6.75 waters. The discrepancy between reported water molecules in the kornelite structure suggests that the mineral can retain its unit cell while having a variable percentage of water not bound to a polyhedron. Kornelite belongs to the monoclinic group of minerals with a space group of $P2_1/n$. The cell dimensions reported for kornelite by Ackerman et al. (2009) can be seen in Table 3.11:

Table 3.11: Kornelite unit cell dimensions (Ackerman et al., 2009).

a-	14.3125(3) Å	β-	96°813(14)’
b-	20.1235(5) Å	V-	1549.88(6)$Å^3$
c-	5.4310(1) Å	Z=	4

3.6.2 Kornelite Structure

The structure of kornelite is described as being composed of “corrugated sheets” (Ackerman et al., 2009; Robinson and Fang, 1973). These sheets are composed of ferric iron octahedra and sulfate tetrahedra. Each of the octahedrally coordinated ferric iron ions is coordinated with 3 water molecules and 3 oxygen atoms. Each of the oxygen atoms coordinating the ferric iron is shared with a sulfate tetrahedron, but each sulfate tetrahedron shares only two of its oxygen with the iron octahedra. Essentially, the kornelite sheet structure is composed of $Fe_2(SO_4)_3 \cdot 6H_2O$ chains which are connected to

each other through bridging oxygen. These sheets are stacked along the *a* axis, parallel to the (100) plane. Figure 3.11 illustrates such a sheet, as viewed down the *a* axis. The corrugated nature of these sheets becomes evident when the structure is viewed down the *c* axis (Figure 3.12). The 1.25-1.75 water molecules not bound to a polyhedron are found within the spaces formed from the corrugated structure.

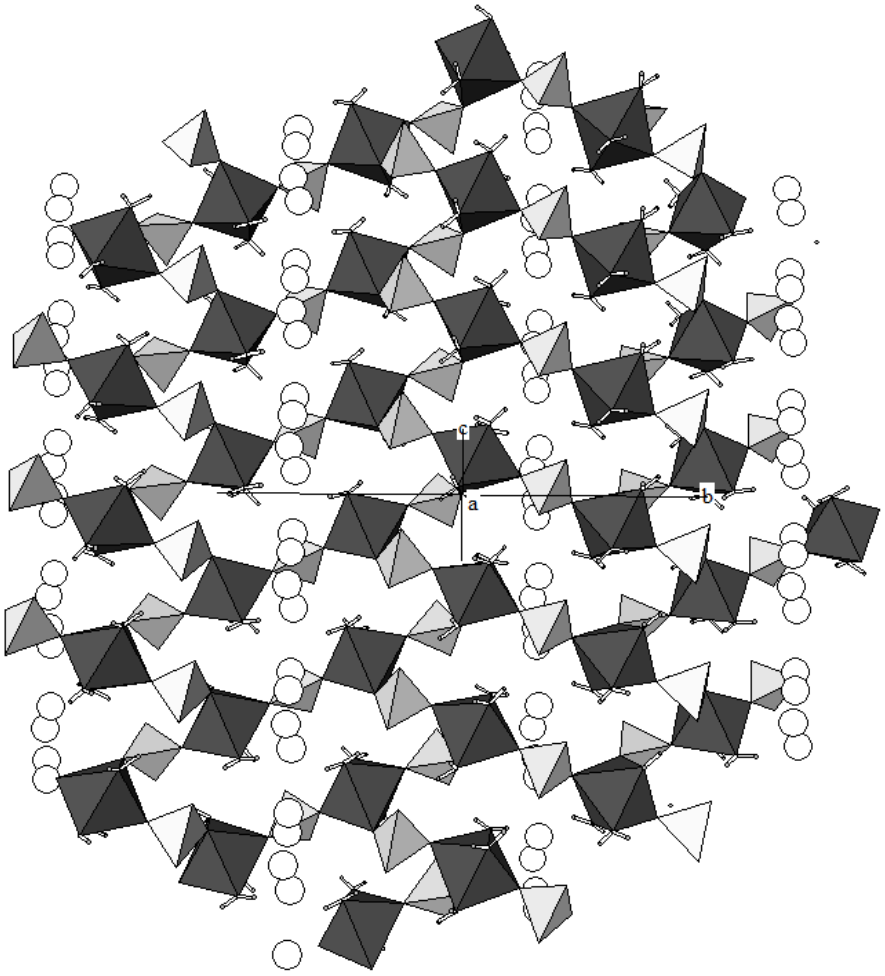

Figure 3.11: The kornelite sheet structure as viewed down the *a* axis. The kornelite sheet structure is composed of $Fe_2(SO_4)_3 \cdot 6H_2O$ chains which are connected to each other through bridging oxygen. Octahedra are drawn in dark grey, tetrahedra are in light grey and free water are white circles.

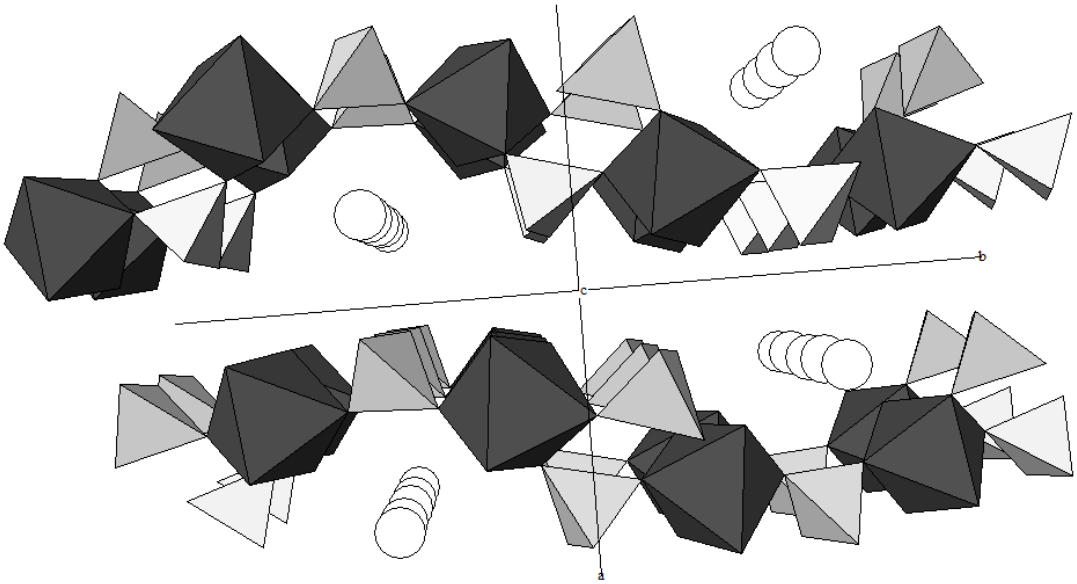

Figure 3.12: The kornelite structure as viewed down the *c* axis, illustrating the corrugated nature of the sheets and the location of the water molecules located between the sheets and not bound to an iron-containing polyhedron.

3.6.3 Pentahydrate Structure

The previous studies of the pentahydrate [$Fe_2(SO_4)_3 \cdot 5H_2O$] and the uncertainty about whether it was the original lausenite has been discussed in the introduction to this chapter. Therefore, only a description of its crystallographic structure is presented here. Ferric sulfate pentahydrate is monoclinic and belongs to the space group $P2_1/m$. The cell dimensions reported by Majzlan et al. (2005) are presented in Table 3.12.

Table 3.12: Pentahydrate unit cell dimensions (Majzlan et al., 2005)

a-	10.711(1) Å	β-	98°85(3)’
b-	11.084(1) Å	V-	654Å^3
c-	5.574(5) Å	Z-	2

Majzlan et al. (2005) describes the ferric sulfate pentahydrate as containing two ferric ions in octahedral coordination. The first ferric iron is coordinated with 4 oxygen atoms and 2 water molecules, while the second octahedron is coordinated with 3 oxygen atoms and 3 water molecules. In each case, the oxygen atoms belonging to the iron octahedra are shared with sulfate tetrahedra. The first symmetrically distinct sulfate tetrahedron shares three oxygen atoms with the three different iron-containing octahedra, while the second distinct sulfate tetrahedron shares only two of its oxygen atoms with iron-containing octahedra. These polyhedra are all connected to each other in a sheet formation similar to that found in kornelite (Figure 3.13). These sheets are likewise stacked along the *a* axis and when viewed down the *c* axis are also seen to have a corrugated arrangement (Figure 3.14). The lower water content of the pentahydrate structure, however, results in a more tightly constricted sheet than those of the kornelite structure, because the missing structural water gives rise to the two distinct sulfate tetrahedra.

In the kornelite structure, all sulfate tetrahedra share two bridging oxygen atoms with the iron-containing octahedra, which allows for a less constricted sheet structure. The additional 1.25-1.75 water molecules not bound to an iron-containing polyhedron of kornelite are also absent from the pentahydrate structure; their presence also contributes to the less constricted nature of the kornelite sheets.

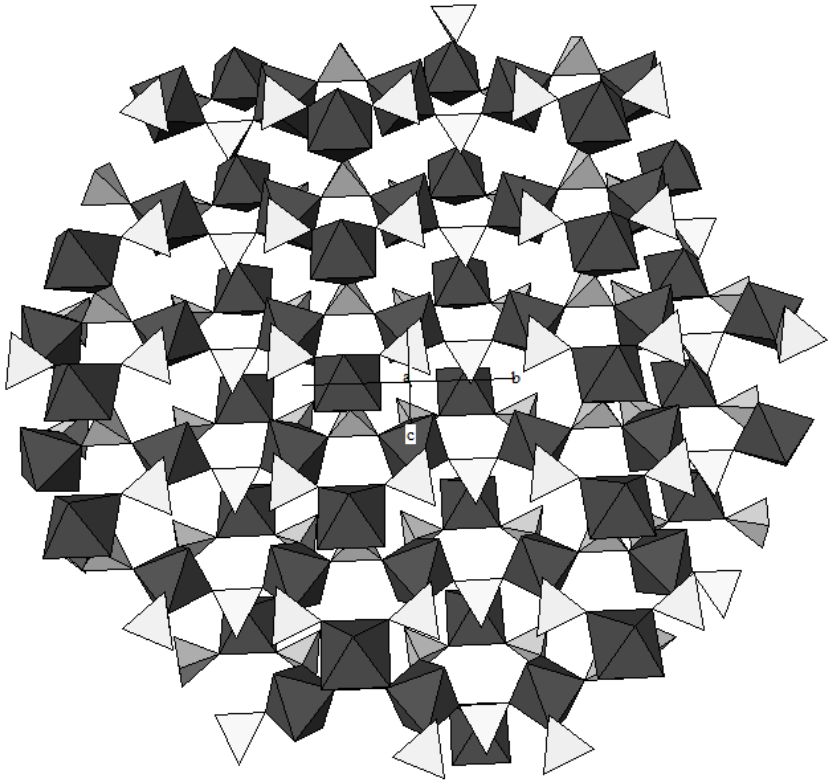

Figure 3.13: The pentahydrate structure as viewed down the a axis, demonstrating the similarity of the linkage of the octahedra and tetrahedra within the corrugated layer but the hydrogen bonded water molecules present in kornelite are absent.

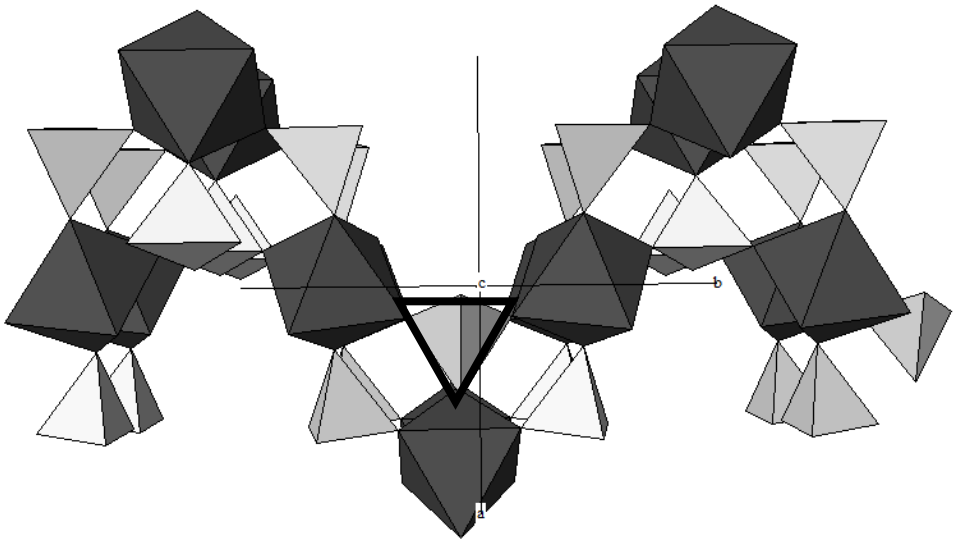

Figure 3.14: Pentahydrate mineral structure as viewed down the *c* axis. The S1 tetrahedron outlined in black shares three of its oxygen with a ferric sulfate octahedron, accounting for the constricted nature of the sheet, when compared to that of kornelite, whose sulfate tetrahedra share only 2 of their oxygen with the Fe octahedra.

3.6.4 Hexahydrate

Robinson and Fang (1973) postulated in their study of kornelite that a ferric sulfate hexahydrate may also be found in nature, when kornelite dehydration occurs and all of those water molecules not bound to a polyhedron are removed. This hexahydrate would simply consist of the kornelite sheets held together by hydrogen bonds. Upon further dehydration, a structural water would also be lost, and the 6-hydrate chains would shrink and constrict into those of the pentahydrate structure discussed above. It would be therefore reasonable to assume that the hexahydrate atomic structure would look something similar to that seen in Figure 3.15. This structure would likely be monoclinic, in keeping with this group of hydrous ferric sulfates.

The unit cell for this "dehydrated kornelite" hexahydrate would likely fall within the ranges of kornelite and the pentahydrate (Table 3.13).

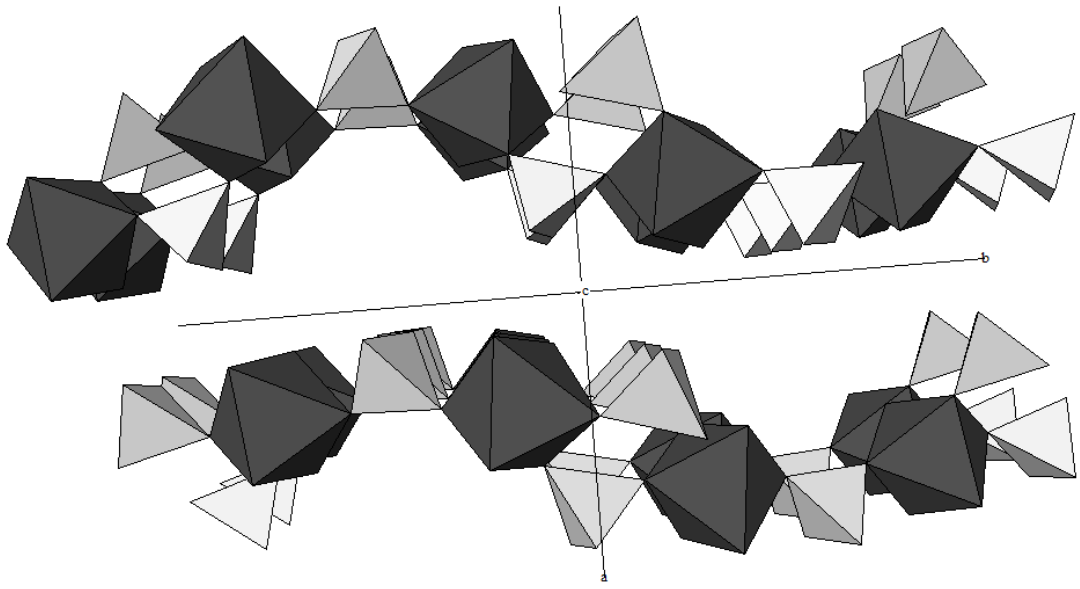

Figure 3.15: Possible hexahydrate mineral structure, as predicted first by Robinson and Fang, 1973. Viewed down the *c* axis. This structure is the same as that of kornelite, without the addition of water not bound to a polyhedron.

Table 3.13: Possible hexahydrate unit cell ranges based on Robinson and Fang (1973).

a- 14.312 - 10.71 Å	β- 96.81° – 98.85°
b- 20.123 - 11.084 Å	V- 710Å^3 (for Z=2)
c- 5.574 – 5.431 Å	

By comparing Figures 3.12 and 3.14, it becomes clear that the subtraction of a water molecule from the corrugated sheets of kornelite leads to a constriction of these sheets along the *b* axis, accounting for the significantly shorter *b* axis of pentahydrate (11.084Å as opposed to 20.123Å for kornelite). Figure 3.16 shows this effect in relation to the *b*-axis.

The same effect can be seen when considering the *a* axis. The *c* axis, however, is very little affected by the addition or subtraction of structural water occurring between kornelite and pentahydrate, as the sheet dimension in this direction is little affected by the change in hydration state.

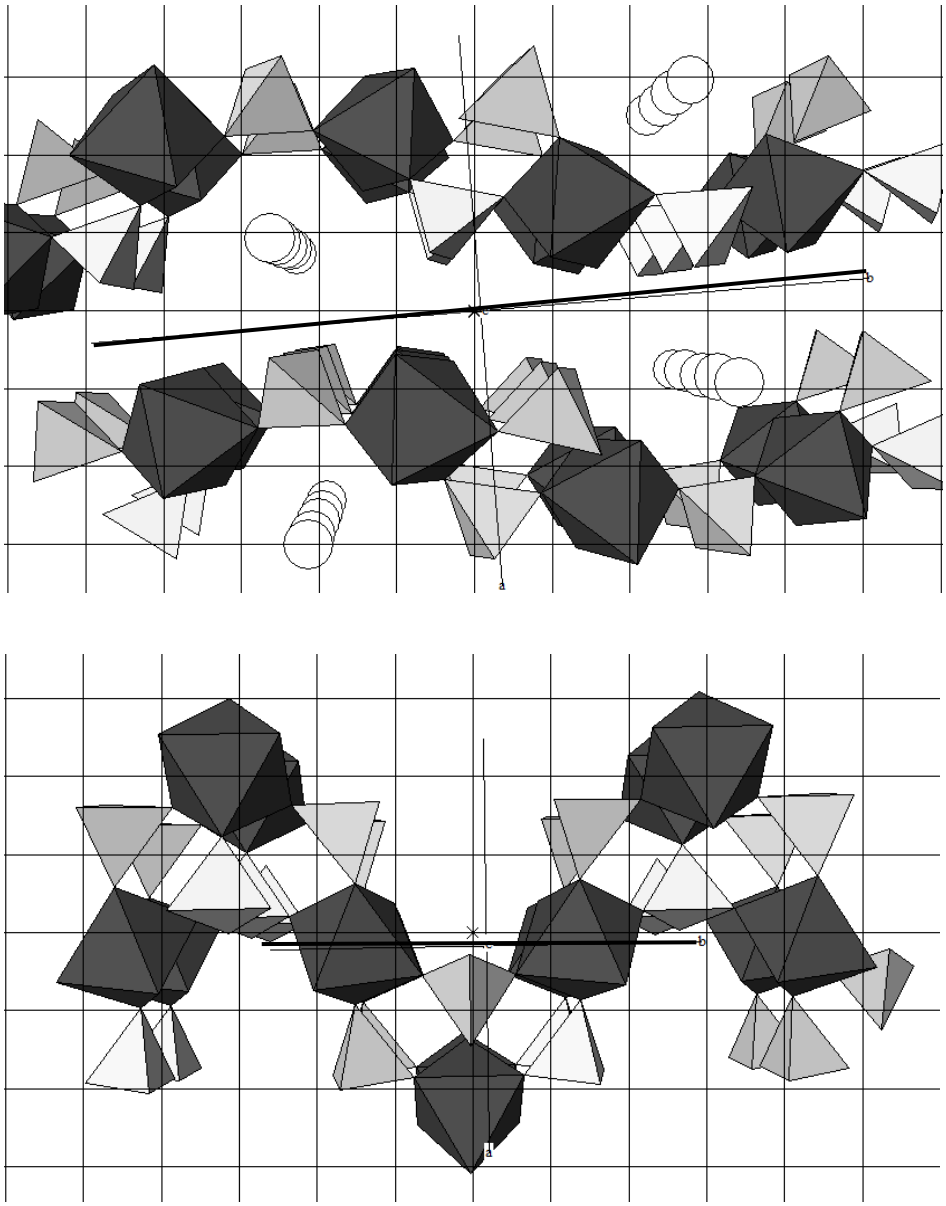

Figure 3.16: Looking down the c axes of kornelite (above) and pentahydrate (below) with a scale grid for reference (each square representing 2Å^2. The *b* axis is indicated by the bold line. It is clear from this image the constriction of the pentahydrate structure which occurs upon dehydration.

There is also a second possibility that could give rise to a hexahydrate with a different structure than that suggested by Robinson and Fang (1973). By considering the pentahydrate structure with the likely hydrogen bonds indicated, distinct channels become apparent (Figure 3.17). These channels are large and could hold a water molecule not bound to a polyhedron, which would result in a hexahydrate with a structure very similar to that of the pentahydrate. Majzlan et al. (2005) solved the crystal structure of the pentahydrate using powder X-ray diffraction, and did not determine hydrogen positions. It therefore remains uncertain whether the bond valence environment in the pentahydrate channels would be allow the free water molecule, but the geometry of the structure suggests that it may be possible (Figure 3.18).

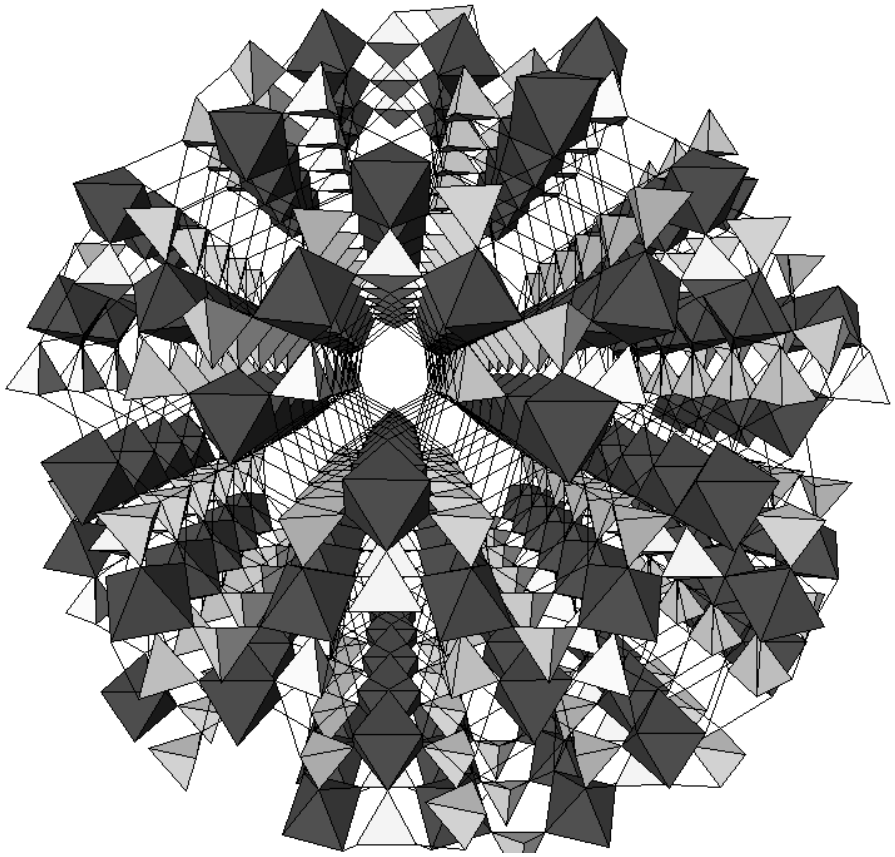

Figure 3.17: Pentahydrate structure showing predicted hydrogen bonds to a water molecule within the channel. This image is drawn looking down the *c* axis and bond lengths are in angstroms.

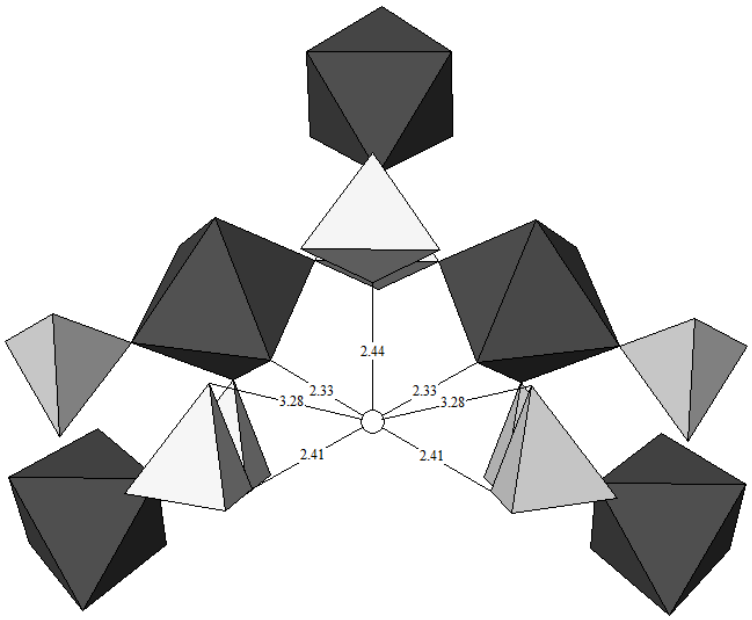

Figure 3.18: Pentahydrate channel showing a geometrically possible water site, as looking down the *c* axis, with hypothetical hydrogen bonds indicated.

It is also possible that the ferric sulfate hexahydrate which was seen by Posnjak and Merwin (1922) and Lausen (1928), could have had the same structural framework as the pentahydrate, but with a water molecule filling the open channels formed. The unit cell parameters of this hexahydrate would therefore be much closer to those of the pentahydrate. Figure 3.19 shows the pentahydrate structure viewed down the *b* axis. We can see that the addition of a water molecule could cause an expansion along the *c* axis as the structure accommodates the molecule.

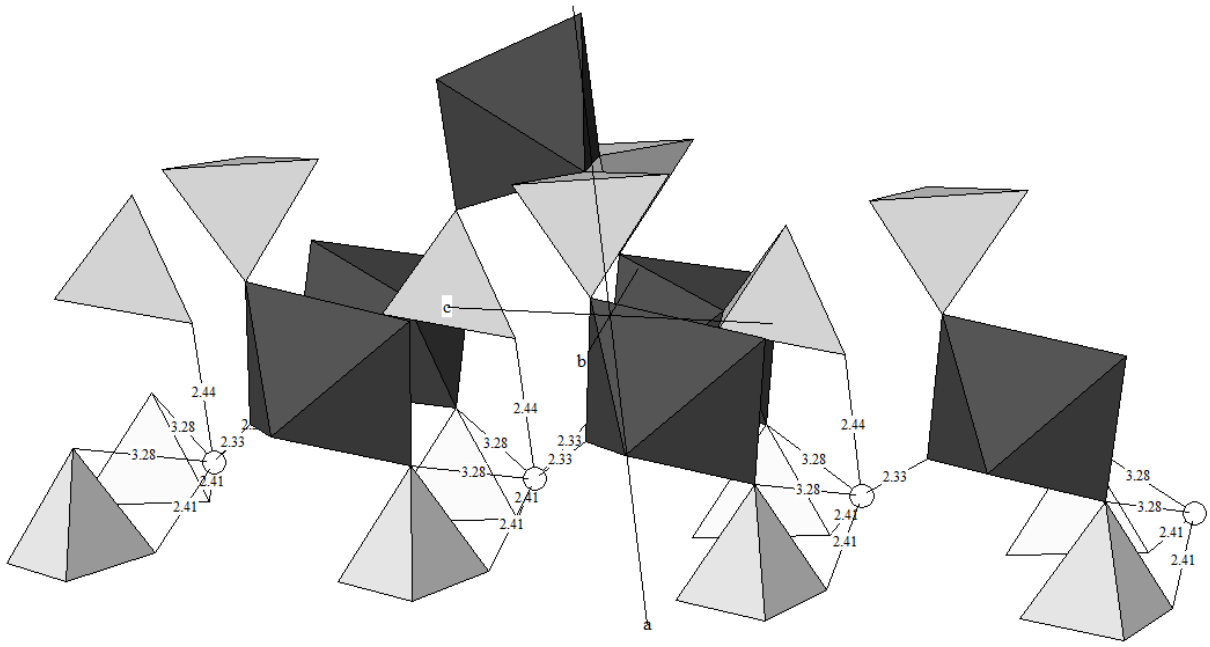

Figure 3.19: Pentahydrate structure with an additional water molecule indicated with possible bond lengths shown. The addition of this water could cause an expansion along the *c* axis as the structure accommodates that additional water molecule.

Likewise, we might expect an expansion along the *a* and *b* axes. It is evident that although the unit cell would have to expand to accommodate a sixth water molecule in the pentahydrate channels, it would be geometrically possible without breaking the restrictive bonds of the S1 tetrahedron indicated in Figure 2.11. The possible hydrogen bond lengths (Table 3.14) between the oxygen involved with the octahedra or the tetrahedra of the structure and the possible water location shown in Figure 3.18 are in the accepted range for O--H-O bonds found in other ferric sulfate species such as the hydrogen bonds found in kornelite (Table 2.18) by Robinson and Fang (1973).

Table 3.14: Hydrogen bond lengths between oxygen in the pentahydrate structure and a hypothetical water molecule not bound to a polyhedron. These are in good agreement with the hydrogen bonds found in other ferric sulfates, such as kornelite (Table 3.15).

O(A)		O*zw*	O(A)-zwO
O(1)	...	O*zw*	2.44 Å
O(3)	...	O*zw*	3.28
O(4)	...	O*zw*	2.41
O(8)	...	O*zw*	2.33

Table 3.15: Hydrogen bonds determined by Robinson and Fang (1973) for the mineral kornelite.

O(A)		Ow		O(b)	O(A)-Ow	Ow-O(B)
O(1)	...	Ow(1)	...	O(5)	2.673 Å	2.675 Å
O(4)	...	Ow(2)	...	O(4')	2.670	2.739
O(10)	...	Ow(3)	...	O(8)	2.822	2.567
O(2)	...	Ow(4)	...	Ow(7)	3.027	3.087
O(9)	...	Ow(5)	...	O(10)	2.780	2.650
O(7)	...	Ow(6)	...	O(9)	2.715	2.674
O(8)	...	Ow(7)	...	Ow(8)	2.869	2.864
O(5)	...	Ow(8)	...	Ow(4)	2.795	2.720

The two possible atomic structures discussed here (the kornelite structure without the additional free water and the pentahydrate with a trapped water molecule not bound to a polyhedron) are hypothetical. A single phase powder of the ferric sulfate hexahydrate has never been grown nor has a single crystal analysis ever been done, therefore the structure is unknown. In fact, as explained in the introduction, the existence of this member of the normal hydrous ferric sulfate system is, itself, suspect.

However, the predicted water content of the UK1 unit cell could suggest that the second hypothetical hexahydrate crystal structure presented here may be valid. It is possible that a water molecule could be contained in the channels of the pentahydrate 25% of the time (accounting for the extra 0.25 water in the pentahydrate structure). This additional water could bend and adjust the unit cell of the pentahydrate into the unit cell determined here, provided that this water was added systematically. It is also possible that this phase is a polymorph of the pentahydrate, having the same water content but different unit cell.

Unfortunately, without an atomic structure determination it is impossible to be sure of the nature of this UK1 phase. And without a single-phase powder or a large single crystal, an atomic structure determination is impossible. However, the unit cell presented here does offer a plausible configuration for UK1 that accounts for all the UK1 peaks.

However, regarding the mineral lausenite and whether or not it coincided with UK1 and what its hydration state might be, further experimentation still needed to be done. In order to further explore this aspect, the experiments of Posnjak and Merwin (1922) were recreated.

3.7 Posnjak and Merwin (1922) Experiments Recreated – An Introduction

On the 140°C and 110°C phase diagrams of Posnjak and Merwin's (1922) that at (Figure 3.1 and Figure 3.2), only one normal ferric sulfate (the hexahydrate) was observed. The material, described as hexahydrate, grown in these early experiments consisted of crystals large enough size to allow for refractive indices to be measured. An attempt was made to recreate those experiments done in 1922. This was done not only to allow for the collection of refractive indices data, but also with the expectation of obtaining a crystal large enough for single crystal X-ray diffraction and to resolve the debate about lausenite and its hydration state.

3.7.1 Experimental Method

In order to achieve maximum crystal yield, but also to remain within the appropriate percentages shown upon the Posnjak and Merwin (1922) ternary diagrams, several solutions were prepared. The solutions consisted of ferricopiapite or amorphous ferric sulfate *n*-hydrate, sulfuric acid and deionized water, which initially formed a cloudy precipitate. Table 3.16 shows the quantities used. Their ratios in relation to Fe_2O_3, SO_3 and H_2O can be seen in Figure 3.20 in reference to the Posnjak and Merwin (1922) 140°C diagram. These solutions were placed inside 1.0 ml. glass vials which were then sealed with an acetylene torch. The vials contained approximately 0.5 ml. of solution. The vials were then placed inside an oven heated to 130°C and left for between 7-10 days. When ready for analysis a vial was briefly cooled in air (for less than 3 minutes) and then opened. The liquid was sampled using a hypodermic needle and the solid material was removed and washed with anhydrous methanol in order to stop further reactions from taking place with the residual liquid. Half of the solid material was then placed on a glass slide and in diffraction pattern measured with an Panalytical X'pert Pro™ diffractometer equipped with a copper-target X-ray (λ = 1.5418 Å Cu Kα) tube operating at 40kV and 45mA. An incident slit of 1/4° with a 1/2° anti-scatter slit and 0.02 rad soller slits were used. A Ni filter was used, with an X'celerator™ position sensitive detector. Data were collected with an effective step size of 0.017° 2θ and an effective 25 second counting time over a 2θ range of 5°-55°, while the other half was immediately placed in Cargile oil (refractive index *n*=1.518) in order to minimize the risk of further reaction with remaining solution or air.

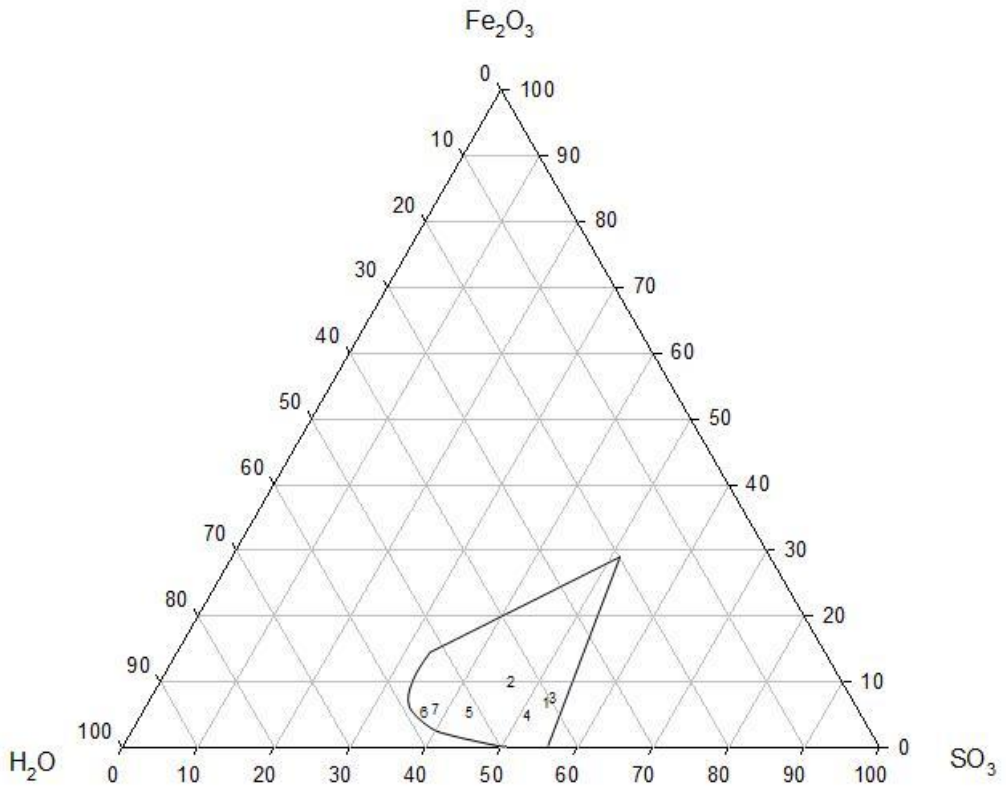

Figure 3.20: Selected samples demonstrated as percentages of Fe_2O_3, SO_3 and H_2O. The area outlined within the ternary is that which is shown on the 140°C Posnjak and Merwin (1922) diagram as the stability field of ferric sulfate hexahydrate .

Table 3.16: The amount of reagent used in the re-creation of the Posnjak and Merwin experiments of 1922. The solutions were placed in glass vials and sealed with an acetylene torch before being exposed to 130°C for between 7-10 days.

	1-15	2-15	3-15	5-15
Ferricopiapite	0.0786g	0.0950g	0.0654g	0.1049g
Water	0.2210g	0.2158g	0.2214g	0.2451g
Sulfuric acid	0.2145g	0.1926g	0.2115g	0.2138g

	6-15	7-15	8-15	10-15
Ferric sulfate *n*-hydrate	0.7490g	0.0883g	0.0994g	0.0888g
Water	0.2003g	0.2127g	0.2152g	0.1989g
Sulfuric acid	0.1806g	0.2064g	0.2254g	0.2014g

	1-26	2-26	3-26	4-26	5-26
Ferric sulfate n-hydrate	0.1143g	0.1553g	0.0987g	0.8670g	0.1075g
Water	0.1543g	0.1599g	0.1114g	0.1914g	0.2744g
Sulfuric acid	0.2941g	0.2003g	0.2206g	0.3275g	0.2922g

A crystal grain large enough to mount on a glass fiber was obtained from sample 3-15, and was placed on a spindle stage. Extinction measurements were taken using the monochromatic light from a sodium vapor lamp (λ=589.3nm). Using the computer program Excalibur (QuickWin V. 5.00, ©1998), the crystal was shown to have a 2V angle of 78.778°. Refractive indices were observed to be α = 1.604 β = 1.624 and γ = 1.658. These values are in good agreement with those reported by Posnjak and Merwin (1922) and Lausen (1928) (Table 3.17). Single crystal X-ray analysis was then performed on this mineral grain.

Table 3.17: Refractive indices of the phase identified as hexahydrate by Posnjak and Merwin (1922) and Lausen (1928) in comparison with synthetic pentahydrate (this study).

	Posnjak and Merwin (1922)	Lausen (1928)	Material created in this study
α	1.605	1.598	1.604
β	1.635	1.628	1.624
γ	1.657	1.654	1.658

The maximum extinction angle measured from the crystals grown in these experiments was 24° and fell within the range reported by Posnjak and Merwin (1922) of 22°-26°.

3.7.2 Results and Discussion

The solid materials analyzed through X-ray powder diffraction consistently were, in each case, the ferric sulfate pentahydrate ($Fe_2(SO_4)_3 \cdot 5H_2O$)(Figure 3.21). There was no indication of UK1 in any of the X-ray diffraction patterns generated from the material synthesized by these experiments.

The single crystal X-ray analysis likewise identified the phase as $Fe_2(SO_4)_3 \cdot 5H_2O$. The structure was, however, disordered and therefore unsuitable for the determination of hydrogen positions. The structure was also solved using different crystallographic settings (Table 3.18) but is the same unit cell determined by Majzlan (2005).

Table 3.18: The unit cell refined for this study of the material formed following the Posnjak and Merwin (1922) phase diagrams. Transformed, this cell is in excellent agreement with that of Majzlan's (2005) pentahydrate.

	This Study	Transformed	Majzlan (2005)
a-	5.5571	10.7146	10.711
b-	11.0721	11.0721	11.085
c-	10.7146	5.5571	5.5747
β-	98.888	98.888	98.853
volume			654Å
volume calculated	651.3Å^3	651.3Å^3	654.0Å^3

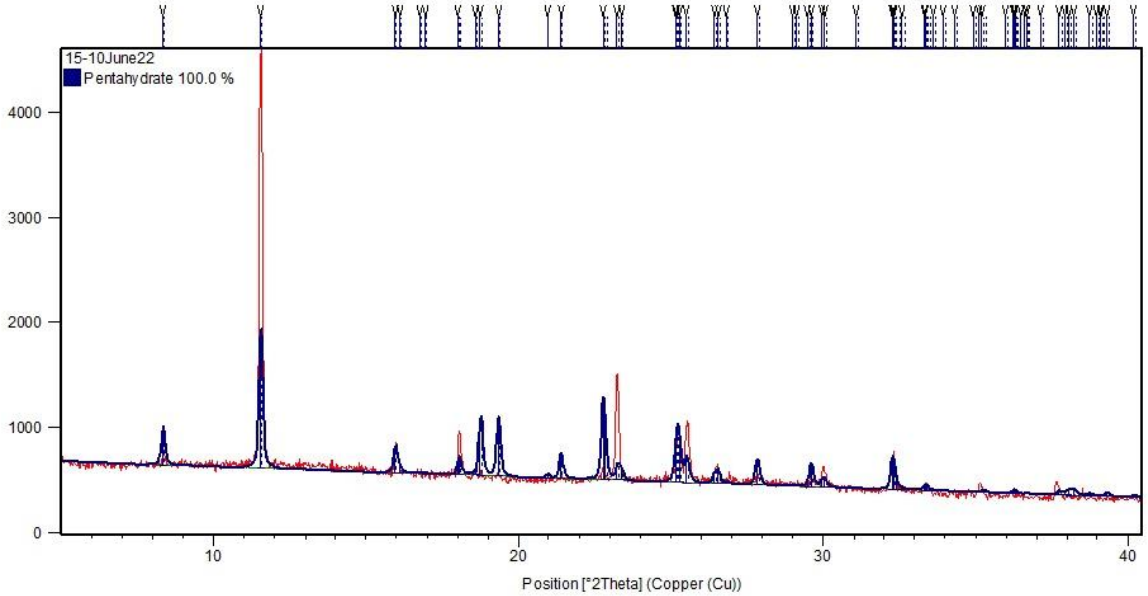

Figure 3.21: The X-ray diffraction pattern for the material grown in the Posnjak and Merwin (1922) recreations, from the same sample from which the single crystal used for single-crystal diffraction analysis was obtained. The blue calculated pattern is that of pentahydrate (Majzlan, 2010) and it corresponds well with the red pattern generated by the powder sample 15-10.

These results suggest that the material grown by Posnjak and Merwin (1922) and identified on their phase diagrams (Figure 3.1 and Figure 3.2) as $Fe_2(SO_4)_3 \cdot 6H_2O$, was incorrectly classified as a hexahydrate. The experiments performed here, using the compositional ranges as well as the experimental methods outlined in Posnjak and Merwin (1922), indicate a ferric sulfate pentahydrate. As the material analyzed by Posnjak and Merwin (1922) was likely the same as that found by Lausen (1928), based on refractive indice data, it is likely that the mineral lausenite is of formula $Fe_2(SO_4)_3 \cdot 5H_2O$; a pentahydrate.

3.8 Environmental Scanning Electron Microscope Study

The X-ray diffraction measurements indicated that there is a crystallographically distinct phase (UK1) that can form up to 70% of the volume of the sample. In order to obtain more information about this phase, and specifically to look at its crystal morphology, an Environmental Scanning Electron Microscope (ESEM) was used.

3.8.1 Experimental Method

A series of samples were analyzed using an FEI™ Scanning Electron Microscope. Uncoated samples were placed on carbon tape on aluminum plates. The samples consisted of varying amounts of UK1, rhomboclase, pentahydrate and, in some cases, kornelite, as determined by powder X-ray analysis. All were present as small crystallites. Percentages of the three or four minerals present in the mixed-phase samples were approximated based on Rietveld analysis. A single-phase kornelite sample and a single-phase pentahydrate were also examined for comparison of morphology when studying samples with mixed phases. The samples used are summarized in Table 3.18. Samples 1 and 2 were expected to show the largest percentage of UK1 while Sample 3 was dominated by pentahydrate. Sample 4 was kornelite and Sample 5 was pentahydrate.

Table 3.19: Mineral assemblage percentages estimated based on Rietveld analysis and peak intensities.

Sample	Pentahydrate	UK1	Kornelite	Rhomboclase
1	25	50	0	25
2	20	45	10	25
3	50	15	5	30
4	0	0	100	0
5	100	0	0	0

3.8.2 Results and Discussion

The results of the SEM analysis clearly showed a phase with a distinct morphology that does not match that of pentahydrate, kornelite or rhomboclase and is assumed to be UK1. The images of kornelite show the characteristic tabular, prismatic nature of this mineral. Kornelite is known to often form as a splay of the monoclinic prisms (Dana, 1951), but in this case individual crystals of kornelite can be seen quite clearly in the back-scattered SEM images shown in Figure 3.22.

In contrast, sample 5 consisting entirely of pentahydrate based on X-ray diffraction (Figure 3.23) exhibits a different morphology, being less blocky than the prisms of kornelite with a finer, more blade-like nature.

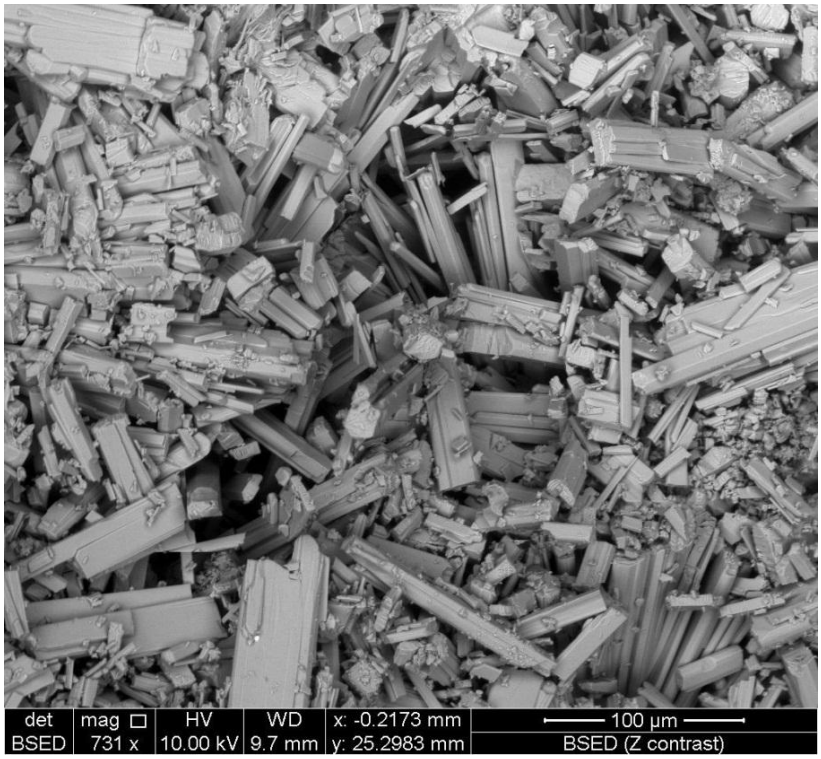

Figure 3.22: Sample 4 showing prismatic and blocky mineral grains of kornelite.

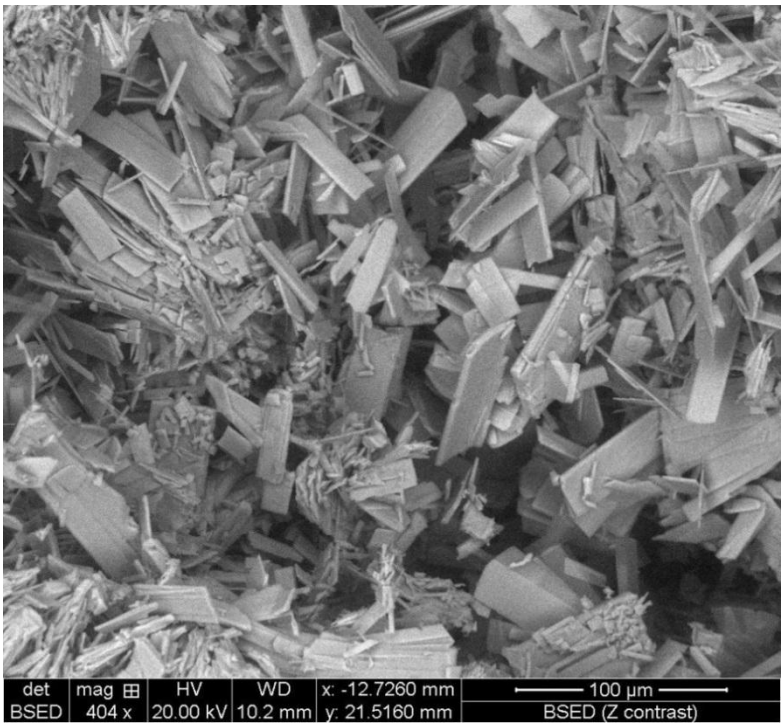

Figure 3.23: Sample 5 showing pentahydrate crystals with a fine, blade-like morphology.

Sample 1, which through XRD analysis was confirmed to be composed largely of UK1 and to have no kornelite in the mixture, contains a phase with a distinctly different morphology. The crystals are narrow, thin, and pointed (Figure 3.24), as opposed to the equant prisms of kornelite, and the flattened blades of pentahydrate. An image of the mixed-phase Sample 2 shows clearly the close association of pentahydrate and UK1 (Figure 3.25), and that they are a clearly distinct phases.

In addition to pentahydrate, Sample 2 had a large volume of rhomboclase (approximately 25%). Rhomboclase has perfect (001) cleavage and often forms as flat plates. Rhomboclase can be seen in Figure 3.25, as the large anhedral plates in the bottom right of the image.

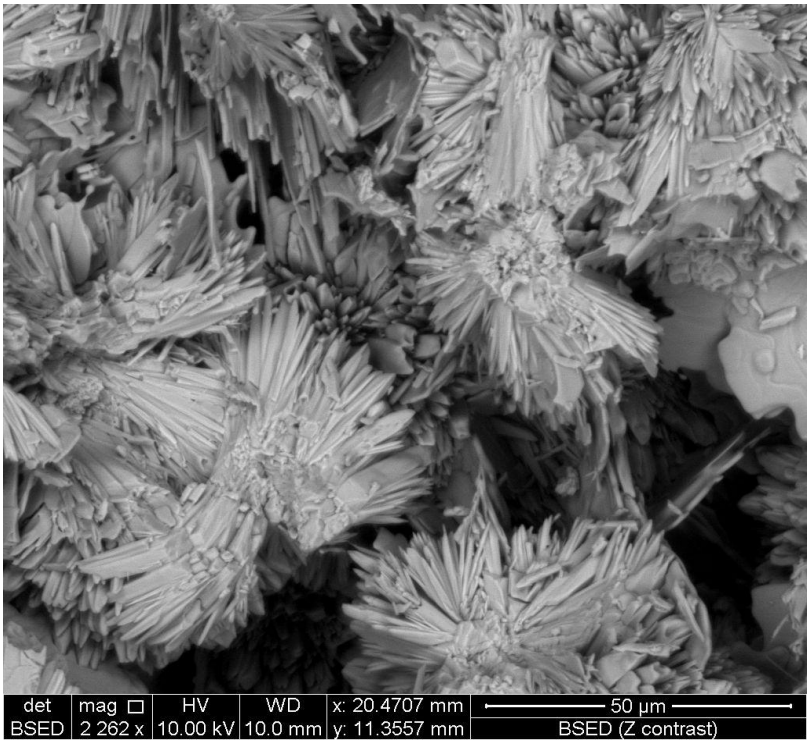

Figure 3.24: The Sample 1 showing flower-like blooms of UK1.

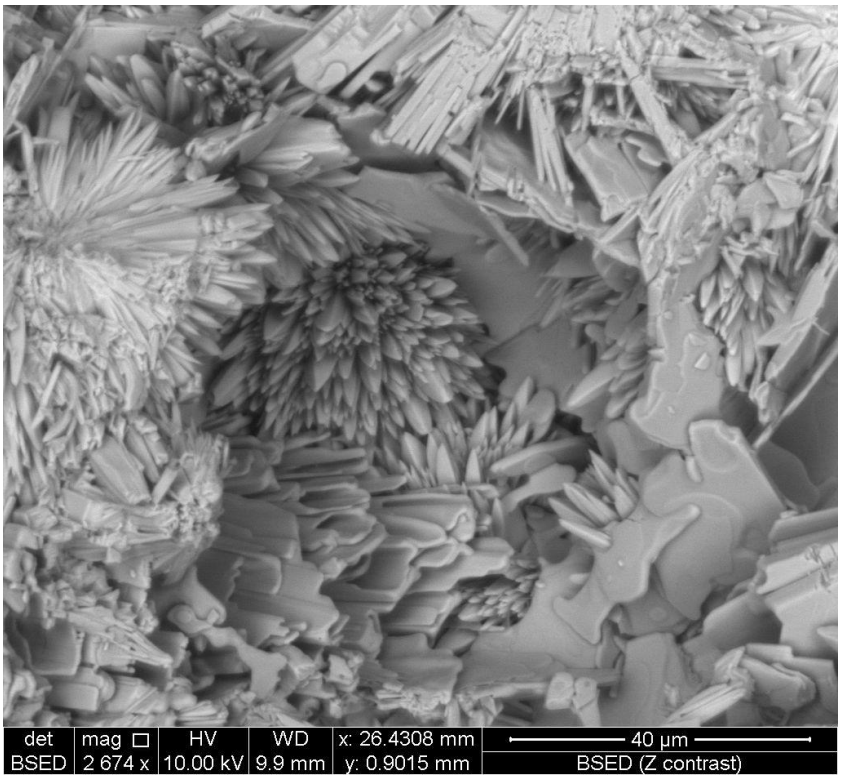

Figure 3.25: Back-scattered sample 1 the pointed nature of UK1 can be seen in the flower-like structure in center. In the bottom middle are the fine blades of pentahydrate and in the bottom right are plates of rhomboclase.

The images gathered with the ESEM show a crystal with a distinct morphology whose atomic structure, unfortunately, remains unknown. However, it is clear from these images that this phase grows in intimate association with other normal ferric sulfates in this system. To better quantify this phase in the future a single-phase powder or a large enough grain for single crystal X-ray analysis is required.

Chapter 4

Summary and Conclusion

4.1 Summary and Conclusion

Ferric sulfate minerals have long been known on Earth and, more recently, have been found on Mars (Jambor et al., 2000, Bishop et al., 2009). Their occurrence on Earth is often associated with mine waste environments where they contribute to the production of AMD, which presents an environmental threat to both aquatic and terrestrial ecosystems (Nordstrom et al.; 2000, Akcil and Koldas, 2006). Sulfate minerals also present a problem in other areas, such as the field of art conservation. Their occurrence on Mars represents an opportunity to investigate the history of water on that planet (Morris et al., 2006).

Wherever they are found, a thorough understanding of the mineralogy of ferric sulfates is necessary in order to optimize the human response. In the case of Earth, understanding the ferric sulfate minerals involved in the contamination of the environment is important if we are to mitigate these effects (Ling and Wang, 2009, Nordstrom et al., 2000). In the case of Mars, understanding the ferric sulfate minerals found on its surface is partly what will enable us to determine if life on that planet is, or was, possible (Yen et al, 2008). Unfortunately, there is still much that is unknown about the hydrous ferric sulfate system.

One aspect of hydrous ferric sulfates that was left undetermined by previous researchers was the hydrogen positions of several species, such as quenstedtite. The hydrogen positions of this mineral were determined and were presented here. An updated refinement of the mineral romerite was likewise presented here.

Another aspect of these minerals which is still not well understood is the phase relationships between the different phases at varying temperatures and relative humidities. This information is the key to building an understanding of the stability of the phases as well as the conditions under which they form. However, there is still uncertainty about the phases that even exist in the system, let alone their relationships. These phases need to be classified before a more thorough understanding of their phase relationships can be had.

One of the phases about which little has been known is in the sub-group of normal ferric sulfates. This phase was first synthesized and identified in 1922 as a normal ferric sulfate hexahydrate (Posnjak and Merwin, 1922). The mineral was soon after found in nature by Lausen (1928) and was named lausenite. After that, a period of nearly 80 years went by with no further exploration into the hexahdyrate until, in 2005, Majzlan et al. retrieved the type specimen of lausenite. Majzlan performed a study on the type specimen of lausenite and a synthesized phase, the results of which suggested that lausenite was actually a ferric sulfate pentahydrate. However, Ling and Wang (2009) found a hexahydrate and that lausenite did, in fact, have 6 water molecules in its structure. So, there remained some controversy.

To investigate this issue, the experiments conducted by Posnjak and Merwin (1922) were reproduced and the material resulting was analyzed. In the case of refractive indice measurements, the crystals grown were a match for those described by Posnjak and Merwin (1922) and by Lausen (1928).

The X-ray diffraction patterns for the solid material grown in these experiments were a perfect match for that generated by Majzlan (2005) and correspond to the mineral $Fe_2(SO_4)_3 \cdot 5H_2O$. The single crystal X-ray analysis also confirmed that the material grown was the ferric sulfate pentahydrate.

Therefore, the conclusion regarding the hexahydrate seen by Posnjak and Merwin (1922) and that found by Lausen (1928) is that the material was incorrectly classified as being $Fe_2(SO_4)_3 \cdot 6H_2O$ and was actually $Fe_2(SO_4)_3 \cdot 5H_2O$.

However, Ling and Wang (2009) had claimed to have identified an XRD pattern not explainable by any indexed mineral in the ferric sulfate system. This phase was further investigated as a part of this study. A series of experiments did demonstrate the existence of another unknown phase in the normal hydrous ferric sulfate system. This phase seemed to grow as an intermediate phase between and along with the minerals kornelite and pentahydrate at high temperature (~90°C) and low relative humidity (~23%). Attempts to grow a single-phase powder were unsuccessful, but a mixed phase powder was sent for synchrotron X-ray diffraction and a unit cell was identified. This unit cell had a unit cell volume more in keeping with a mineral formula of $Fe_2(SO_4)_3 \cdot 5.25H_2O$, than a hexahydrate. Looking at the crystal structure of the pentahydrate it is possible to see channels which could accommodate a free water molecule. Should a non-structurally bound water molecule, present only 25% of the time, work its way into these channels, the stretching of the pentahydrate unit cell could result in the unit cell observed here.

However, the possible existence of a second unknown phase in the mixture, as well as the possibility of peak overlap with the other phases present, means that there is still uncertainty about this unknown phase. Unless the phases are more clearly separated and/or a crystal grain large enough for single crystal X-ray analysis obtained, this uncertainty is likely to remain.

More work needs to be done to try and isolate the phases grown in this system so that accurate crystallographic measurements can be made. This information can then be applied in the field of environmental mineralogy or that of planetary mineralogy, both of which could benefit immensely from a more thorough understanding of the hydrous ferric sulfate system.

References

Ackermann, S., Biljana L., Armbrustrer,L., Doyle, S., Klaus-Dieter, G., and Majzlan, J. (2009). Thermodynamic and crystallographic properties of kornelite [$Fe_2(SO_4)_3$~$7.75H_2O$] and paracoquimbite [$Fe_2(SO_4)_3 \cdot 9H_2O$]. *Am. Mineral.* **94**, 1620-8.

Akcil, A., and Koldas, S. (2006). Acid mine drainage (AMD): Causes, treatment and case studies. *Journal of Cleaner Production* **14**, 1139-45.

Anderson, J.L., Peterson, R.C., Swainson, I. (2012). The atomic structure of deuterated boyleite $ZnSO_4 \cdot 4D_2O$ and Ilesite $MnSO_4 \cdot 4D_2O$ and Bianchite $ZnSO_4 \cdot 6H_2O$. *Am. Mineral.* (In press).

Bandy, M.C. (1938). Mineralogy of three sulphate deposits of northern Chile. *Am. Mineral.* **23**, 669-760.

Bigham, J. M. and Nordstrom, D.K. (2000). Iron and aluminum hydroxysulfates from acid sulfate waters. *Reviews in Mineralogy and Geochemistry* **40**, 351-403.

Bishop, J.L., Parente, M., Weitz, C.M., Dobrea, E., Roach, L.H., Murchie, S.L., McGuire, P.C. (2009). Mineralogy of juventae chasma: Sulfates in the light-toned mounds, mafic minerals in the bedrock, and hydrated silica and hydroxylated ferric sulfate on the plateau. *J.Geophys.Res.* **114**, E00D09.

Blaas, J. (1883). Uœber roemerit, botryogen und natrlichen magnesia-eisenvitriol. *Monatshefte fur Chemie. Chemical Monthly* **4**, 833-49.

Bloss D.F. (1980). The Spindle Stage. Cambridge University Press, New York.

Bond, P.L., Druschel, G.K., and Banfield, J.F. (2000). Comparison of acid mine drainage microbial communities in physically and geochemically distinct ecosystems. *Applied and Environmental Microbiology* **66**, 4962-71.

Brown, I.D. (1976). On the Geometry of O-H…O Hydrogen Bonds. *Acta Cryst*. **32**, 24-31

Bruker AXS. (2006). *APEX2*, *Version 2.0.* Bruker AXS Inc., Madison, Wisconsin, 53719 U.S.A.

Butler, G.M. (1928). In Corrections to volume 13. *Am. Mineral.* 13, 594.

Cesbron, F. (1964). Contribution a la Mineralogie des sulfates de fer hydrates. *Societe Francaise Mineralogie et de Cristallographie*. **E7**, 125-143.

Chandra, A. P., and Gerson, A.R. (2010). The mechanisms of pyrite oxidation and leaching: A fundamental perspective. *Surface Science Reports* **65**, 293-315.

Dana, J.D., Dana, E.S. (1951) Charles Palache, Harry Berman, and Clifford Frondel. 1944-9999. *System of mineralogy of james dwight dana and edward salisbury dana ... /*. 7th ed., 1951, entirely written and greatly enlarged ed. New York: John Wiley and sons, inc.

Fanfani, L., Nunzi, A. and Zanazzi, P.F. (1970). The crystal structure of romerite. *Am. Mineral.*, **55**, 78-89.

Fors, Y. and Sandström, M. (2006). Sulfur and iron in shipwrecks cause conservation concerns. *Chemical Society* Reviews **35**, 399-415.

Garcia, C., Ballester, A., Gonzalez, F., and Blazquez, M.L. (2005). Pyrite behaviour in a tailings pond. *Hydrometallurgy* **76**, 25-36.

Grailich, J. (1858). Der Roemerit, ein neues Mineral aus dem Rammelsberge. *Berichte der Akademie der Wissenschaften*, **28**, 272-288.

Greenspan, L. (1977). Humidity fixed points of binary saturated aqueous solutions. *Journal of Research - National Bureau of Standards. – Atmospheric Physics and Chemistry*. **81A**, 89–96.

Gunter, M.E., Downs, R.T., Bartelmehs, K.L., Evans, S.h., Pommier, C., Grow, J.S., Sanchez, M.S. and Bloss, F. (2005). Optic properties of centimeter-sized crystals determined in air with the spindle stage using EXCALIBRW. *Am. Mineral.* **90**, 1648-54.

Hammarstrom, J. M., Seal, R.R., Meier, A.L. and Kornfeld, J.M. (2005). Secondary sulfate minerals associated with acid drainage in the eastern US: Recycling of metals and acidity in surficial environments. *Chemical Geology* **215**, 407-31.

Hesketh, A. H., Broadhurst, J.L. and Harrison, S.T.L. (2010). Mitigating the generation of acid mine drainage from copper sulfide tailings impoundments in perpetuity: A case study for an integrated management strategy. *Minerals Engineering* **23**, 225-9.

HILL, D.W. (1969), Neutralization of Acid Mine Drainage. *Water Pollution Control Federation* **41**, 1702 - 1715

Hu, G., Dam-Johansen, K., Wedel, S. and Hansen, J.P. (2006). Decomposition and oxidation of pyrite. *Progress in Energy and Combustion Science* **32**, 295-314.

ICDD. (2006). PCPDFWIN. *International Centre for Diffraction Data.* Newtown Square, Pennsylvania, USA.

Jambor, J.L., Nordstrom, D.L. and Alpers, C.N. (2000). Metal-sulfate salts from sulfide mineral oxidation. *Reviews in Mineralogy and Geochemistry* **40**, 303-50.

Jerz, J.K. and Rimstidt, J.D. (2003). Efflorescent iron sulfate minerals: Paragenesis, relative stability, and environmental impact. *Am. Mineral.* **88**, 1919-32.

Kong, W.G., Wang, A. and Chou, I. (2011). Experimental determination of the phase boundary between kornelite and pentahydrated ferric sulfate at 0.1MPa. *Chemical Geology* **284**, 333-8.

Krenner, J.A. (1888) Ak. Magyar, Értes. **22**, 131.

Lausen, C. 1928. “Hydrous sulphates formed under fumerolic conditions at the United Verde mine”. *Am. Mineral.* **13**, 203-229.

Liang, H.C. and Thomson, B.M. (2010). Minerals and mine drainage. *Water Environment Research* **82**, 1485-533.

Lichtenberg, K.A., Arvidson, R.E., Morris, R.V., Murchie, S.L., Bishop, J.L., Remolar, D.F. and Glotch, T.D. (2010). Stratigraphy of hydrated sulfates in the sedimentary deposits of aram chaos, Mars. *Journal of Geophysical Research* **115**, E00D17.

Linck. (1889) Beitrlge zur Kenntniss der Sulfate von Tierra ammarilla bei Copiapo in Chile. Zeitschrift für Kristallographie. *Mineralogie und Petrographie*, Leipzig, **15**, 22.

Ling, Z. C., and Wang, A. (2009). Comparative spectroscopic study of three ferric sulfates: kornelite, lausenite and pentahydrate*. Lunar Planetary Science **40**: Abstract #1867.*

Ling, Z. C., and Wang, A. (2010). A Systematic spectroscopic Study of Eight Hydrous Ferric Sulfates Relevant to Mars. *Icarus* **209.2**, 422-33.

Lottermoser, B.G. (2007). *Sulfidic mine wastes*. Mine wastes. Springer Berlin Heidelberg.

Majzlan, J., Botez, C. and Stephens, P.R. (2005). The crystal structures of synthetics $Fe_2(SO_4)_3(H_2O)_5$ and the type specimen of lausenite. *Am. Mineral.* **90**, 411-6.

Marion, G. M., Kargel, J.S. and Catling, D.C. (2008). Modeling ferrous-ferric iron chemistry with application to martian surface geochemistry. *Geochimica Et Cosmochimica Acta* **72,** 242-66.

Mereiter, K. (1974). Die Kristallstruktur von Rhomboklas $(H_5O_2)^+(Fe(SO_4)_2(H_2O)_2)$. *Tschermaks Mineralogische und Petrographische Mitteilungen* **21**, 216–232.

Molson, J. W., Fala, O., Aubertin, M. and Bussiere, B. (2005). Numerical simulations of pyrite oxidation and acid mine drainage in unsaturated waste rock piles. *Journal of Contaminant Hydrology* **78**, 343-71.

Montero S., Brimhall, G.H., Alpers, C.N. and Swayze, G.H. (2005). Characterization of waste rock associated with acid drainage at the penn mine, California, by ground-based visible to short-wave infrared reflectance spectroscopy assisted by digital mapping. *Chemical Geology* **215**, 453-72.

Morris, R. V., Klingelhöfer, G., Schröder, C., Rodionov, D.S., Yen, A., Ming, D.W., de Souza, P. A. (2006). Mössbauer mineralogy of rock, soil, and dust at meridiani planum, Mars: Opportunity's journey across sulfate-rich outcrop, basaltic sand and dust, and hematite lag deposits. *Journal of Geophysical Research* **111**, E12S15.

Natarajan, K. A. (2008). Microbial aspects of acid mine drainage and its bioremediation. *Transactions of Nonferrous Metals Society of China* **18**, 1352-60.

Newman, A. (1998). Pyrite Oxidation and Museum Collections: A review of theory and conservation treatments. *The Geological Curator* **6**, 363-372

Nordstrom, D.K. and Alpers, C.N. (1999). Negative pH, efflorescent mineralogy, and consequences for environmental restoration at the Iron Mountain Superfund site, California. *Presented at National Academy of Sciences colloquium ''Geology, Mineralogy, and Human Welfare,''* held November 8–9, 1998

Nordstrom, D.K., Alpers, C.N., Ptacek, C.J. and Blowes, D.W. (2000). Negative pH and extremely acidic mine waters from Iron Mountain, California. *Environmental Science & Technology* **34**, 254-8.

Oddy, W. A. (1977). The conservation of pyritic stone antiquities. *Studies in Conservation* **22**, 68-72.

Posnjak, E. and Merwin, H.E. 1922. The system, Fe_2O_3-SO_3-H_2O. *Journal of the American Chemical Society* **44**, 1965-1994.

Robinson, P.D. and Fang, J.H. (1973). The crystal structure and mineral chemistry of hydrated ferric sulfates. III. The crystal structure of kornelite. *Am. Mineral.* **58**, 535-539.

Sabelli, C. and Trosti-Ferroni, R. (1985). A structural classification of sulfate minerals. *Periodico di Mineralogia* **5.4**, 1-46.

Scott, D.A. and Eggert, G. (1948). Iron and steel in art : Corrosion, colorants, conservation. Archetype Publishing Inc. London

Sefton-Nash, E. and Catling, D.C. (2008). Hematitic concretions at meridiani planum, Mars: Their growth timescale and possible relationship with iron sulfates. *Earth and Planetary Science Letters* **269**, 365-75.

Smith, G.S. and Snyder, R.L. (1979). A criterion for rating powder diffraction patterns and evaluating the reliability of powder-pattern indexing. *Journal of Applied Crystallography.* **12**, 60-65.

Stumm, W. and Lee, F.G. Oxygenation of Ferrous Iron. *Industrial & Engineering Chemistry* **53**, 143-146.

Susse P. (1971). Kristallchemie und Klassifikation der Naturlichen Ferrisulphate. *Fortschr Mineral*. **49**, 119-121.

Synchrotron Diffraction. *International Diffraction Data Database- Tutorials*. Accessed August 14, 2012. <http://www.icdd.com/resources/tutorials/pdf/Synchrotron%20Diffraction.pdf>

Thomas, J. N., Robinson, P.D., and Fang, J.H. (1974). The crystal structure and mineral chemistry of hydrated ferric sulphates. IV. The crystal structure of quenstedtite. *Am. Mineral.* **59**, 582-586.

Ungemach, H. (1935). Sur certains mineraux sulfates du Chili. *Bulletin de la Societe Chimique de France* **58**, 160-165.

Valente, T.M. and Gomes, C.L. (2009). Occurrence, properties and pollution potential of environmental minerals in acid mine drainage. *Science of the Total Environment* **407**, 1135-52.

Visser, J. W. (1969). A fully automatic program for finding the unit cell from powder data. *Journal of Applied Crystallography* **2**, 89-95.

Wang, A., Bell, J.F., Li, R., Johnson, J.R., Farrand, W.H., Cloutis, E.A., Arvidson, R.E. (2008). Light-toned salty soils and coexisting si-rich species discovered by the Mars exploration rover spirit in Columbia hills. *Journal of Geophysical Research* **113**, E12S40.

Wolfe, C. W. (1937). Re-orientation of roemerite. *Am. Mineral.* **22**, 736-741.

Xu, W. and Parise, J. (2011). Temperature and humidity effects on ferric sulfate stability and phase transformation. *Am. Mineral.* **97**, 378-83.

Xu, W., Tosca, N.J., McLennan, S.M. and Parise, J. (2009). Humidity-induced phase transitions of ferric sulfate minerals studied by in situ and ex situ X-ray diffraction. *Am. Mineral.* **94**, 1629-37.

Yen, A. S., Morris, R.V., Clark, B.C., Gellert, R., Knudson, A.T., Squyres, S. and Mittlefehldt, D.W. (2008). Hydrothermal processes at gusev crater: An evaluation of paso robles class soils. *Journal of Geophysical Research* **113**, E06S10.

Yerrapragada, S.S. and Chirra, S.R. (1996). Weathering rates of marble in laboratory and outdoor conditions. *Journal of Environmental Engineering* **122**, 856.

Appendix A – Unit Cell Refinement

Measurement Conditions: (Bookmark 1)

Dataset Name	HS1
File name	C:\Users\User\Documents\Queen's\Masters\Thesis\XRD Data\Synchrotron\HS1.asc
Raw Data Origin	ASCII-2Theta-Intensity (.ASC)
Scan Axis	Gonio
Start Position [°2Th.]	0.5000
End Position [°2Th.]	49.9910
Step Size [°2Th.]	0.0010
Scan Step Time [s]	1.0000
Offset [°2Th.]	0.0000
Divergence Slit Type	Fixed
Divergence Slit Size [°]	1.0000
Specimen Length [mm]	10.00
Receiving Slit Size [mm]	0.1000
Measurement Temperature [°C]	25.00
Anode Material	Cu
K-Alpha1 [Å]	0.41308
Generator Settings	0 mA, 0 kV
Diffractometer Number	0
Goniometer Radius [mm]	240.00
Dist. Focus-Diverg. Slit [mm]	91.00
Incident Beam Monochromator	No
Spinning	No

Main Graphics, Analyze View: (Bookmark 2)

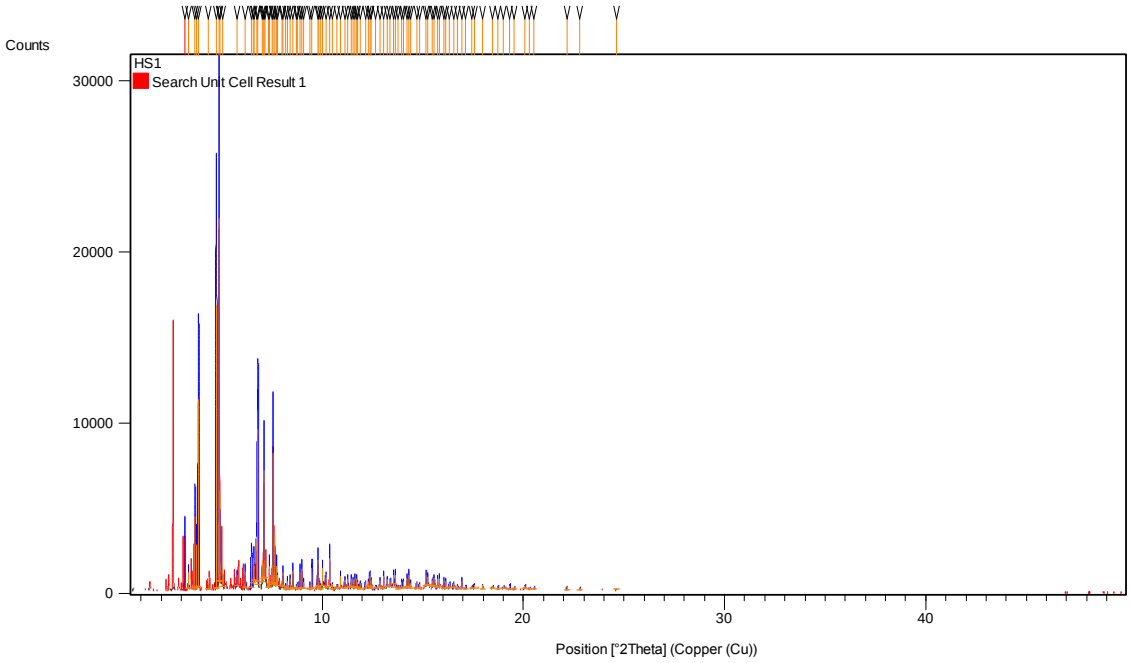

Peak List: (Bookmark 3)

Pos. [°2Th.]	Height [cts]	FWHM [°2Th.]	d-spacing [Å]	Rel. Int. [%]
3.1638	2997.40	0.0109	7.48182	14.12
3.3636	945.24	0.0109	7.03739	4.45
3.6822	4240.84	0.0694	6.42864	19.98
3.7709	2506.87	0.0082	6.27757	11.81
3.8600	10966.66	0.0694	6.13267	51.66
4.3402	374.40	0.0084	5.45447	1.76
4.7325	945.08	0.0694	5.00253	4.45
4.7360	16576.93	0.0694	4.99883	78.09
4.8863	21226.76	0.0082	4.84520	100.00
4.9218	5295.00	0.0142	4.81020	24.94
5.0578	1021.93	0.0139	4.68100	4.81
5.7514	673.08	0.0082	4.11689	3.17
6.1849	941.04	0.0070	3.82856	4.43

6.4827	1801.55	0.0694	3.65285	8.49
6.5851	1468.71	0.0694	3.59610	6.92
6.6208	855.53	0.0155	3.57676	4.03
6.7503	2359.98	0.0694	3.50822	11.12
6.8113	9105.04	0.0694	3.47681	42.89
7.0240	1285.23	0.0184	3.37167	6.05
7.0709	880.25	0.0273	3.34932	4.15
7.1006	6295.04	0.0109	3.33534	29.66
7.1332	991.00	0.0241	3.32012	4.67
7.3495	519.36	0.0222	3.22251	2.45
7.3686	1246.61	0.0083	3.21420	5.87
7.5184	1136.82	0.0197	3.15025	5.36
7.5460	7626.91	0.0082	3.13874	35.93
7.6444	2869.31	0.0128	3.09840	13.52
7.6446	2484.56	0.0083	3.09832	11.70
7.7255	621.40	0.0372	3.06592	2.93
7.7493	1152.50	0.0100	3.05653	5.43
7.7862	628.69	0.0127	3.04205	2.96
8.0221	348.26	0.0121	2.95273	1.64
8.0417	855.72	0.0083	2.94554	4.03
8.1837	221.04	0.0200	2.89453	1.04
8.2653	513.34	0.0100	2.86599	2.42
8.3883	604.17	0.0100	2.82404	2.85
8.5423	1013.42	0.0083	2.77323	4.77
8.7120	218.42	0.0167	2.71930	1.03
8.7818	277.84	0.0233	2.69773	1.31
8.8903	958.10	0.0100	2.66486	4.51
8.9921	1178.33	0.0150	2.63476	5.55
9.0647	383.23	0.0133	2.61372	1.81

9.3877	269.74	0.0133	2.52396	1.27
9.4743	968.98	0.0083	2.50094	4.56
9.4987	1204.03	0.0117	2.49453	5.67
9.7780	1560.52	0.0150	2.42345	7.35
9.8533	368.19	0.0133	2.40498	1.73
9.9239	223.12	0.0133	2.38790	1.05
10.0223	1046.21	0.0117	2.36453	4.93
10.1735	613.43	0.0167	2.32948	2.89
10.3723	1704.85	0.0117	2.28495	8.03
10.5129	293.66	0.0200	2.25447	1.38
10.7457	180.14	0.0267	2.20577	0.85
10.9144	649.42	0.0117	2.17176	3.06
11.1145	444.84	0.0167	2.13280	2.10
11.2706	531.88	0.0233	2.10335	2.51
11.4456	486.73	0.0133	2.07128	2.29
11.5202	377.84	0.0333	2.05793	1.78
11.6168	533.58	0.0083	2.04087	2.51
11.6964	525.59	0.0200	2.02703	2.48
11.7669	358.79	0.0200	2.01493	1.69
11.9079	328.11	0.0133	1.99115	1.55
12.1414	338.06	0.0200	1.95300	1.59
12.2922	348.34	0.0167	1.92912	1.64
12.3625	615.79	0.0200	1.91819	2.90
12.4343	451.63	0.0200	1.90717	2.13
12.6526	187.73	0.0533	1.87439	0.88
12.8696	387.74	0.0333	1.84291	1.83
13.0496	736.28	0.0183	1.81760	3.47
13.2254	421.43	0.0167	1.79354	1.99
13.3796	347.69	0.0533	1.77297	1.64

13.5498	545.71	0.0267	1.75080	2.57
13.6460	731.03	0.0100	1.73851	3.44
13.7781	203.78	0.0333	1.72192	0.96
13.9397	338.72	0.0267	1.70206	1.60
14.0173	357.55	0.0167	1.69269	1.68
14.2307	547.51	0.0167	1.66743	2.58
14.2944	705.50	0.0133	1.66003	3.32
14.3918	311.05	0.0133	1.64886	1.47
14.6931	297.12	0.0333	1.61523	1.40
14.8257	272.16	0.0267	1.60086	1.28
15.1728	633.62	0.0200	1.56445	2.98
15.2432	486.74	0.0267	1.55726	2.29
15.4891	360.71	0.0267	1.53269	1.70
15.5702	465.27	0.0167	1.52475	2.19
15.7398	510.48	0.0167	1.50843	2.40
15.8259	495.47	0.0133	1.50027	2.33
16.0376	467.18	0.0167	1.48060	2.20
16.1248	438.16	0.0233	1.47264	2.06
16.3215	252.02	0.0667	1.45501	1.19
16.5196	231.24	0.0667	1.43768	1.09
16.7179	177.01	0.0400	1.42075	0.83
16.9298	418.13	0.0167	1.40309	1.97
17.1318	199.69	0.0400	1.38667	0.94
17.4411	156.89	0.0533	1.36226	0.74
17.5531	231.77	0.0267	1.35364	1.09
17.9712	223.27	0.0267	1.32240	1.05
18.4713	144.12	0.0800	1.28689	0.68
18.7493	157.90	0.0533	1.26798	0.74
18.9983	153.82	0.0800	1.25151	0.72

19.3308	205.44	0.0533	1.23018	0.97
19.5477	110.53	0.1333	1.21666	0.52
20.0815	157.42	0.0667	1.18464	0.74
20.2837	100.22	0.0800	1.17295	0.47
20.5364	111.47	0.0533	1.15867	0.53
22.1585	162.99	0.0333	1.07480	0.77
22.8111	138.90	0.0400	1.04444	0.65
24.6274	71.99	0.0533	0.96847	0.34

Appendix B – Romerite CIF

```
data_romerite

_audit_creation_method            SHELXL-97
_chemical_name_systematic
;
 ?
;
_chemical_name_common             ?
_chemical_melting_point           ?
_chemical_formula_moiety          ?
_chemical_formula_sum
 'Fe3 H28 O30 S4'
_chemical_formula_weight          804.01

loop_
 _atom_type_symbol
 _atom_type_description
 _atom_type_scat_dispersion_real
 _atom_type_scat_dispersion_imag
 _atom_type_scat_source
 'Fe'  'Fe'   0.3463   0.8444
 'International Tables Vol C Tables 4.2.6.8 and 6.1.1.4'
 'H'  'H'   0.0000   0.0000
 'International Tables Vol C Tables 4.2.6.8 and 6.1.1.4'
 'O'  'O'   0.0106   0.0060
```

```
 'International Tables Vol C Tables 4.2.6.8 and 6.1.1.4'
 'S'  'S'   0.1246   0.1234
 'International Tables Vol C Tables 4.2.6.8 and 6.1.1.4'

_symmetry_cell_setting            Triclinic
_symmetry_space_group_name_H-M    P-1

loop_
 _symmetry_equiv_pos_as_xyz
 'x, y, z'
 '-x, -y, -z'

_cell_length_a                    6.4274(3)
_cell_length_b                    15.2490(7)
_cell_length_c                    6.3464(3)
_cell_angle_alpha                 89.72
_cell_angle_beta                  100.79
_cell_angle_gamma                 85.96
_cell_volume                      609.40(5)
_cell_formula_units_Z             1
_cell_measurement_temperature     180(2)
_cell_measurement_reflns_used     4939
_cell_measurement_theta_min       2.68
_cell_measurement_theta_max       28.00

_exptl_crystal_description        plate
_exptl_crystal_colour             colourless
_exptl_crystal_size_max           0.25
```

```
_exptl_crystal_size_mid          0.15
_exptl_crystal_size_min          0.08
_exptl_crystal_density_meas      ?
_exptl_crystal_density_diffrn    2.191
_exptl_crystal_density_method    'not measured'
_exptl_crystal_F_000             410
_exptl_absorpt_coefficient_mu    2.230
_exptl_absorpt_correction_type   multi-scan
_exptl_absorpt_correction_T_min  0.6056
_exptl_absorpt_correction_T_max  0.8418
_exptl_absorpt_process_details   ?

_exptl_special_details
;
 ?
;

_diffrn_ambient_temperature      180(2)
_diffrn_radiation_wavelength     0.71073
_diffrn_radiation_type           MoK\a
_diffrn_radiation_source         'fine-focus sealed tube'
_diffrn_radiation_monochromator  graphite
_diffrn_measurement_device_type  'CCD area detector'
_diffrn_measurement_method       'phi and omega scans'
_diffrn_detector_area_resol_mean ?
_diffrn_standards_number         ?
_diffrn_standards_interval_count ?
_diffrn_standards_interval_time  ?
```

```
_diffrn_standards_decay_%        ?
_diffrn_reflns_number            5995
_diffrn_reflns_av_R_equivalents  0.0146
_diffrn_reflns_av_sigmaI/netI    0.0159
_diffrn_reflns_limit_h_min       -7
_diffrn_reflns_limit_h_max       7
_diffrn_reflns_limit_k_min       -18
_diffrn_reflns_limit_k_max       18
_diffrn_reflns_limit_l_min       -7
_diffrn_reflns_limit_l_max       7
_diffrn_reflns_theta_min         2.68
_diffrn_reflns_theta_max         26.00
_reflns_number_total             2370
_reflns_number_gt                2274
_reflns_threshold_expression     >2sigma(I)

_computing_data_collection       'Bruker SMART'
_computing_cell_refinement       'Bruker SMART'
_computing_data_reduction        'Bruker SAINT'
_computing_structure_solution    'SHELXS-97 (Sheldrick, 1990)'
_computing_structure_refinement  'SHELXL-97 (Sheldrick, 1997)'
_computing_molecular_graphics    'Bruker SHELXTL'
_computing_publication_material  'Bruker SHELXTL'

_refine_special_details
;
 Refinement of F^2^ against ALL reflections.  The weighted R-factor wR and
 goodness of fit S are based on F^2^, conventional R-factors R are based
```

```
 on F, with F set to zero for negative F^2^. The threshold expression of
 F^2^ > 2sigma(F^2^) is used only for calculating R-factors(gt) etc. and is
 not relevant to the choice of reflections for refinement.  R-factors based
 on F^2^ are statistically about twice as large as those based on F, and R-
 factors based on ALL data will be even larger.
;

_refine_ls_structure_factor_coef  Fsqd
_refine_ls_matrix_type            full
_refine_ls_weighting_scheme       calc
_refine_ls_weighting_details
 'calc w=1/[\s^2^(Fo^2^)+(0.0313P)^2^+0.4836P] where P=(Fo^2^+2Fc^2^)/3'
_atom_sites_solution_primary      direct
_atom_sites_solution_secondary    difmap
_atom_sites_solution_hydrogens    geom
_refine_ls_hydrogen_treatment     mixed
_refine_ls_extinction_method      none
_refine_ls_extinction_coef        ?
_refine_ls_number_reflns          2370
_refine_ls_number_parameters      229
_refine_ls_number_restraints      13
_refine_ls_R_factor_all           0.0207
_refine_ls_R_factor_gt            0.0199
_refine_ls_wR_factor_ref          0.0551
_refine_ls_wR_factor_gt           0.0546
_refine_ls_goodness_of_fit_ref    1.043
_refine_ls_restrained_S_all       1.040
_refine_ls_shift/su_max           0.001
```

```
_refine_ls_shift/su_mean          0.000


loop_
 _atom_site_label
 _atom_site_type_symbol
 _atom_site_fract_x
 _atom_site_fract_y
 _atom_site_fract_z
 _atom_site_U_iso_or_equiv
 _atom_site_adp_type
 _atom_site_occupancy
 _atom_site_symmetry_multiplicity
 _atom_site_calc_flag
 _atom_site_refinement_flags
 _atom_site_disorder_assembly
 _atom_site_disorder_group
Fe1 Fe 0.0000 0.0000 0.0000 0.01587(10) Uani 1 2 d S . .
Fe2 Fe 0.34140(4) 0.319699(15) 0.59698(4) 0.01105(8) Uani 1 1 d . . .
S1 S 0.59524(7) 0.16739(3) 0.36522(7) 0.01259(10) Uani 1 1 d . . .
S2 S 0.76279(6) 0.38635(3) 0.90830(6) 0.01160(10) Uani 1 1 d . . .
O1 O 0.4336(2) 0.20732(8) 0.4864(2) 0.0174(3) Uani 1 1 d . . .
O1W O 0.2460(3) 0.05136(12) -0.1321(4) 0.0413(5) Uani 1 1 d D . .
H1 H 0.318(5) 0.0230(19) -0.189(5) 0.057(10) Uiso 1 1 d D . .
H2A H 0.309(8) 0.055(5) -0.018(5) 0.059(16) Uiso 0.49(6) 1 d PD A 1
H2B H 0.272(10) 0.0984(16) -0.148(11) 0.059(16) Uiso 0.51(6) 1 d PD A 2
O2 O 0.5859(2) 0.21936(9) 0.1676(2) 0.0223(3) Uani 1 1 d . . .
O2W O 0.1134(3) 0.04888(12) 0.3090(3) 0.0314(4) Uani 1 1 d D . .
H3 H 0.230(3) 0.057(2) 0.345(5) 0.050(9) Uiso 1 1 d D . .
```

```
H4 H 0.055(5) 0.074(2) 0.385(5) 0.054(10) Uiso 1 1 d D . .
O3 O 0.8095(2) 0.16942(9) 0.4974(2) 0.0180(3) Uani 1 1 d . . .
O3W O 0.1803(3) -0.11695(12) 0.0906(3) 0.0400(5) Uani 1 1 d . . .
H5 H 0.184(5) -0.1354(19) 0.200(5) 0.039(8) Uiso 1 1 d . . .
H6 H 0.229(5) -0.152(2) 0.021(5) 0.048(9) Uiso 1 1 d . . .
O4 O 0.5411(2) 0.07728(9) 0.3218(2) 0.0244(3) Uani 1 1 d . . .
O4W O 0.2598(2) 0.25391(9) 0.8459(2) 0.0176(3) Uani 1 1 d . . .
H7 H 0.357(5) 0.2402(19) 0.951(5) 0.042(8) Uiso 1 1 d . . .
H8 H 0.166(5) 0.2742(19) 0.883(5) 0.034(8) Uiso 1 1 d . . .
O5 O 0.6269(2) 0.32843(9) 0.7588(2) 0.0193(3) Uani 1 1 d . . .
O5W O 0.0364(2) 0.30840(10) 0.4459(2) 0.0158(3) Uani 1 1 d . . .
H9 H -0.022(4) 0.2722(19) 0.471(4) 0.028(7) Uiso 1 1 d . . .
H10 H 0.011(4) 0.3184(16) 0.313(5) 0.027(6) Uiso 1 1 d . . .
O6 O 0.6421(2) 0.42223(9) 1.0656(2) 0.0182(3) Uani 1 1 d . . .
O6W O 0.2231(2) 0.43517(9) 0.7000(2) 0.0182(3) Uani 1 1 d . . .
H11 H 0.279(5) 0.468(2) 0.768(5) 0.041(9) Uiso 1 1 d . . .
H12 H 0.092(5) 0.4397(19) 0.719(5) 0.043(8) Uiso 1 1 d . . .
O7 O 0.8276(2) 0.45676(9) 0.7805(2) 0.0197(3) Uani 1 1 d . . .
O7W O 0.3824(2) 0.38805(10) 0.3390(2) 0.0194(3) Uani 1 1 d . . .
H13 H 0.331(5) 0.434(2) 0.309(5) 0.048(9) Uiso 1 1 d . . .
H14 H 0.473(5) 0.3802(18) 0.268(5) 0.034(7) Uiso 1 1 d . . .
O8 O 0.9504(2) 0.33113(9) 1.0139(2) 0.0165(3) Uani 1 1 d . . .

loop_
 _atom_site_aniso_label
 _atom_site_aniso_U_11
 _atom_site_aniso_U_22
 _atom_site_aniso_U_33
```

```
 _atom_site_aniso_U_23
 _atom_site_aniso_U_13
 _atom_site_aniso_U_12
Fe1 0.0160(2) 0.01614(19) 0.01516(18) -0.00085(14) 0.00317(14) 0.00176(14)
Fe2 0.00953(14) 0.01271(14) 0.01092(13) -0.00079(9) 0.00214(10) -0.00018(9)
S1 0.0114(2) 0.0140(2) 0.0124(2) -0.00117(15) 0.00286(16) 0.00053(16)
S2 0.0090(2) 0.0132(2) 0.0124(2) -0.00071(15) 0.00219(16) 0.00024(16)
O1 0.0170(6) 0.0162(6) 0.0208(7) -0.0048(5) 0.0085(5) 0.0000(5)
O1W 0.0403(10) 0.0286(9) 0.0672(14) -0.0222(9) 0.0369(10) -0.0127(8)
O2 0.0199(7) 0.0315(8) 0.0148(6) 0.0061(5) 0.0041(5) 0.0045(6)
O2W 0.0189(8) 0.0446(10) 0.0287(8) -0.0189(7) 0.0006(7) 0.0016(7)
O3 0.0136(6) 0.0221(7) 0.0172(6) 0.0026(5) 0.0007(5) -0.0007(5)
O3W 0.0657(13) 0.0355(10) 0.0183(8) 0.0100(7) 0.0194(8) 0.0308(9)
O4 0.0205(7) 0.0171(7) 0.0379(8) -0.0109(6) 0.0111(6) -0.0026(5)
O4W 0.0145(7) 0.0236(7) 0.0150(7) 0.0018(5) 0.0055(6) 0.0032(6)
O5 0.0122(6) 0.0233(7) 0.0209(7) -0.0060(5) -0.0009(5) -0.0017(5)
O5W 0.0126(6) 0.0205(7) 0.0140(7) 0.0016(5) 0.0004(5) -0.0045(5)
O6 0.0174(7) 0.0178(6) 0.0218(7) -0.0040(5) 0.0097(5) -0.0011(5)
O6W 0.0142(7) 0.0175(7) 0.0245(7) -0.0083(6) 0.0067(6) -0.0022(5)
O7 0.0171(7) 0.0182(7) 0.0252(7) 0.0052(5) 0.0089(6) 0.0015(5)
O7W 0.0195(7) 0.0197(7) 0.0210(7) 0.0060(6) 0.0116(6) 0.0052(6)
O8 0.0122(6) 0.0225(7) 0.0136(6) 0.0016(5) 0.0012(5) 0.0030(5)

_geom_special_details
;
 All esds (except the esd in the dihedral angle between two l.s. planes)
 are estimated using the full covariance matrix.  The cell esds are taken
 into account individually in the estimation of esds in distances, angles
```

```
 and torsion angles; correlations between esds in cell parameters are only
 used when they are defined by crystal symmetry.  An approximate (isotropic)
 treatment of cell esds is used for estimating esds involving l.s. planes.
;

loop_
 _geom_bond_atom_site_label_1
 _geom_bond_atom_site_label_2
 _geom_bond_distance
 _geom_bond_site_symmetry_2
 _geom_bond_publ_flag
Fe1 O3W 2.0746(16) 2 ?
Fe1 O3W 2.0746(16) . ?
Fe1 O1W 2.1169(17) . ?
Fe1 O1W 2.1169(17) 2 ?
Fe1 O2W 2.1183(15) . ?
Fe1 O2W 2.1183(15) 2 ?
Fe2 O5 1.9414(13) . ?
Fe2 O1 1.9506(13) . ?
Fe2 O7W 2.0051(14) . ?
Fe2 O6W 2.0286(14) . ?
Fe2 O5W 2.0343(13) . ?
Fe2 O4W 2.0362(13) . ?
S1 O4 1.4560(14) . ?
S1 O2 1.4699(13) . ?
S1 O3 1.4748(13) . ?
S1 O1 1.5021(13) . ?
S2 O6 1.4606(13) . ?
```

```
S2 O8 1.4703(13) . ?
S2 O7 1.4716(13) . ?
S2 O5 1.5000(13) . ?

loop_
 _geom_angle_atom_site_label_1
 _geom_angle_atom_site_label_2
 _geom_angle_atom_site_label_3
 _geom_angle
 _geom_angle_site_symmetry_1
 _geom_angle_site_symmetry_3
 _geom_angle_publ_flag
O3W Fe1 O3W 180.00(11) 2 . ?
O3W Fe1 O1W 87.92(8) 2 . ?
O3W Fe1 O1W 92.08(8) . . ?
O3W Fe1 O1W 92.08(8) 2 2 ?
O3W Fe1 O1W 87.92(8) . 2 ?
O1W Fe1 O1W 180.00(9) . 2 ?
O3W Fe1 O2W 91.22(7) 2 . ?
O3W Fe1 O2W 88.78(7) . . ?
O1W Fe1 O2W 93.15(8) . . ?
O1W Fe1 O2W 86.85(8) 2 . ?
O3W Fe1 O2W 88.78(7) 2 2 ?
O3W Fe1 O2W 91.22(7) . 2 ?
O1W Fe1 O2W 86.85(8) . 2 ?
O1W Fe1 O2W 93.15(8) 2 2 ?
O2W Fe1 O2W 180.00(12) . 2 ?
O5 Fe2 O1 89.38(6) . . ?
```

```
O5 Fe2 O7W 95.99(6) . . ?

O1 Fe2 O7W 93.56(6) . . ?

O5 Fe2 O6W 94.93(6) . . ?

O1 Fe2 O6W 175.68(6) . . ?

O7W Fe2 O6W 86.26(6) . . ?

O5 Fe2 O5W 176.22(6) . . ?

O1 Fe2 O5W 91.54(6) . . ?

O7W Fe2 O5W 87.61(6) . . ?

O6W Fe2 O5W 84.14(6) . . ?

O5 Fe2 O4W 90.78(6) . . ?

O1 Fe2 O4W 89.03(6) . . ?

O7W Fe2 O4W 172.77(6) . . ?

O6W Fe2 O4W 90.65(6) . . ?

O5W Fe2 O4W 85.57(6) . . ?

O4 S1 O2 112.35(9) . . ?

O4 S1 O3 110.91(8) . . ?

O2 S1 O3 108.78(8) . . ?

O4 S1 O1 106.21(8) . . ?

O2 S1 O1 108.92(8) . . ?

O3 S1 O1 109.60(8) . . ?

O6 S2 O8 110.88(8) . . ?

O6 S2 O7 111.29(8) . . ?

O8 S2 O7 110.04(8) . . ?

O6 S2 O5 109.18(8) . . ?

O8 S2 O5 106.99(8) . . ?

O7 S2 O5 108.33(8) . . ?

S1 O1 Fe2 141.04(8) . . ?

S2 O5 Fe2 143.08(9) . . ?
```

```
loop_
 _geom_hbond_atom_site_label_D
 _geom_hbond_atom_site_label_H
 _geom_hbond_atom_site_label_A
 _geom_hbond_distance_DH
 _geom_hbond_distance_HA
 _geom_hbond_distance_DA
 _geom_hbond_angle_DHA
 _geom_hbond_site_symmetry_A
O1W H1 O4  0.753(19) 1.99(2) 2.726(2) 164(4) 2_655
O1W H2A O4  0.76(2) 2.42(2) 3.182(3) 172(8) .
O2W H3 O4  0.758(19) 2.08(2) 2.799(2) 159(3) .
O2W H4 O3  0.75(2) 2.28(2) 3.002(2) 159(3) 1_455
O3W H5 O3  0.75(3) 1.98(3) 2.719(2) 173(3) 2_656
O3W H6 O2  0.78(3) 2.07(4) 2.828(2) 165(3) 2_655
O4W H7 O2  0.84(3) 1.82(3) 2.659(2) 174(3) 1_556
O4W H8 O8  0.74(3) 1.90(3) 2.6369(19) 172(3) 1_455
O5W H9 O3  0.72(3) 1.99(3) 2.707(2) 172(3) 1_455
O5W H10 O8  0.84(3) 1.87(3) 2.7091(19) 175(2) 1_454
O6W H11 O6  0.73(3) 2.02(3) 2.740(2) 165(3) 2_667
O6W H12 O7  0.87(3) 1.82(3) 2.6836(19) 174(3) 1_455
O7W H13 O7  0.76(3) 1.92(3) 2.673(2) 173(3) 2_666
O7W H14 O6  0.80(3) 1.96(3) 2.6957(18) 151(3) 1_554
O7W H14 O2  0.80(3) 2.62(3) 3.098(2) 119(2) .

_diffrn_measured_fraction_theta_max    0.995
_diffrn_reflns_theta_full              26.00
```

```
_diffrn_measured_fraction_theta_full   0.995
_refine_diff_density_max    0.313
_refine_diff_density_min   -0.400
_refine_diff_density_rms    0.071
```

Appendix C – Romerite CIF check

checkCIF/PLATON report

You have not supplied any structure factors. As a result the full set of tests cannot be run.

No syntax errors found. CIF dictionary Interpreting this report

Datablock: ron14a

```
Bond precision:  Fe- O = 0.0016 A        Wavelength=0.71073

Cell:            a=6.4274(3)      b=15.2490(7)     c=6.3464(3)
                 alpha=89.7200    beta=100.7900    gamma=85.9600
Temperature:     180 K

                 Calculated                Reported
Volume           609.40(5)                 609.40(5)
Space group      P -1                      P-1
Hall group       -P 1                      ?
Moiety formula   2(Fe H8 O12 S2), Fe H12 O6 ?
Sum formula      Fe3 H28 O30 S4            Fe3 H28 O30 S4
Mr               804.05                    804.01
Dx,g cm-3        2.191                     2.191
Z                1                         1
Mu (mm-1)        2.230                     2.230
F000             410.0                     410.0
F000'            411.82
h,k,lmax         7,18,7                    7,18,7
Nref             2381                      2370
Tmin,Tmax        0.676,0.837               0.606,0.842
Tmin'            0.567

Correction method= MULTI-SCAN

Data completeness= 0.995          Theta(max)= 26.000

R(reflections)= 0.0199( 2274)     wR2(reflections)= 0.0551( 2370)

S = 1.043                 Npar= 229
```

The following ALERTS were generated. Each ALERT has the format
test-name_ALERT_alert-type_alert-level.
Click on the hyperlinks for more details of the test.

Alert level C

```
ABSTY02_ALERT_1_C  An _exptl_absorpt_correction_type has been given without
           a literature citation. This should be contained in the
           _exptl_absorpt_process_details field.
           Absorption correction given as multi-scan
```

Appendix D – Quenstedtite CIF

```
data_quenstedtite

_audit_creation_method            SHELXL-97
_chemical_name_systematic
;
 ?
;
_chemical_name_common             ?
_chemical_melting_point           ?
_chemical_formula_moiety          ?
_chemical_formula_sum
 'H22 Fe2 O23 S3'
_chemical_formula_weight          598.06

loop_
 _atom_type_symbol
 _atom_type_description
 _atom_type_scat_dispersion_real
 _atom_type_scat_dispersion_imag
 _atom_type_scat_source
 'H'  'H'   0.0000   0.0000
 'International Tables Vol C Tables 4.2.6.8 and 6.1.1.4'
 'O'  'O'   0.0106   0.0060
 'International Tables Vol C Tables 4.2.6.8 and 6.1.1.4'
 'S'  'S'   0.1246   0.1234
```

```
 'International Tables Vol C Tables 4.2.6.8 and 6.1.1.4'
 'Fe'  'Fe'   0.3463   0.8444
 'International Tables Vol C Tables 4.2.6.8 and 6.1.1.4'

_symmetry_cell_setting            Triclinic
_symmetry_space_group_name_H-M    P-1

loop_
 _symmetry_equiv_pos_as_xyz
 'x, y, z'
 '-x, -y, -z'

_cell_length_a                    6.1741(1)
_cell_length_b                    23.5062(4)
_cell_length_c                    6.5282(1)
_cell_angle_alpha                 85.633(1)
_cell_angle_beta                  101.553(2)
_cell_angle_gamma                 83.745(2)
_cell_volume                      918.03(3)
_cell_formula_units_Z             2
_cell_measurement_temperature     180(2)
_cell_measurement_reflns_used     1430
_cell_measurement_theta_min       2.63
_cell_measurement_theta_max       25.78

_exptl_crystal_description        block
_exptl_crystal_colour             colourless
_exptl_crystal_size_max           0.08
```

```
_exptl_crystal_size_mid          0.04
_exptl_crystal_size_min          0.02
_exptl_crystal_density_meas      ?
_exptl_crystal_density_diffrn    2.164
_exptl_crystal_density_method    'not measured'
_exptl_crystal_F_000             612
_exptl_absorpt_coefficient_mu    2.034
_exptl_absorpt_correction_type   Multi-scan
_exptl_absorpt_correction_T_min  0.8542
_exptl_absorpt_correction_T_max  0.9604
_exptl_absorpt_process_details   ?

_exptl_special_details
;
 ?
;

_diffrn_ambient_temperature      180(2)
_diffrn_radiation_wavelength     0.71073
_diffrn_radiation_type           MoK\a
_diffrn_radiation_source         'fine-focus sealed tube'
_diffrn_radiation_monochromator  graphite
_diffrn_measurement_device_type  'Bruker APEX-II CCD'
_diffrn_measurement_method       '\f and \w scans'
_diffrn_detector_area_resol_mean ?
_diffrn_standards_number         0
_diffrn_standards_interval_count ?
_diffrn_standards_interval_time  ?
```

```
_diffrn_standards_decay_%        ?
_diffrn_reflns_number            5946
_diffrn_reflns_av_R_equivalents  0.0456
_diffrn_reflns_av_sigmaI/netI    0.0832
_diffrn_reflns_limit_h_min       -4
_diffrn_reflns_limit_h_max       7
_diffrn_reflns_limit_k_min       -27
_diffrn_reflns_limit_k_max       27
_diffrn_reflns_limit_l_min       -7
_diffrn_reflns_limit_l_max       6
_diffrn_reflns_theta_min         1.75
_diffrn_reflns_theta_max         25.00
_reflns_number_total             3147
_reflns_number_gt                2182
_reflns_threshold_expression     >2sigma(I)

_computing_data_collection       'Bruker APEX2'
_computing_cell_refinement       'Bruker SAINT'
_computing_data_reduction        'Bruker SAINT'
_computing_structure_solution    'SHELXS-97 (Sheldrick, 1990)'
_computing_structure_refinement  'SHELXL-97 (Sheldrick, 1997)'
_computing_molecular_graphics    'Bruker SHELXTL'
_computing_publication_material  'Bruker SHELXTL'

_refine_special_details
;
 Refinement of F^2^ against ALL reflections.  The weighted R-factor wR and
 goodness of fit S are based on F^2^, conventional R-factors R are based
```

```
 on F, with F set to zero for negative F^2^. The threshold expression of
 F^2^ > 2sigma(F^2^) is used only for calculating R-factors(gt) etc. and is
 not relevant to the choice of reflections for refinement.  R-factors based
 on F^2^ are statistically about twice as large as those based on F, and R-
 factors based on ALL data will be even larger.
;

_refine_ls_structure_factor_coef  Fsqd
_refine_ls_matrix_type            full
_refine_ls_weighting_scheme       calc
_refine_ls_weighting_details
 'calc w=1/[\s^2^(Fo^2^)+(0.0341P)^2^+0.0000P] where P=(Fo^2^+2Fc^2^)/3'
_atom_sites_solution_primary      direct
_atom_sites_solution_secondary    difmap
_atom_sites_solution_hydrogens    geom
_refine_ls_hydrogen_treatment     mixed
_refine_ls_extinction_method      none
_refine_ls_extinction_coef        ?
_refine_ls_number_reflns          3147
_refine_ls_number_parameters      307
_refine_ls_number_restraints      34
_refine_ls_R_factor_all           0.0653
_refine_ls_R_factor_gt            0.0412
_refine_ls_wR_factor_ref          0.0945
_refine_ls_wR_factor_gt           0.0848
_refine_ls_goodness_of_fit_ref    0.946
_refine_ls_restrained_S_all       0.943
_refine_ls_shift/su_max           0.000
```

```
_refine_ls_shift/su_mean          0.000


loop_
 _atom_site_label
 _atom_site_type_symbol
 _atom_site_fract_x
 _atom_site_fract_y
 _atom_site_fract_z
 _atom_site_U_iso_or_equiv
 _atom_site_adp_type
 _atom_site_occupancy
 _atom_site_symmetry_multiplicity
 _atom_site_calc_flag
 _atom_site_refinement_flags
 _atom_site_disorder_assembly
 _atom_site_disorder_group
Fe1 Fe 0.03200(12) 0.11847(3) 0.25588(12) 0.0156(2) Uani 1 1 d . . .
Fe2 Fe 0.63872(12) 0.38553(3) 0.83515(12) 0.0163(2) Uani 1 1 d . . .
S1 S -0.2375(2) 0.21911(5) 0.4566(2) 0.0166(3) Uani 1 1 d . . .
O1 O -0.1102(6) 0.19358(14) 0.3045(6) 0.0220(9) Uani 1 1 d . . .
O2 O -0.0937(6) 0.21620(14) 0.6655(6) 0.0231(9) Uani 1 1 d . . .
O3 O -0.4248(5) 0.18606(14) 0.4678(6) 0.0211(9) Uani 1 1 d . . .
O4 O -0.3127(6) 0.27891(13) 0.3717(6) 0.0207(9) Uani 1 1 d . . .
S2 S 0.3718(2) 0.07369(5) 0.7096(2) 0.0145(3) Uani 1 1 d . . .
O5 O 0.1974(6) 0.10845(15) 0.5435(6) 0.0259(9) Uani 1 1 d . . .
O6 O 0.2686(6) 0.02770(14) 0.8041(6) 0.0258(9) Uani 1 1 d . . .
O7 O 0.5514(6) 0.05037(14) 0.6153(6) 0.0213(9) Uani 1 1 d . . .
O8 O 0.4474(6) 0.11243(14) 0.8669(6) 0.0217(9) Uani 1 1 d . . .
```

S3 S 0.9446(2) 0.42257(5) 1.2613(2) 0.0164(3) Uani 1 1 d . . .

O9 O 0.7676(5) 0.39716(15) 1.1214(6) 0.0237(9) Uani 1 1 d . . .

O10 O 1.0586(5) 0.37734(14) 1.4258(6) 0.0208(9) Uani 1 1 d . . .

O11 O 1.0979(6) 0.44437(14) 1.1408(6) 0.0228(9) Uani 1 1 d . . .

O12 O 0.8332(6) 0.46969(14) 1.3525(6) 0.0270(9) Uani 1 1 d . . .

O1W O -0.1236(6) 0.12993(15) -0.0499(6) 0.0214(9) Uani 1 1 d D . .

H1WA H -0.119(7) 0.1554(17) -0.138(7) 0.026 Uiso 1 1 d D . .

H1WB H -0.251(4) 0.122(2) -0.069(8) 0.026 Uiso 1 1 d D . .

O2W O 0.1705(7) 0.04291(15) 0.1819(6) 0.0243(9) Uani 1 1 d D . .

H2WA H 0.198(9) 0.038(2) 0.067(4) 0.029 Uiso 1 1 d D . .

H2WB H 0.237(8) 0.0152(16) 0.262(6) 0.029 Uiso 1 1 d D . .

O3W O -0.2159(5) 0.07704(14) 0.3168(6) 0.0181(6) Uani 1 1 d D . .

H3WA H -0.329(6) 0.0829(17) 0.361(8) 0.022 Uiso 1 1 d D . .

H3WB H -0.215(7) 0.0431(11) 0.286(8) 0.022 Uiso 1 1 d D . .

O4W O 0.2688(5) 0.16015(15) 0.1572(6) 0.0181(6) Uani 1 1 d D . .

H4WA H 0.375(6) 0.1701(19) 0.246(6) 0.022 Uiso 1 1 d D . .

H4WB H 0.346(7) 0.1424(18) 0.083(6) 0.022 Uiso 1 1 d D . .

O5W O 0.3394(6) 0.42691(16) 0.8441(7) 0.0239(7) Uani 1 1 d D . .

H5WA H 0.283(7) 0.4572(14) 0.768(7) 0.029 Uiso 1 1 d D . .

H5WB H 0.246(7) 0.4218(19) 0.916(7) 0.029 Uiso 1 1 d D . .

O6W O 0.5083(6) 0.36815(14) 0.5424(6) 0.0189(8) Uani 1 1 d D . .

H6WA H 0.562(7) 0.3404(15) 0.496(8) 0.023 Uiso 1 1 d D . .

H6WB H 0.371(3) 0.3711(19) 0.501(8) 0.023 Uiso 1 1 d D . .

O7W O 0.9242(6) 0.34772(16) 0.7885(6) 0.0239(7) Uani 1 1 d D . .

H7WA H 1.018(6) 0.3249(18) 0.871(5) 0.029 Uiso 1 1 d D . .

H7WB H 1.000(7) 0.357(2) 0.699(6) 0.029 Uiso 1 1 d D . .

O8W O 0.5565(6) 0.31337(15) 0.9534(6) 0.0225(9) Uani 1 1 d D . .

H8WA H 0.463(7) 0.297(2) 0.886(6) 0.027 Uiso 1 1 d D . .

```
H8WB H 0.585(8) 0.299(2) 1.074(4) 0.027 Uiso 1 1 d D . .
O9W O 0.7028(7) 0.46171(16) 0.7105(6) 0.0271(10) Uani 1 1 d D . .
H9WA H 0.749(9) 0.461(2) 0.600(5) 0.032 Uiso 1 1 d D . .
H9WB H 0.758(9) 0.4879(17) 0.769(7) 0.032 Uiso 1 1 d D . .
O10W O 0.3218(7) 0.25140(17) 0.7079(8) 0.0351(11) Uani 1 1 d D . .
H10A H 0.408(7) 0.2290(19) 0.665(10) 0.042 Uiso 1 1 d D . .
H10B H 0.206(5) 0.237(2) 0.701(10) 0.042 Uiso 1 1 d D . .
O11W O 0.1390(7) 0.28712(17) 0.1328(7) 0.0355(11) Uani 1 1 d D . .
H11A H 0.144(10) 0.2507(9) 0.150(8) 0.043 Uiso 1 1 d D . .
H11B H 0.118(10) 0.2959(18) 0.254(4) 0.043 Uiso 1 1 d D . .

loop_
 _atom_site_aniso_label
 _atom_site_aniso_U_11
 _atom_site_aniso_U_22
 _atom_site_aniso_U_33
 _atom_site_aniso_U_23
 _atom_site_aniso_U_13
 _atom_site_aniso_U_12
Fe1 0.0190(4) 0.0155(4) 0.0125(5) -0.0013(3) 0.0035(3) -0.0028(3)
Fe2 0.0162(4) 0.0186(4) 0.0146(5) -0.0019(3) 0.0032(3) -0.0041(3)
S1 0.0227(7) 0.0153(6) 0.0130(8) -0.0018(5) 0.0054(6) -0.0038(5)
O1 0.032(2) 0.0152(18) 0.022(2) -0.0010(16) 0.0150(18) -0.0004(16)
O2 0.034(2) 0.0245(19) 0.012(2) -0.0027(16) 0.0038(18) -0.0098(17)
O3 0.0101(19) 0.030(2) 0.025(2) -0.0037(18) 0.0033(17) -0.0086(16)
O4 0.029(2) 0.0153(18) 0.017(2) 0.0001(16) 0.0076(18) 0.0041(16)
S2 0.0106(6) 0.0177(6) 0.0151(8) -0.0009(5) 0.0027(6) -0.0013(5)
O5 0.031(2) 0.030(2) 0.012(2) -0.0014(17) -0.0013(18) 0.0044(17)
```

O6 0.040(2) 0.0171(18) 0.026(3) -0.0038(17) 0.016(2) -0.0103(17)

O7 0.023(2) 0.0202(19) 0.021(2) -0.0026(17) 0.0072(18) 0.0003(16)

O8 0.030(2) 0.0246(19) 0.014(2) -0.0102(17) 0.0070(18) -0.0087(17)

S3 0.0192(7) 0.0177(7) 0.0128(8) -0.0012(6) 0.0035(6) -0.0044(5)

O9 0.0073(18) 0.040(2) 0.024(2) -0.0053(18) -0.0029(17) -0.0091(16)

O10 0.0085(18) 0.0261(19) 0.024(2) 0.0074(17) 0.0013(17) 0.0026(15)

O11 0.029(2) 0.0229(19) 0.021(2) -0.0020(17) 0.0114(18) -0.0108(17)

O12 0.043(3) 0.0190(19) 0.021(2) -0.0011(17) 0.015(2) -0.0011(18)

O1W 0.030(2) 0.023(2) 0.012(2) 0.0030(16) 0.0028(18) -0.0107(17)

O2W 0.038(2) 0.020(2) 0.016(2) 0.0011(17) 0.012(2) 0.0024(17)

O3W 0.0069(13) 0.0226(14) 0.0266(17) -0.0059(12) 0.0062(12) -0.0024(11)

O4W 0.0069(13) 0.0226(14) 0.0266(17) -0.0059(12) 0.0062(12) -0.0024(11)

O5W 0.0147(14) 0.0314(15) 0.0243(18) 0.0066(13) 0.0084(13) 0.0047(12)

O6W 0.023(2) 0.021(2) 0.014(2) -0.0067(17) 0.0050(18) -0.0011(17)

O7W 0.0147(14) 0.0314(15) 0.0243(18) 0.0066(13) 0.0084(13) 0.0047(12)

O8W 0.025(2) 0.028(2) 0.014(2) 0.0022(18) -0.0017(18) -0.0133(17)

O9W 0.049(3) 0.021(2) 0.017(2) -0.0076(18) 0.013(2) -0.0183(19)

O10W 0.026(2) 0.040(2) 0.050(3) -0.025(2) 0.020(2) -0.014(2)

O11W 0.034(3) 0.034(2) 0.036(3) 0.001(2) 0.006(2) 0.002(2)

_geom_special_details

;

All esds (except the esd in the dihedral angle between two l.s. planes)
are estimated using the full covariance matrix. The cell esds are taken
into account individually in the estimation of esds in distances, angles
and torsion angles; correlations between esds in cell parameters are only
used when they are defined by crystal symmetry. An approximate (isotropic)
treatment of cell esds is used for estimating esds involving l.s. planes.

```
;


loop_
 _geom_bond_atom_site_label_1
 _geom_bond_atom_site_label_2
 _geom_bond_distance
 _geom_bond_site_symmetry_2
 _geom_bond_publ_flag
Fe1 O5 1.933(4) . ?
Fe1 O1 1.961(3) . ?
Fe1 O3W 1.989(3) . ?
Fe1 O1W 2.018(4) . ?
Fe1 O2W 2.021(3) . ?
Fe1 O4W 2.026(3) . ?
Fe2 O9 1.931(4) . ?
Fe2 O8W 1.969(3) . ?
Fe2 O7W 1.976(3) . ?
Fe2 O5W 2.006(3) . ?
Fe2 O6W 2.011(4) . ?
Fe2 O9W 2.022(3) . ?
S1 O4 1.461(3) . ?
S1 O2 1.463(4) . ?
S1 O3 1.472(3) . ?
S1 O1 1.505(4) . ?
S2 O7 1.449(4) . ?
S2 O8 1.465(4) . ?
S2 O6 1.470(3) . ?
S2 O5 1.486(4) . ?
```

```
S3 O11 1.456(4) . ?

S3 O10 1.463(3) . ?

S3 O12 1.467(4) . ?

S3 O9 1.487(4) . ?

O1W H1WA 0.804(19) . ?

O1W H1WB 0.821(19) . ?

O2W H2WA 0.816(19) . ?

O2W H2WB 0.817(19) . ?

O3W H3WA 0.811(19) . ?

O3W H3WB 0.837(19) . ?

O4W H4WA 0.850(19) . ?

O4W H4WB 0.844(19) . ?

O5W H5WA 0.836(19) . ?

O5W H5WB 0.828(19) . ?

O6W H6WA 0.806(19) . ?

O6W H6WB 0.832(19) . ?

O7W H7WA 0.822(19) . ?

O7W H7WB 0.850(19) . ?

O8W H8WA 0.811(19) . ?

O8W H8WB 0.811(19) . ?

O9W H9WA 0.826(19) . ?

O9W H9WB 0.819(19) . ?

O10W H10A 0.812(19) . ?

O10W H10B 0.825(19) . ?

O11W H11A 0.851(19) . ?

O11W H11B 0.863(18) . ?


loop_
```

```
 _geom_angle_atom_site_label_1
 _geom_angle_atom_site_label_2
 _geom_angle_atom_site_label_3
 _geom_angle
 _geom_angle_site_symmetry_1
 _geom_angle_site_symmetry_3
 _geom_angle_publ_flag
O5 Fe1 O1 89.79(16) . . ?
O5 Fe1 O3W 94.59(16) . . ?
O1 Fe1 O3W 93.73(15) . . ?
O5 Fe1 O1W 176.54(16) . . ?
O1 Fe1 O1W 91.11(15) . . ?
O3W Fe1 O1W 88.69(15) . . ?
O5 Fe1 O2W 94.45(16) . . ?
O1 Fe1 O2W 175.59(16) . . ?
O3W Fe1 O2W 87.14(15) . . ?
O1W Fe1 O2W 84.59(16) . . ?
O5 Fe1 O4W 92.08(16) . . ?
O1 Fe1 O4W 87.69(14) . . ?
O3W Fe1 O4W 173.18(16) . . ?
O1W Fe1 O4W 84.61(15) . . ?
O2W Fe1 O4W 90.94(15) . . ?
O9 Fe2 O8W 86.17(16) . . ?
O9 Fe2 O7W 92.67(16) . . ?
O8W Fe2 O7W 93.18(16) . . ?
O9 Fe2 O5W 93.62(16) . . ?
O8W Fe2 O5W 90.55(16) . . ?
O7W Fe2 O5W 172.89(17) . . ?
```

```
O9 Fe2 O6W 176.46(15) . . ?

O8W Fe2 O6W 90.71(16) . . ?

O7W Fe2 O6W 85.83(16) . . ?

O5W Fe2 O6W 88.08(17) . . ?

O9 Fe2 O9W 94.84(16) . . ?

O8W Fe2 O9W 176.41(18) . . ?

O7W Fe2 O9W 90.22(17) . . ?

O5W Fe2 O9W 85.95(16) . . ?

O6W Fe2 O9W 88.38(16) . . ?

O4 S1 O2 110.6(2) . . ?

O4 S1 O3 112.2(2) . . ?

O2 S1 O3 109.5(2) . . ?

O4 S1 O1 105.7(2) . . ?

O2 S1 O1 110.6(2) . . ?

O3 S1 O1 108.2(2) . . ?

S1 O1 Fe1 139.0(2) . . ?

O7 S2 O8 111.8(2) . . ?

O7 S2 O6 111.4(2) . . ?

O8 S2 O6 109.9(2) . . ?

O7 S2 O5 108.9(2) . . ?

O8 S2 O5 106.7(2) . . ?

O6 S2 O5 107.9(2) . . ?

S2 O5 Fe1 148.4(2) . . ?

O11 S3 O10 111.5(2) . . ?

O11 S3 O12 110.3(2) . . ?

O10 S3 O12 110.5(2) . . ?

O11 S3 O9 110.1(2) . . ?

O10 S3 O9 107.3(2) . . ?
```

```
O12 S3 O9 107.1(2) . . ?

S3 O9 Fe2 145.7(2) . . ?

Fe1 O1W H1WA 129(4) . . ?

Fe1 O1W H1WB 113(4) . . ?

H1WA O1W H1WB 108(3) . . ?

Fe1 O2W H2WA 124(3) . . ?

Fe1 O2W H2WB 128(3) . . ?

H2WA O2W H2WB 106(3) . . ?

Fe1 O3W H3WA 140(3) . . ?

Fe1 O3W H3WB 117(3) . . ?

H3WA O3W H3WB 104(3) . . ?

Fe1 O4W H4WA 120(3) . . ?

Fe1 O4W H4WB 117(3) . . ?

H4WA O4W H4WB 99(3) . . ?

Fe2 O5W H5WA 123(3) . . ?

Fe2 O5W H5WB 134(3) . . ?

H5WA O5W H5WB 103(3) . . ?

Fe2 O6W H6WA 120(4) . . ?

Fe2 O6W H6WB 120(4) . . ?

H6WA O6W H6WB 108(3) . . ?

Fe2 O7W H7WA 128(3) . . ?

Fe2 O7W H7WB 130(3) . . ?

H7WA O7W H7WB 101(3) . . ?

Fe2 O8W H8WA 121(3) . . ?

Fe2 O8W H8WB 129(3) . . ?

H8WA O8W H8WB 109(3) . . ?

Fe2 O9W H9WA 116(4) . . ?

Fe2 O9W H9WB 130(4) . . ?
```

```
H9WA O9W H9WB 105(3) . . ?

H10A O10W H10B 106(3) . . ?

H11A O11W H11B 100(3) . . ?


loop_

 _geom_hbond_atom_site_label_D

 _geom_hbond_atom_site_label_H

 _geom_hbond_atom_site_label_A

 _geom_hbond_distance_DH

 _geom_hbond_distance_HA

 _geom_hbond_distance_DA

 _geom_hbond_angle_DHA

 _geom_hbond_site_symmetry_A

O1W H1WA O2  0.804(19) 1.888(19) 2.692(5) 177(5) 1_554

O1W H1WB O8  0.821(19) 1.86(2) 2.679(5) 172(5) 1_454

O2W H2WA O6  0.816(19) 1.88(2) 2.695(5) 178(6) 1_554

O2W H2WB O7  0.817(19) 1.92(3) 2.709(5) 162(5) 2_656

O3W H3WA O7  0.811(19) 2.07(4) 2.718(5) 136(5) 1_455

O3W H3WB O6  0.837(19) 1.85(2) 2.675(5) 169(5) 2_556

O4W H4WA O3  0.850(19) 1.80(2) 2.639(5) 170(5) 1_655

O4W H4WB O8  0.844(19) 1.81(2) 2.638(5) 164(5) 1_554

O5W H5WA O12  0.836(19) 1.84(2) 2.665(5) 169(5) 2_667

O5W H5WB O11  0.828(19) 1.95(3) 2.700(5) 150(5) 1_455

O6W H6WA O4  0.806(19) 1.88(2) 2.685(5) 176(6) 1_655

O6W H6WB O10  0.832(19) 1.88(2) 2.708(5) 177(6) 1_454

O7W H7WA O11W  0.822(19) 1.84(2) 2.598(6) 153(4) 1_656

O7W H7WB O10  0.850(19) 1.92(2) 2.728(5) 158(5) 1_554

O8W H8WA O10W  0.811(19) 1.80(2) 2.584(5) 164(6) .
```

```
O8W H8WB O4  0.811(19) 1.92(2) 2.721(5) 168(5) 1_656
O9W H9WA O12  0.826(19) 1.80(2) 2.620(5) 173(6) 1_554
O9W H9WB O11  0.819(19) 1.98(2) 2.787(5) 169(5) 2_767
O10W H10A O3  0.812(19) 2.06(3) 2.844(5) 162(6) 1_655
O10W H10B O2  0.825(19) 1.93(2) 2.749(5) 169(5) .
O11W H11A O4W  0.851(19) 2.18(3) 2.989(5) 159(5) .
O11W H11A O1  0.851(19) 2.48(5) 3.084(5) 128(4) .
O11W H11B O10  0.863(18) 2.32(3) 3.028(6) 139(4) 1_454

_diffrn_measured_fraction_theta_max    0.972
_diffrn_reflns_theta_full              25.00
_diffrn_measured_fraction_theta_full   0.972
_refine_diff_density_max    0.788
_refine_diff_density_min   -0.658
_refine_diff_density_rms    0.111
```

Appendix E – Quenstedtite CIF check

checkCIF/PLATON report

You have not supplied any structure factors. As a result the full set of tests cannot be run.

No syntax errors found. CIF dictionary Interpreting this report

Datablock: ron15c

```
Bond precision:  S- O = 0.0040 A          Wavelength=0.71073

Cell:          a=6.1741(1)       b=23.5062(4)      c=6.5282(1)
               alpha=85.633(1)   beta=101.553(2)   gamma=83.745(2)
Temperature:   180 K
```

	Calculated	Reported
Volume	918.03(3)	918.03(3)
Space group	P -1	P-1
Hall group	-P 1	?
Moiety formula	Fe H8 O12 S2, Fe H10 O9 S, 2(H2 O)	?
Sum formula	Fe2 H22 O23 S3	H22 Fe2 O23 S3
Mr	598.09	598.06
Dx,g cm-3	2.164	2.164
Z	2	2
Mu (mm-1)	2.034	2.034
F000	612.0	612.0
F000'	614.57	
h,k,lmax	7,27,7	7,27,7
Nref	3239	3147
Tmin,Tmax	0.907,0.960	0.854,0.960
Tmin'	0.850	

```
Correction method= MULTI-SCAN

Data completeness= 0.972          Theta(max)= 25.000

R(reflections)= 0.0412( 2182)     wR2(reflections)= 0.0945( 3147)

S = 0.946                 Npar= 307
```

The following ALERTS were generated. Each ALERT has the format
test-name_ALERT_alert-type_alert-level.
Click on the hyperlinks for more details of the test.

Alert level B

CHEMS01_ALERT_1_B The sum formula contains elements in the wrong order.
H precedes Fe
Sequence must be alphabetical for inorganic structures.